

Editorial corner – a personal view

Waste tyre rubber – what to do next?

*J. Karger-Kocsis**

MTA–BME Research Group for Composite Science and Technology and Department of Polymer Engineering, Faculty of Mechanical Engineering, Budapest University of Technology and Economics Műegyetem rkp. 3., H-1111, Budapest, Hungary

The recycling of worn tyres poses a great challenge nowadays. Land filling is no more a viable option in many countries. Energy recovery routes cover the use of tyres as non-fossil fuel and also some energy recovery/material recycling options. Material recycling routes focus on the combinations of particulate (crumb, ground) rubber with polymeric materials. This ensures the flowability under certain conditions and guarantees products' shaping at acceptable cost. Note that the production of crumb rubber from worn tyres is a well established industrial practice.

Civil engineering is using large quantity of crumb rubbers using bitumen, concrete and especially moisture curable polyurethane systems as 'binders'. Major advantage of this 'particle bonding' strategy is that a high amount of waste rubber can be recycled by this way. On the other hand, mostly 'noncritical' rubber items can be manufactured.

Therefore, there is a great demand to find new, value-added use for crumb rubber fractions. Unfortunately, the incorporation of crumb rubber in thermoplastics and fresh, crosslinkable rubbers is strongly limited (less than 10 wt.%) being associated with prominent property degradation. It was concluded recently that value-added application of ground tyre rubber (GTR) can especially be expected via production of thermoplastic rubbers (DOI: [10.1007/s10853-012-6564-2](https://doi.org/10.1007/s10853-012-6564-2)). Here the key issue is to improve the interfacial adhesion between the GTR particles and matrix polymer. This can be achieved by surface modifications and/or devulcanization/reclamation procedures of GTR, by adding suitable compatibilizers to the polymers and performing reactive extrusion. Thermoplastic rubbers can be prepared even in line through continuous

extrusion including the chemical destruction of GTR and its combination with suitable polymers with and without dynamic curing. The production of cellular thermoplastics with GTR content is also a straight-forward strategy (if there is no adhesion between the matrix and GTR then why not avoid this problem by foaming?). Unlike to thermosetting resins, the incorporation of GTR in fresh rubber stocks remains a promising recycling route provided that GTR devulcanization/reclaiming is economically solved. According to the authors' feeling thermo-mechanical and thermo-mechano-chemical decomposition routes should be preferred for that.

One can also recognize a new trend in GTR recycling: other properties instead of the mechanical ones, such as acoustic and vibration damping, become under spot of interest. This is reasoned by the fact that rubbers and with locally inhomogeneous crosslinked structure, like GTR itself, are excellent vibration and sound absorbers.

Albeit a large body of works has been addressed the material recycling of GTR, further efforts are badly needed – so, why not to make a valuable contribution to this issue?



Prof. Dr. Dr. h.c. József Karger-Kocsis
Editor-in-Chief

*Corresponding author, e-mail: karger@pt.bme.hu
© BME-PT

Toward reliable morphology assessment of thermosets via physical etching: Vinyl ester resin as an example

S. Grishchuk¹, A. Bonyár², J. Elsässer³, A. Wolynski⁴, J. Karger-Kocsis^{5,6*}, B. Wetzel¹

¹Institut für Verbundwerkstoffe GmbH (Institute for Composite Materials), University of Kaiserslautern, Erwin-Schrödinger Str. 58, D-67663 Kaiserslautern, Germany

²Department of Electronics Technology, Budapest University of Technology and Economics, H-1111 Budapest, Hungary

³Arbeitsgruppe Werkstoff- und Oberflächentechnik Kaiserslautern (Workgroup Materials and Surface Technologies), University of Kaiserslautern, Erwin-Schrödinger Str. 58, D-67663 Kaiserslautern, Germany

⁴Photonik-Zentrum Kaiserslautern e.V., Kohlenhofstr. 10, D-67663 Kaiserslautern, Germany

⁵MTA–BME Research Group for Composite Science and Technology, Műegyetem rkp. 3, H-1111 Budapest, Hungary

⁶Department of Polymer Engineering, Faculty of Mechanical Engineering, Budapest University of Technology and Economics, H-1111 Budapest, Hungary

Received 30 November 2012; accepted in revised form 13 January 2013

Abstract. The morphology of peroxide-cured, styrene crosslinked, bisphenol A-based vinyl ester (VE) resin was investigated by atomic force microscopy (AFM) after ‘physical’ etching with different methods. Etching was achieved by laser ablation, atmospheric plasma treatment and argon ion bombardment. Parameters of the etching were varied to get AFM scans of high topography resolution. VE exhibited a nanoscaled nodular structure the formation of which was ascribed to complex intra- and intermolecular reactions during crosslinking. The microstructure resolved after all the above physical etching techniques was similar provided that optimized etching and suitable AFM scanning conditions were selected. Nevertheless, with respect to the ‘morphology visualization’ these methods follow the power ranking: argon bombardment > plasma treatment > laser ablation.

Keywords: thermosetting resins, physical etching, morphology, nodular structure, structural inhomogeneity

1. Introduction

There is a long lasting dispute on whether the structure of thermosets becomes homogenous or heterogeneous after their curing. Usual arguments for homogeneity list the appearance of a sharp, well detectable glass transition relaxation, no direct evidence of heterogeneity by electron microscopy techniques, perfect agreement with conversion calculations accepting a single curing mechanism. For amine-cured epoxy (EP) systems for example it has been quoted that their structure is homogenous and results against this claim are linked with artifacts,

especially when resolved in nanoscale ([1] and references therein).

Atomic force microscopy (AFM) seems to be one of the best tools to study the morphology of cured thermosets. Using its phase contrasting tapping mode one can resolve the eventually present two-phase structure provided that the corresponding phases have a large enough difference in their stiffness and related characteristics (e.g. hardness). Supposing ab ovo that the network structure of thermosets is inhomogeneous, the degradation of its constituents should be different, as well. This fea-

*Corresponding author, e-mail: karger@pt.bme.hu

© BME-PT

ture can be exploited for the ‘visualization’ of the morphology via controlled degradation of the phase constituents. For that purpose various physical etching techniques may be used. However, to explore their applicability, it is straightforward to use suitable model materials, such as vinyl ester (VE) and resin blends [2]. Commercial VEs may contain up to 50 wt% styrene comonomer and their curing is induced by peroxides in presence or absence of accelerators. Considering the fact that VE is tetrafunctional (bearing two double bonds), whereas styrene is bifunctional, the ‘real’ crosslinking agent is the VE itself in VE/styrene formulations. During curing of VEs different coreactions may occur. Beside of the favored VE/styrene copolymerization, VE/VE and styrene/styrene homopolymerizations may take place. There is a difference in the reactivity ratios of the above listed possible reactions. In addition, the growing, branching chains may be involved in intra- and intermolecular reactions. Last but not least the gelling phase, occurring during crosslinking, strongly affects the course of the various reactions through hampering the molecular diffusion. The above scenario already suggests that VE and similar systems should possess a heterogeneous structure. This has been proved on unetched samples by AFM [1, 3–4] and even by scanning electron microscopy [5]. By the latter method micronscaled, whereas with the AFM nanoscaled domains, called nodules, were detected. The corresponding structure is frequently termed as microgel. The AFM scans were sometimes of low quality and thus less suited for an insight in the morphology [3]. Detectability of the morphology was prominently improved by physical etching. VE samples were etched by laser treatment [6] and argon ion (Ar^+) bombardment [7]. On the other hand, the nodules’ size in the published works often differed from one another markedly. This may be due to differences in the type and composition in the VE resins (e.g. styrene amount, accelerator content) and due to artifacts generated by the physical etching techniques themselves. Nonetheless, it is commonly accepted that the nodules formed by intramolecular reactions and they are VE-rich by contrast to the embedding matrix phase that is polystyrene-rich [4, 7].

The aim of this study was to get a deeper understanding in the morphology of VE by using various

physical etching techniques whereby varying their conditions, and to check whether optimized etching parameters reveal the same morphology without artifacts. For VE etching laser ablation, atmospheric plasma treatment and Ar^+ bombardment were used. Note that in depth studies on the VE morphology are essential to reveal changes caused by recent modification strategies, such as resin hybridization [8] and nanofilling [9], as well.

2. Experimental

2.1. Materials, sample preparation

A styrene diluted bisphenol-A type vinyl ester (VE) Daron-XP-45-A2 from DSM Composite Resins AG (Schaffhausen, Switzerland) with a density of 1.080 g/ml, viscosity of 175–225 mPa·s and styrene content of ca. 30 wt% was chosen for this study. Dibenzoyl peroxide (BPO; Perkadox CH50L: peroxide content 50 wt%) and N,N-diethyl aniline (DEA; Accelerator NL-64-100) were purchased from Akzo Nobel (Düren, Germany) and used as initiator and accelerator for the free radical polymerization, respectively. The preparation procedure was as follows. First, 1.5 part per hundred resin [phr] of BPO was dissolved in the VE resin at ambient temperature at 800 revolutions per minute [rpm] mixing speed and the obtained mixture was degassed *in vacuo*. Then, 0.15 phr of DEA accelerator was introduced. The mixture was mixed for additional 3 min at 800 rpm, degassed and introduced in open polytetrafluoro ethylene moulds. Plates $100 \times 8 \times 4 \text{ mm}^3$ (length \times width \times thickness) were produced using the following curing regime: room temperature for 45 min, 50°C for 15 min, 80°C for 30 min, 140°C for 30 min, and finally 180°C for 1 hour. The moulds were then cooled to ambient temperature overnight and the specimens removed, cut to the size $8 \times 8 \times 4 \text{ mm}^3$ (length \times width \times thickness), fixed in cylindrical steel clips for mounting (Buehler GmbH, Düsseldorf, Germany), embedded in EpoFix bisphenol-A based ($M_n \leq 700 \text{ g/mol}$) triethylene tetramine curable mounting epoxy resin from Struers (Ballerup, Denmark). The embedding resin was cured overnight at ambient temperature in the pressure chamber Technomat from Heraeus Kulzer GmbH (Wehrheim/Ts., Germany) at 2 bar air pressure in order to remove the on the sample surface adsorbed air bubbles and ensure the good quality of embedding. Afterwards, embedded samples were polished at 300 rpm using

Buehler Alpha 2 speed grinder-polisher from Buehler GmbH (Düsseldorf, Germany) with silicon carbide grinding paper Buehler-Met[®] II of different grits (from 800 to 4000) under continuous water flow cooling. Further polishing was performed using TegraPol-21 polishing machine with Tegra Force-5 head from Struers using diamond suspensions of 3 μm and finally of 1 μm corn size from Buehler (Lake Bluff, IL, USA). After final polishing procedure the samples were washed thoroughly with water and then in isopropanol in a Bandelin Sonorex Super RK 103 H ultrasound bath (Badelin Electronic, Berlin, Germany) working at 100% power (320 W) at a frequency of 35 kHz for 2×15 min. The polished sides of the embedded specimens were cut to 1 mm thick plates using precise in-hole micro-saw Leica 1600 from Leica Instruments GmbH (Nussloch, Germany) with diamond coated cutting unit Winter D46 JS 35D (Saint-Gobain Diamantwerkzeuge, Norderstedt, Germany), resulting in the $8 \times 8 \times 1 \text{ mm}^3$ (length \times width \times thickness) embedded samples. The polished surfaces were rinsed with isopropanol once again prior to the physical etching.

2.2. Physical etching

For physical etching the following techniques were used: laser ablation (LA), plasma treatment (PT) and Ar^+ bombardment (AB).

The ultrafast laser system used for LA in this paper was a commercially available picoseconds [ps] laser system with 10 ps pulse duration (HYPER25, Lumera Laser, Kaiserslautern, Germany). The experiments were run at a laser wavelength in the UV spectral range ($\lambda = 355 \text{ nm}$) and at high pulse repetition frequencies (PRF = 200 kHz). For fast beam deflection a galvanometer scanner (hurrySCAN, Scanlab, Munich, Germany) was used at feed rates as high as 1400 mm/s. Using an $f = 100 \text{ mm}$ objective mounted at the scanner system's beam exit the laser beam was focused on the sample surface to a spot size of about 12 μm . The pulse energy was varied between 1 and 15 μJ during the laser treatment of 5 mm long and 1 mm wide areas. In order to achieve the necessary topology an optimized pulse to pulse overlap was chosen, while the laser etching process was repeated up to three times per area. Accordingly, a sample designated as e.g. $3 \times 7 \mu\text{J}$ means that the pulse energy was set to 7 μJ and the laser etch-

ing process was repeated three times on the whole surface of the corresponding area.

Information on the topology was received by a chromatically encoded confocal measurement (CHRocodile E, Precitec Optronic GmbH, Ridgau, Germany) with an axial resolution of 35 nm, (measuring rate 4 kHz, lateral measuring distance $\Delta x = \Delta y = 2.5 \mu\text{m}$, feed rate 1 mm/min) yielding an arithmetic surface roughness (R_a) in the range of 260–480 nm. It is noteworthy that in the pioneering work of Mortaigne [6] on the laser ablation of VE using a pulsed ArF excimer laser ($\lambda = 193 \text{ nm}$, PRF 10 Hz, number of pulses 200, pulse duration = 16 ns) an ablation threshold of about 25 mJ/cm^2 laser fluence was determined. In our case LA etching process using 10 ps laser pulses was observed at pulse energies as small as 1 μJ , which corresponds to a laser fluence of about 1.7 J/cm^2 . Note that the ablation threshold of 10 ps pulses was not determined in this work. The laser fluence (energy density, ED) was calculated from the pulse energy (E_p) and spot size (radius of the beam, R ; here 6 μm) as follows taking into account the Gaussian character of the beam (factor 2 in Equation (1)):

$$ED = \frac{E_p}{\pi R^2} \quad (1)$$

ED is in the range of ca. 5.3 J/cm^2 and ca. 37.2 J/cm^2 based on the minimum ($3 \times 1 \mu\text{J} = 3 \mu\text{J}$) and maximum ($3 \times 7 \mu\text{J} = 21 \mu\text{J}$) conditions of the LA etching, respectively.

The basic event by using ultrashort laser pulses is the ablation of thin material layers in the order of tens of nanometers. This offers a reliable and high resolution etching process. In comparison to excimer lasers the PRF is several orders of magnitude higher, which will be advantageous for laser treatment of large areas.

Atmospheric low-frequency PT was performed in a Plasmatreater 400 (Plasmatrete GmbH, Steinhagen, Germany) in air. The related plasma jet system consists of one PTW10 nozzle mounted in parallel manner. This allows the treatment in 2 mm width. The following parameters such as plasma voltage (280 V), plasma current (3.4 A), plasma power (21 kHz), plasma cycle time (100%), initial pressure (1000 mbar) were kept constant. Variables of the PT were the distance of the substrate to the jet orifice (5–20 mm) and the nozzle feed velocity (5–

20 m/min). Each sample has got one single treatment. Unfortunately, here the authors were not able to estimate the surface-related PT energy.

In case of argon ion bombardment (AB) the polished surface of the specimens was eroded by Ar^+ ions using a secondary neutral mass spectrometer (INA-X, SPECS GmbH, Berlin, Germany) operating at 500 eV and at a plasma potential of ca. 40–50 eV using diaphragm of 10 mm in diameter. The incoming beam was oriented perpendicularly to the surface of the specimen. The distance 4.7 mm from the beam source to the surface of the specimen was set. The irradiation time, was the only parameter that was varied in three steps: 5, 10 and 20 min. This resulted in overall ion doses of approximately $0.9 \cdot 10^{18}$, $1.9 \cdot 10^{18}$ and $3.8 \cdot 10^{18}$ Ar^+/cm^2 , respectively. The corresponding surface related energy values are: $4.5 \cdot 10^{20}$, $9.5 \cdot 10^{20}$ and $1.9 \cdot 10^{21}$ $\text{eV} \cdot \text{Ar}^+/\text{cm}^2$, respectively, calculated by multiplying the overall ion doses with their energy of 500 eV ($= 8.01 \cdot 10^{-17}$ J). The above data in the range of 72.1–304.4 J/cm^2 are estimated values. Note that AB etching with the middle flux value was already practiced for VE [7] and VE/EP hybrids [2].

2.3. AFM testing

For the AFM scans two devices were used, viz. MultiMode AFM-2 type NanoScope[®]IIIa from Veeco-Digital Instruments (Mannheim, Germany) and diInnova type instrument of Bruker AXS (Karlsruhe, Germany). They are denoted next as AFM-a and AFM-b, respectively.

Scans with AFM-a were registered in tapping mode, and the related height-, amplitude- and phase-contrast images captured. An Al-coated (reflection side) N-type silicon (Si) cantilever (125 μm cantilever length, 4.5 μm thickness, 35 μm width), product of AppNano (Santa Clara, Ca, USA), with a nominal tip radius of less than 10 nm, tip height of 14–16 μm and spring constant in the range of 25–75 Nm^{-1} (about 50 Nm^{-1}) was employed in the range of its fundamental resonance frequency of 200–400 kHz (about 330 kHz). The scan rates were set at 0.5 Hz for all images.

The experimental conditions of AFM-b were as follow: tapping mode images were made with a Bruker RTESPA-CP type antimony (n) doped Si tip with a nominal tip radius below 10 nm (125 μm cantilever

length, 4 μm thickness, 35 μm width, 40 Nm^{-1} spring constant and 300 kHz resonance frequency). Amplitude, height and phase-contrast images were captured with a scan rate of 1 Hz and 512×512 sampling rate. During the scans the PID values of the scanner feedback were optimized according to the User Manual to gain the best image quality. For data evaluation the Gwyddion 2.27 software was used.

3. Results and discussion

3.1. Laser treatment (LA)

As expected based on the work of Mortaigne [6] there should be a lower ablation threshold that should be surpassed during etching. Figure 1 shows a series of AFM height, amplitude and phase contrast images taken from the VE etched by different LA parameters. One can notice that three times 5 to 7 μJ treatments gave an optimum topography. By contrast, etching two times by 10 μJ (that is comparable from the point of view of the overall dose) results already in a smeared surface due to obvious melting phenomena. This means that also an upper threshold exists for LA above which the bulk properties may prominently alter. Moreover, the latter threshold cannot be assigned to an overall dose because the dose in one step is of great relevance, too.

Albeit the microgel structure is well recognizable in most of the AFM-a scan in Figure 1, there is a large difference in their size compared to former results [4, 7] reporting on nanoscaled nodules. Based on Figure 2 the nodule size may reach 0.5 μm . However, the height scan from the same sample provided by AFM-b with a fresh cantilever revealed that the nodules are in nanoscale, in fact (cf. Figure 3). It is noteworthy that the ‘used’ cantilever in AFM-b yielded a similar morphology as AFM-a, as shown in Figure 2. Accordingly, the conditions of AFM testing should be properly set, and even the tip of the cantilever purposefully checked, in order to achieve the necessary resolution.

3.2. Plasma treatment (PT)

First the combined effects of the distance to nozzle/nozzle speed were checked in the range 5/5, 7/7, 10/10, 15/15 and 20/20 [$\text{mm}/(\text{m}/\text{min})$] settings. Change in the surface relief was observed only at 10

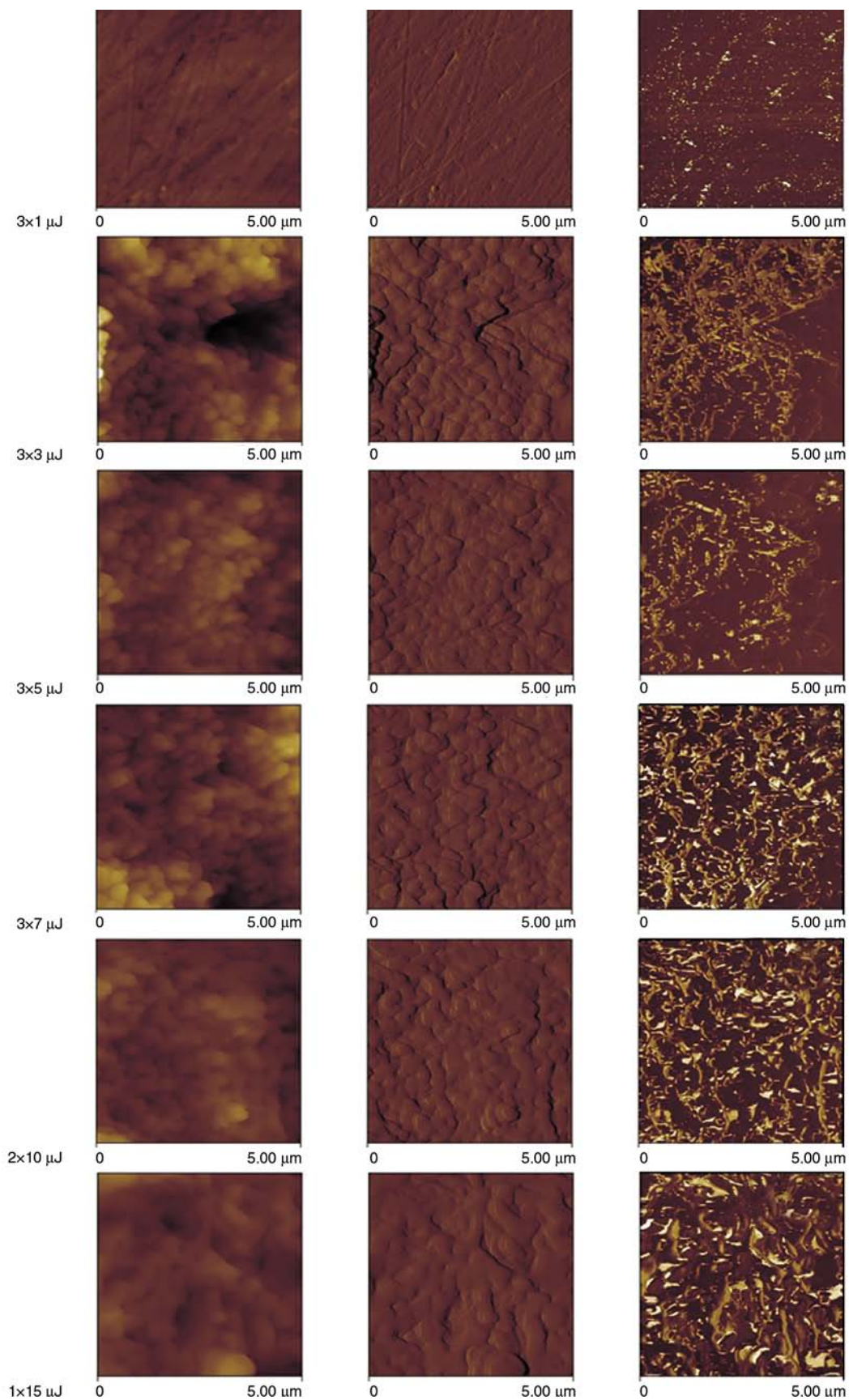


Figure 1. Height (left), amplitude (middle) and phase contrast (right) AFM-a scans taken from VE after different LA conditions

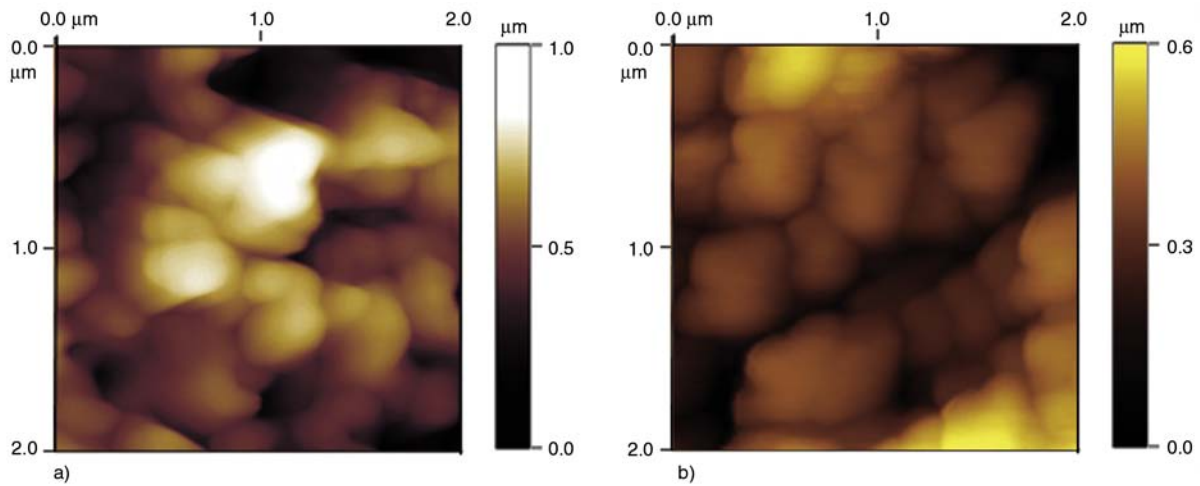


Figure 2. AFM-a (a) and AFM-b (b) height scans from VE etched by $3 \times 7 \mu\text{J}$

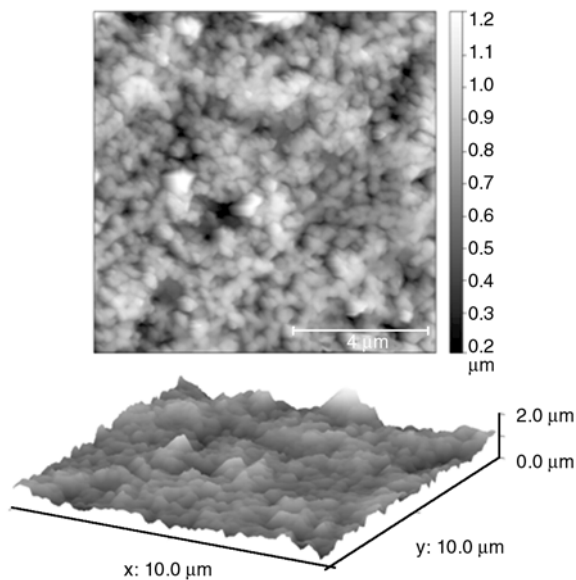


Figure 3. Two- and three-dimensional AFM-b scans from VE etched by $3 \times 7 \mu\text{J}$ showing the existence of nanoscaled nodules

to 15 mm distances to nozzle and 10 to 15 m/min speeds. Outside this range less surface roughening appeared according to the AFM-a scans in Figure 4. AFM scans registered on the VE after optimum PT conditions are given in Figure 5. The phase contrast picture in Figure 5 suggests, however, that even under these PT conditions surface melting took place and thus further ‘tuning’ of this etching technique is required.

The most important finding is, however, that the nodules’ size range (30–70 nm) agrees reasonably with that of derived from Figure 3.

3.3. Argon ion bombardment (AB)

Figure 6 compares the AFM scans taken after AB with various Ar^+ ion fluxes. One can see that only highest flux yielded the expected surface morphology. This means that the use of AB also requires the determination of a threshold and most likely also a proper ‘working’ range for this kind of etching, as well.

Results in Figure 6d confirm that the size of the nodules is nanoscaled. They are in the range of 30–100 nm. This value is well matched with those derived after LA and PT performed in optimum etching conditions. Further, this nodules’ range agrees fairly with that one found in our earlier work [7].

This means that all above etching methods may be used to visualize the morphology of thermosets after detecting the best etching conditions. As far as the methods concern, one can state that AB is more straightforward than PT or LA. This is the right place to underline that further considerable efforts are needed to find the right ways to reveal the morphology of thermosets. The physically etched surfaces should be subjected to analytical investigations covering Fourier transform infrared (FTIR), Raman and X-ray photoelectron spectroscopy analyses to clarify eventual chemical changes. Further, the etching in different atmospheres, combined with in depth analytics on the degradation pathways are further challenging and necessary tasks in this respect.

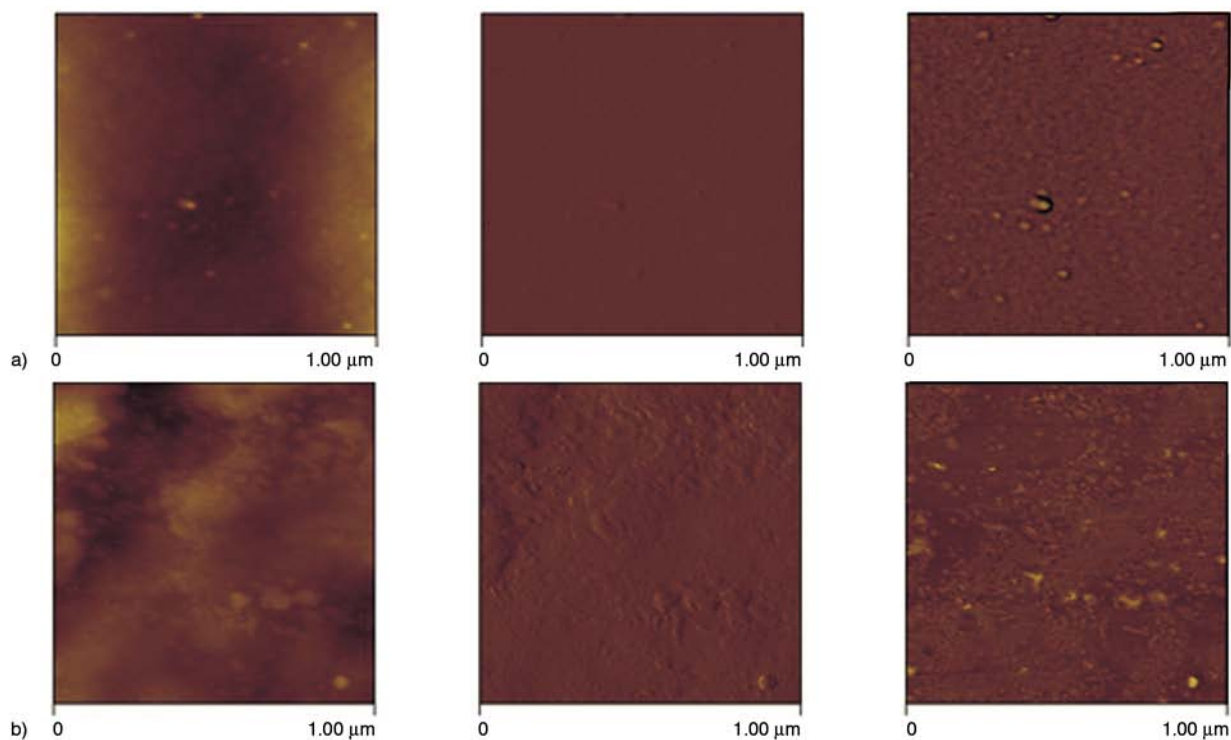


Figure 4. Height (left), amplitude (middle) and phase contrast images (right) taken by AFM-a after PT performed at distance/speed ratios of 7 mm/7 m/min (a), and 20 mm/20 m/min (b), respectively

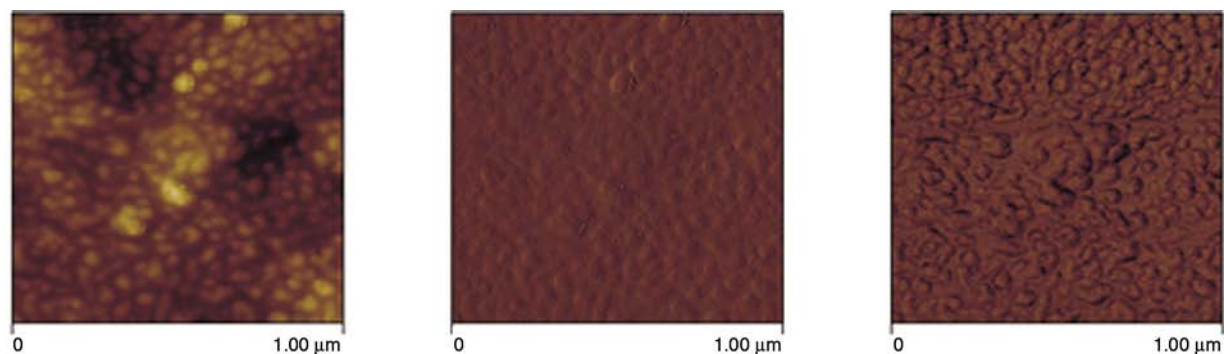


Figure 5. Height (left), amplitude (middle) and phase contrast images (right) taken by AFM-a after optimum PT conditions, viz. distance between substrate and nozzle 15 mm and nozzle speed 15 m/min

4. Conclusions

This work was devoted to the morphology detection of a cured vinyl ester (VE) resin by atomic force microscopy (AFM) after various ‘physical’ etching techniques, namely laser ablation (LA), atmospheric plasma treatment (PT) and argon ion bombardment (AB). It was established that all above techniques may be used when their conditions are adjusted to the related thermoset. In order to avoid etching technique-related artifacts, attention should be taken to define the ‘working window’, i.e. the range between lowest and highest etching/ablation thresholds, which reflect the initial structure adequately.

Acknowledgements

The research leading to the reported results has received funding from a German (DAAD) -Hungarian (MÖB) collaboration project and from the Hungarian Scientific Research Fund (OTKA-NK 83421). It was also connected to the scientific program of the ‘Development of quality-oriented and harmonized R+D+I strategy and functional model at BME’, supported by the New Hungary Development Plan (Project ID: TÁMOP-4.2.1/B-09/1/KMR-2010-0002). The authors are thankful to the following colleagues due their help in this work: M. Fejös (Budapest), Prof. P. Geiß, Prof. J. L’huillier, Dr. Th. Herrmann, Dr. W. Bock, Dr. M. Wahl, Mr. S. Passlack, Mr. S. Schmitt, Mr. J. Mersch (Kaiserslautern).

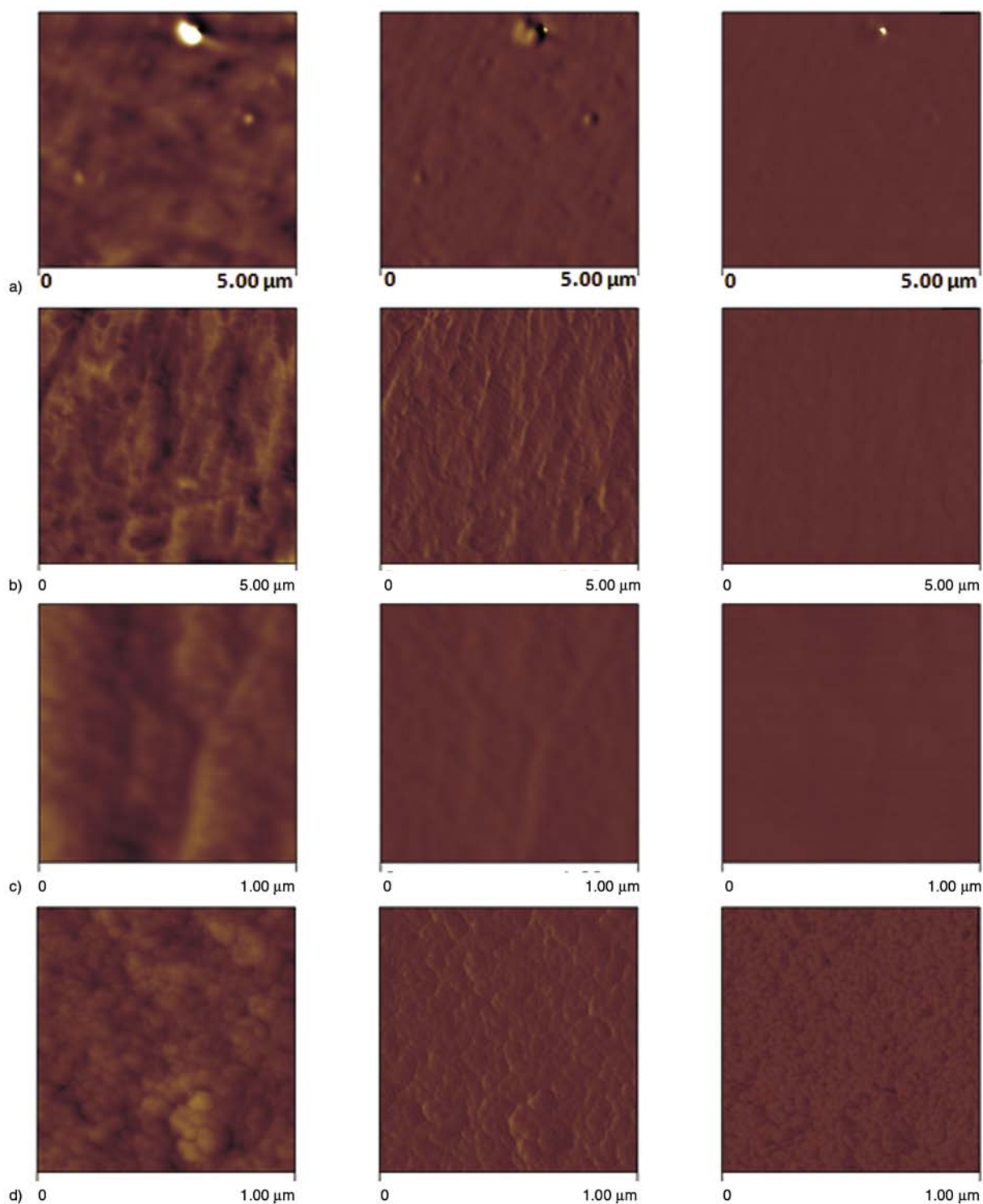


Figure 6. Height (left), amplitude (middle) and phase contrast images (right) taken by AFM-a after bombarding with various Ar^+ fluxes. Designations: fluxes = $0.95 \cdot 10^{18} \text{ Ar}^+/\text{cm}^2$ (a), $1.9 \cdot 10^{18} \text{ Ar}^+/\text{cm}^2$ (b, c) and $3.8 \cdot 10^{18} \text{ Ar}^+/\text{cm}^2$ (d)

References

- [1] Duchet J., Pascault J. P.: Do epoxy–amine networks become inhomogeneous at the nanometric scale? *Journal of Polymer Science Part B: Polymer Physics*, **41**, 2422–2432 (2003).
DOI: [10.1002/polb.10585](https://doi.org/10.1002/polb.10585)
- [2] Gryshchuk O., Karger-Kocsis J.: Influence of the type of epoxy hardener on the structure and properties of interpenetrated vinyl ester/epoxy resins. *Journal of Polymer Science Part A: Polymer Chemistry*, **42**, 5471–5481 (2004).
DOI: [10.1002/pola.20371](https://doi.org/10.1002/pola.20371)

- [3] Mosiewicki M. A., Schroeder W. F., Leite F. L., Hermann P. S. P., Curvelo A. A. S., Aranguren M. I., Borrajo J.: AFM fracture surface study of vinylester and unsaturated polyester based thermosets. *Journal of Materials Science*, **41**, 6154–6158 (2006).
DOI: [10.1007/s10853-006-0163-z](https://doi.org/10.1007/s10853-006-0163-z)
- [4] Rodriguez E., Larrañaga M., Mondragón I., Vázquez A.: Relationship between the network morphology and properties of commercial vinyl ester resins. *Journal of Applied Polymer Science*, **100**, 3895–3903 (2006).
DOI: [10.1002/app.22732](https://doi.org/10.1002/app.22732)
- [5] Li P., Yang X., Yu Y., Yu D.: Cure kinetics, microheterogeneity, and mechanical properties of the high-temperature cure of vinyl ester resins. *Journal of Applied Polymer Science*, **92**, 1124–1133 (2004).
DOI: [10.1002/app.13686](https://doi.org/10.1002/app.13686)
- [6] Mortaigne B., Feltz B., Laurens P.: Study of unsaturated polyester and vinylester morphologies using excimer laser surface treatment. *Journal of Applied Polymer Science*, **66**, 1703–1714 (1997).
DOI: [10.1002/\(SICI\)1097-4628\(19971128\)66:9<1703::AID-APP8>3.0.CO;2-H](https://doi.org/10.1002/(SICI)1097-4628(19971128)66:9<1703::AID-APP8>3.0.CO;2-H)
- [7] Karger-Kocsis J., Gryshchuk O., Schmitt S.: Vinylester/epoxy-based thermosets of interpenetrating network structure: An atomic force microscopic study. *Journal of Materials Science*, **38**, 413–420 (2003).
DOI: [10.1023/A:1021855228253](https://doi.org/10.1023/A:1021855228253)
- [8] Grishchuk S., Karger-Kocsis J.: Hybrid thermosets from vinyl ester resin and acrylated epoxidized soybean oil (AESO). *Express Polymer Letters*, **5**, 2–11 (2011).
DOI: [10.3144/expresspolymlett.2011.2](https://doi.org/10.3144/expresspolymlett.2011.2)
- [9] Avilés F., Cauch-Rodríguez J. V., Rodríguez-González J. A., May-Pat A.: Oxidation and silanization of MWCNTs for MWCNT/vinyl ester composites. *Express Polymer Letters*, **5**, 766–776 (2011).
DOI: [10.3144/expresspolymlett.2011.75](https://doi.org/10.3144/expresspolymlett.2011.75)

Poly(ethylene glycol)-poly(tetrahydrofuran)-poly(ethylene glycol) triblock copolymer: Synthesis, crystallization behavior and novel morphology

W. W. Fan, X. D. Fan, W. Tian*, X. Q. Liao, W. B. Zhang, C. G. Mu, J. Kong

The Key Laboratory of Space Applied Physics and Chemistry, Ministry of Education and Shaanxi Key Laboratory of Macromolecular Science and Technology, School of Science, Northwestern Polytechnical University, Xi'an, 710072, P. R. China

Received 15 November 2012; accepted in revised form 26 January 2013

Abstract. Poly(ethylene glycol)-poly(tetrahydrofuran)-poly(ethylene glycol) (PEG-PTHF-PEG) triblock copolymer was synthesized by ring-opening polymerization of ethylene oxide using sodium alcoholate of PTHF as the macroinitiator. Its crystallization behavior and formation mechanisms of different crystal structures were studied. The study showed that the molecular weight of PEG-PTHF-PEG exhibited a significant effect on its crystallization: that is, with the increase of the copolymer's molecular weight, the crystallizability of PTHF blocks decreased gradually, which led to the transition of copolymer from crystalline-crystalline to crystalline-amorphous. By adjusting the total molecular weight of triblock copolymer, the crystallization process can be effectively controlled, and as a result, different spherulite structures were obtained. Particularly, when PTHF blocks became amorphous, novel double concentric spherulites were observed. The morphological structures were studied by differential scanning calorimetry (DSC), Fourier transform infrared spectroscopy (FTIR), scanning electron microscope (SEM), polarized optical microscopy (POM), and its crystalline process was investigated.

Keywords: polymer synthesis, molecular engineering, crystallization, double concentric spherulites

1. Introduction

With the rapid development of polymer synthesis strategy, various block copolymers with desired structures were obtained, and at the same time, the crystallization behavior for these copolymers was investigated accordingly [1–5]. Block copolymers, consisting of both crystalline and amorphous segments were widely recognized that their crystallization processes and the resulting crystal morphologies can be significantly influenced by microphase separation in melt [6, 7]. However, block copolymers, consisting of different crystalline segments such as the double crystalline block copolymers, usually exhibit much more complicated crystalliza-

tion behaviors [8, 9], including confined crystallization [10–13], competitive or interactive crystallization and so on [14–16]. For these block copolymers, the overall crystallization behavior is influenced by block ratios, nucleation types, crystallization kinetics and characteristics of the individually folded chains [5, 17–19]. Recently, Li *et al.* [20] reported that the order of block crystallization in double crystalline block copolymers could be switched by adjusting total molecular weight, even while holding the block length ratio fixed. Their work revealed a convenient method to regulate the crystallization for double crystalline block copolymers, with the advantage that the block ratio or the content of each

*Corresponding author, e-mail: happytw_3000@163.com
© BME-PT

component could be maintained. However, for the various block copolymers with different structures and components, the molecular weight dependence of their crystallization behavior should be diverse and much more complicated. Unfortunately, reports on this field are still inadequate till now.

Recently, with the comprehensive investigations on crystallization process for block copolymers, the high order structures containing crystal lamellae were frequently discovered [6, 21–25], where several types of spherulites with unusual morphologies such as ring banded spherulite, spherical granular aggregates and double concentric spherulites have been reported [14, 15, 26–31]. Especially, the double concentric spherulites were only found in poly(ethylene oxide)/poly(ϵ -caprolactone) PEG/PCL block copolymer up to now [14, 26–29]. This complex morphology contains an initial spherulite in center and a concentric outside spherulite with different crystal structure. The inner and outer spherulites are templated by crystallization of different blocks. Lately, Shi *et al.* [32] also reported a similar morphology in their study on PEG/PMMA blend and the formation was due to the different orientations of PEG crystal lamellae caused by the intervention of phase separation during crystallization process. Considering that the polymer's phase separation can also significantly affect the crystallization process of crystalline-amorphous block copolymers, double concentric spherulites may be expected to exist in crystalline-amorphous block copolymers. However, related studies were rarely reported up to now.

In this work, we synthesized several poly(ethylene glycol)-poly(tetrahydrofuran)-poly(ethylene glycol) (PEG-PTHF-PEG) as model triblock copolymers, where the copolymer's block ratios are equal and fixed, but their molecular weights are different. We focused our attention on controlling the copolymer's crystallization behavior via adjusting total molecular weight with a fixed block ratio to understand the detailed mechanism of the formation of crystalline structures for these triblock copolymers. The copolymer's crystallization process was monitored by DSC and their crystal morphologies were inspected via POM. The research data confirmed that the copolymer's molecular weight was a key factor to affect its crystallization behavior. Especially, when the molecular weight of triblock copolymer reached a certain value, the PTHF block became completely amorphous. Meanwhile the interesting double con-

centric spherulites in this triblock copolymer were found. As far as we known, it was the first time that double concentric spherulites had been observed in crystalline-amorphous block copolymer. Our study could provoke more considerations in regulating the crystallization of block copolymers and may also be helpful for the design of crystalline materials.

2. Experimental section

2.1. Materials

Tetrahydrofuran (THF, Alfa Aesar, USA) was refluxed over Sodium (Na, 98%, Sinopharm Chemical Reagent Co., Ltd, China) and freshly distilled before use. Ethylene oxide (EO, 98.0%) was purchased from Sinopharm Chemical Reagent Co., Ltd (China) and stored with 3 Å molecular sieve in sealed preserving condition. Sodium hydride (57–63% oil dispersion, Alfa Aesar, USA) was washed by anhydrous THF three times. Ethanol (99.5%, Sinopharm Chemical Reagent Co., Ltd, China), perchloric acid (70–72%, Sinopharm Chemical Reagent Co., Ltd, China), dichloromethane (99.5%, Sinopharm Chemical Reagent Co., Ltd, China), *n*-hexane (99.5%, Sinopharm Chemical Reagent Co., Ltd, China), Amberlite IR-120(+) resin (Alfa Aesar, USA) and acetic anhydride (98.5%, Sinopharm Chemical Reagent Co., Ltd, China) were all used as received.

Two types of Poly(ethylene glycol), denoted as PEG2000 and PEG8000, were purchased from Sinopharm Chemical Reagent Co., Ltd (China). Three types of hydroxyl-ended PTHF, denoted as PTHF1600, PTHF2600 and PTHF3900 (numbers stand for weight average molecular weights and the below is same), were purchased from Sigma (USA). For removing the residual moisture, the polymers were first dissolved in toluene and then distilled. The collected product was dried under the vacuum until a constant weight was obtained. The polymer's molecular weights were determined by size exclusion chromatography with multi-angle laser lights (SEC-MALLS).

2.2. Synthesis of triblock copolymers (PEG-PTHF-PEG)

Triblock copolymers with different molecular weights were synthesized by ring-opening polymerization of ethylene oxide using sodium alcoholate of PTHF as the macroinitiator. Preparation was car-

Table 1. Molecular weight and composition of polymers

Sample ^a	M _w ^b	M _w /M _n ^b	M _n ^b	M _n ^c	PTHF in copolymer ^c [wt%]
PTHF1600	1660	1.25	1330	972	100
PTHF2600	2590	1.21	2140	1349	100
PTHF3900	3960	1.20	3300	2928	100
Block2950	2950	1.11	2660	–	48.6
Block4900	4910	1.09	4500	–	47.1
Block7800	7810	1.08	7200	–	47.8

^aBlock2950, Block4900 and Block7800 were synthesized from PTHF1600, PTHF2600 and PTHF3900 respectively.

^bDetermined by GPC-MALLS.

^cPEG/ PTHF weight ratio in the block copolymer was determined from the area ratio of the ¹H NMR peaks at 3.64 ppm (due to the PEG blocks) and 1.62 ppm (due to the PTHF block). Then the content of PTHF in copolymer could be calculated.

ried out in an autoclave (300 mL, parr4566, Parr Instrument Company, USA), specifically, for Block7800, 40.07 g PTHF3900 was first dissolved in 50 mL of anhydrous THF, and then transferred into the autoclave. At the same time, 1.11 g of NaH was added and the air in autoclave was displaced subsequently by nitrogen. The temperature was raised to 60°C and retained for 3 h to make sure that NaH reacts with PTHF completely. After the reaction, the autoclave was cooled down in ice-water bath, and the atmosphere inside was replaced by nitrogen again. By that time, 48.00 g EO was added in, the temperature was increased to 75°C under stirring with a speed of 80 r/min for 12 h. The polymerization was terminated by addition of 20 g of Amberlite IR-120(+) resin and stirred for another 6 hours. The final product was obtained by filtration from the resin into n-hexane (500 mL) at 0°C. ¹H NMR (300 MHz, δ ppm, CDCl₃): 3.64 (b, OCH₂CH₂O), 3.41 (b, OCH₂CH₂CH₂CH₂O), 1.62 (b, OCH₂CH₂CH₂CH₂O).

Two other block copolymers, denoted as Block2950 and Block4900, were synthesized following the similar procedure. The polymer's characteristics parameters were listed in Table 1.

2.3. Characterization

Molecular weights and polydispersity indexes of three triblock copolymers were determined by SEC-MALLS (DAWN EOS, Wyatt Technology Corporation, USA) equipped with a highly cross-linked styrene/divinylbenzene gel column (500 Å, 5 μm). HPLC grade THF was used as the eluent with a flow rate of 0.5 mL/min at 25°C. Samples were first

diluted with THF to a concentration of ca. 5 wt% and then filtered through a filter of 0.22 μm. The refractive index increment (dn/dc) value of samples was obtained by an Optilab rEX detector at 25°C through a batch model.

Structural compositions of the PEG-PTHF-PEG triblock copolymers were determined by ¹H NMR and ¹³C NMR on a Bruker 300 MHz spectrometer (Bruker Corporation, Germany) with DMSO as solvent and tetramethylsilane as the internal standard.

2.4. Thermal and morphological characterization

Differential scanning calorimetry (DSC) measurement was conducted on a TA 2910 instrument (TA Instruments, USA) calibrated with indium. The sample (3~5 mg) treated by freeze drying was encapsulated in aluminum pan and characterized with a heating rate of 5°C/min. Polarized optical microscopy (POM) inspection was performed with a Nikon E400 optical microscope (Nikon Corporation, Japan) equipped with crossed polarizers (λ = 546 nm) and a camera system. Fourier transform infrared spectroscopy (FTIR) was utilized to measure the characteristic vibrational bands of crystalline structures on a Nicolet iS10 instrument (Nicolet Instrument Corporation, USA). The samples for POM measurements were prepared by casting three drops of a 5 wt% tetrahydrofuran solution of the copolymer on a clean cover glass and then dried in a vacuum oven for 24 h at room temperature. KBr plate coated with sample was used for FTIR sample preparation. All samples before measurements were melted at 80°C for 10 min and then maintained at the crystallization temperature for 48 h. For in situ POM and time-dependent FTIR measurements, the samples were melted at 80°C for 10 min and then characterized immediately.

3. Results and discussion

3.1. Synthesis of triblock copolymers

According to the literatures, there are mainly two approaches to prepare PEG/PTHF block copolymers. One is to utilize chemical reaction to couple the hydroxyl-terminated PEO and PTHF segments [33–35], and the other one is to terminate the cationic polymerization of THF by methoxypolyethylene glycols [36, 37]. However, none of them can be regarded as the ideal synthetic strategies to prepare a qualified copolymer, typically, with a well-defined

structure. Because the first method has a limited efficiency for coupling reaction and is time-consuming, and the latter requires a critically equal feed ratio, and frequently, the target block copolymer is often end-capped with methyl group. For this reason, we used anionic ring opening polymerization to prepare PEG-PTHF-PEG triblock copolymers, where hydroxyl-terminated PTHF carrying sodium alcoholate was used as the macroinitiator. As can be seen in Figure 1, the ionization of the terminal hydroxyl groups in PTHF can be accomplished via addition of sodium hydride, however, the ionized hydroxyls in PTHF should be lower than 50% for preventing initiator precipitation from THF. It was found that as the exchange reaction between alcoholate active center and hydroxyl group is much faster than the initiation rate, which leads to simultaneous growth of polymer chains [38, 39]; therefore, accurate feeding of NaH is not necessary and as a result, the synthesis process becomes much easier to operate.

Using our synthetic approach, three triblock copolymers were prepared and their molecular weights and polydispersity indexes were listed in Table 1. The results of ^{13}C NMR measurements, as shown in Figure 2, also proved that the copolymer's structures are correct. The signals at 29.76 ppm which can be assigned as the carbon of methylene-ended group in PTHF disappeared completely in PEG-PTHF-PEG triblock copolymer, indicating all the PTHF being linked with PEG segment successfully.

Additionally, it should be pointed out that the polymerization is technically demanding. All solvents and reagents must be rigorously dried and degassed, and the purity of the sodium hydride is critical. In the synthesis, a possible problem is that NaOH, which is formed from reaction of NaH with water, can induce the polymerization of EO and result in homopolymers. To get a deep scope, we added 0.5 wt% of water into EO during polymer synthesis. The final product was contaminated by PEG diol, and had a lower molecular weight as well as a broader

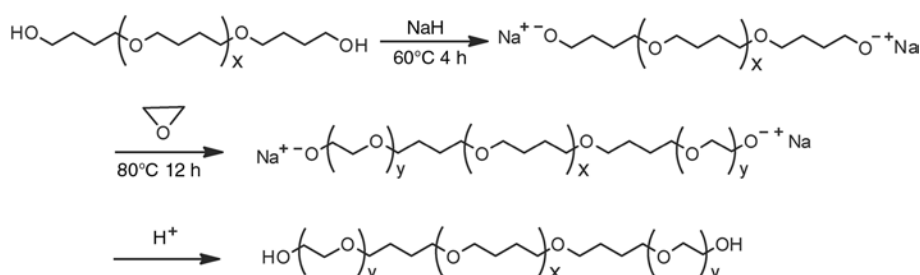


Figure 1. Synthesis route of triblock copolymers

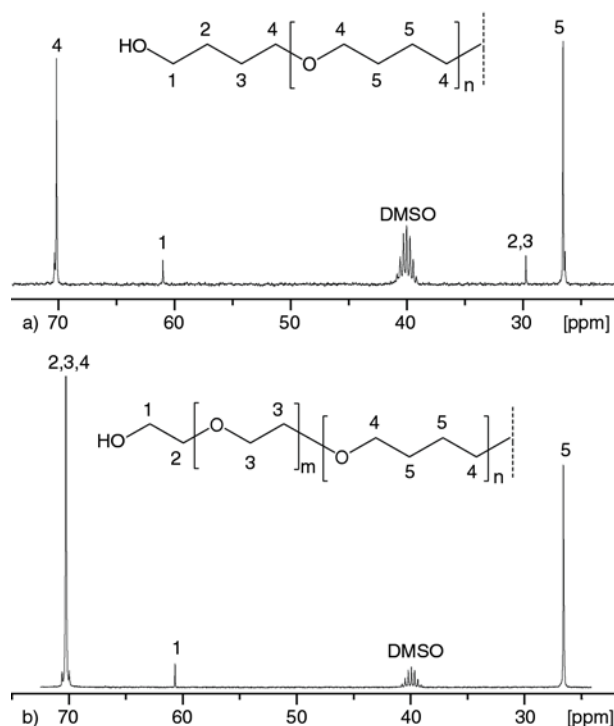


Figure 2. ^{13}C NMR spectrum of PTHF2600 (a) and Block4900 (b)

molecular weight distribution. Especially, an additional peak of PEG diol emerged in SEC elution curve, as shown in Figure 3b. With the strict control of processing conditions to avoid the contamination of moisture, triblock copolymer with desired molecular weight and narrow molecular weight distribution could be obtained, as shown in Figure 3c. Evidently, the peaks of PEG contaminant in SEC elution curve vanished. On the other hand, though the molecular weight of triblock copolymer could not be calculated by ^1H NMR spectra as the chemical shift of terminal groups was covered, the block ratio was easy to calculate and the value agreed well with that calculated from the number average molecular weight determined by SEC-MALLS, suggesting that the triblock copolymer was successfully prepared with high purity, which is very critical for the next crystallization behavior study.

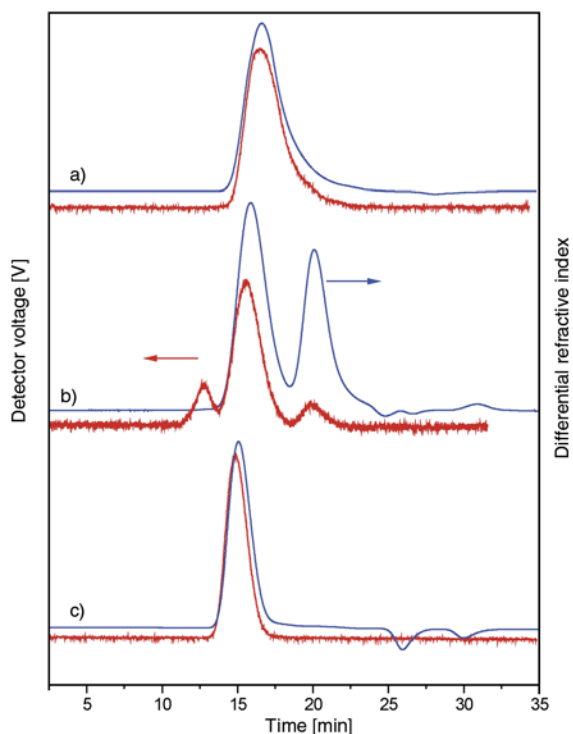


Figure 3. MALLS-SEC elution curves of polymers: (a) PTHF3900; (b) block copolymer synthesized with moisture in monomers; (c) Block 7800

3.2. Relationship between crystallization and molecular weight

The melting and crystallization behaviors of the PEG-PTHF-PEG triblock copolymers were investi-

Table 2. The T_m and T_c of the triblock copolymers

Sample	Cooling T_c [°C]		Heating T_m [°C]	
	PTHF	PEG	PTHF	PEG
PTHF1600	5.7	–	21.8	–
Block2950	–3.3	7.1	18.6	25.6
Block4900	7.4 ^a		23.5	33.3
Block7800	–	16.6	–	45.0
PEG2000	–	35.7	–	54.3

^aOverlapping peaks

gated by DSC. Homopolymers of PEG2000 and PTHF1600 were also tested for comparison. Figure 4 shows the DSC curves collected from the measurements. The melting temperature (T_m) and crystallization temperature (T_c) are listed in Table 2.

As can be seen from Figure 4, both PEG and PTHF homopolymers are crystalline, and exhibited a fine single peak during crystallization and melting processes. In addition, the T_m of PTHF is much lower than that of PEG with the similar molecular weight, which is consistent with the literature [37]. Compared with the homopolymers, Block2950 exhibits two exothermic and two endothermic peaks. Both exothermic and endothermic peaks are rather lower than those of the homopolymers. That is because crystallization of one block significantly affects the crystallization behavior of the other block, and the crystallinity of both blocks tend to

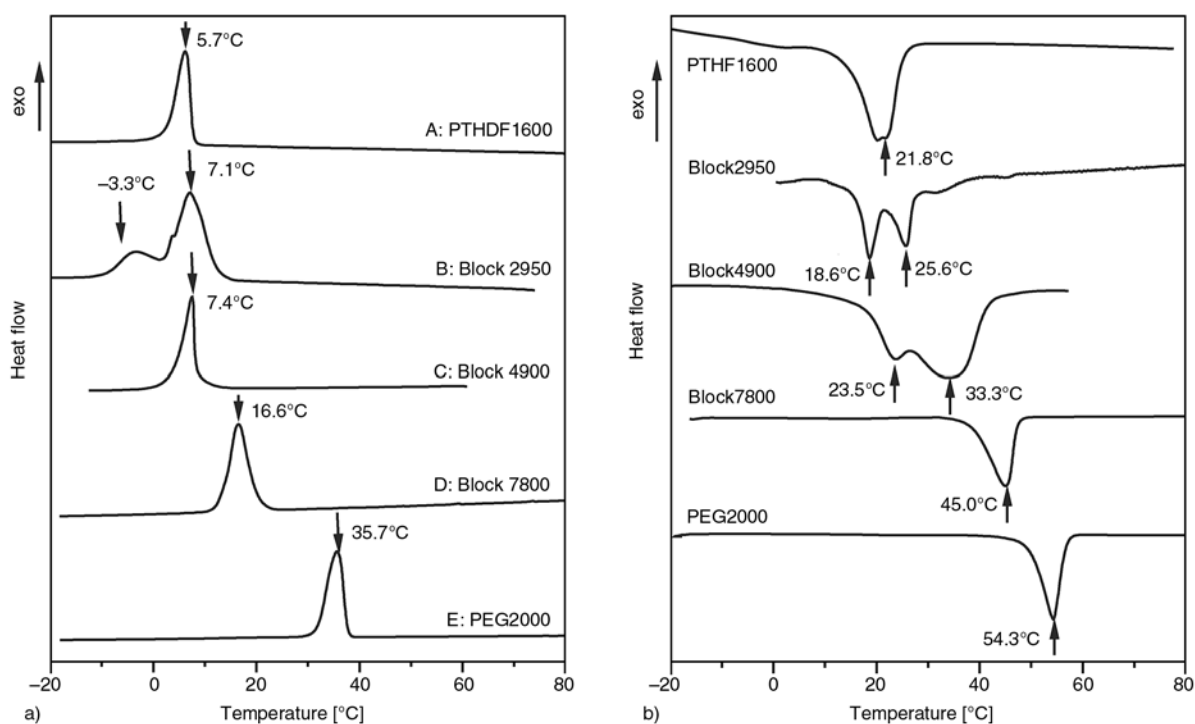


Figure 4. DSC cooling scans (a) and heating scans (b) at 5°C/min after melting at 80°C for the indicated polymers

decrease with the composition of the other block [5]. The peaks at lower temperatures can be assigned to the crystallization or crystalline melting of PTHF blocks, and the peaks at higher temperatures can be assigned to PEG block's contribution. However, the crystallization and melting temperatures for PTHF blocks are 9 and 3.2°C below that of PTHF1600, respectively. As the molecular weight in both homo- and copolymers is basically the same, the result may indicate that the nucleation of the PTHF blocks in the copolymer was hindered by the PEG lamellae formed earlier, which are covalently bonded to them.

Following the increase in molecular weight, Block4900 exhibits a single exothermic peak at 7.4°C but two endothermic peaks at 23.5 and 33.3°C respectively. From our FTIR results (discussed below), both PEG and PTHF blocks proved to be crystallizable, so the single exothermic peak may come from the overlap of the DSC signals during cooling. By the use of slower cooling rates, this overlap effect still cannot be overcome even at a cooling rate of 0.5°C/min, where a clear tailing area of crystallization was observed as shown in Figure 5. This may be related to the fact that, once the crystallization of PEG blocks started, it was quickly followed by the crystallization of the PTHF block which can be nucleated by PEG blocks, and this phenomenon was also reported in the literature by Müller *et al.* [40]. Besides, the intensity of endothermic peak of PTHF block was much weaker than that of PEG

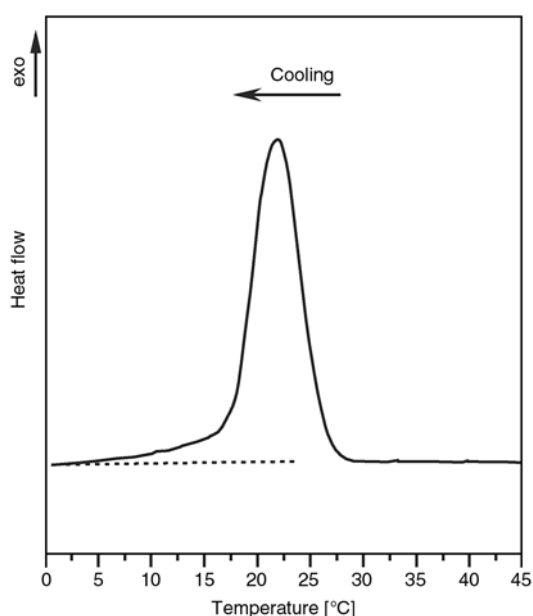


Figure 5. DSC cooling scan of Block4900 at 0.5°C/min

blocks in Block4900, suggesting that the crystallizability of PTHF blocks was reduced following the increase in the molecular weight.

When the molecular weight increased further to 7800, Block7800 shows a single peak for both endothermic and exothermic processes. The melting point was also beyond the melting temperature range of homo-PTHF as reported before [37]. Therefore, it was reasonable to attribute the endothermic and exothermic peaks to PEG blocks only, and PTHF blocks may not be crystallizable in this molecular weight range. The conclusion was further confirmed by our FTIR data below. Additionally, it is worthwhile to note that, whether for PTHF or PEG blocks, the melting point and crystallization temperature were lower than that of the homopolymers with the same molecular weight. That is because the crystallization of PTHF and PEG segments in the block copolymers were restricted by each other. In the case of Block7800, even the PTHF blocks were non-crystallizable, the covalently bonded molten PTHF segments could also hinder the crystallization process of PEG blocks.

In order to further study the crystallization behavior, FTIR spectroscopy was used to monitor the crystallization process. The absorption band at 843 cm^{-1} in FTIR spectrum could be used to characterize the crystallization of PEG segments [27, 28]. On the other hand, characteristic absorption at 564 cm^{-1} for homo-PTHF crystals was also obtained by time-dependent FTIR measurements during crystallization (Figure 6a). The intensity of absorption at 746 cm^{-1} could also characterize the crystallization of PTHF, but it should be noted that this absorption was inherent in PTHF even if it is totally amorphous. For triblock copolymers that crystallized at -30°C , as shown in Figure 6b, following the increase in molecular weight, the absorption intensities at 746 and 564 cm^{-1} gradually decreased implying the deduction of PTHF block's crystallization ability. Particularly, the disappearance of absorption band at 564 cm^{-1} for Block7800 demonstrates strongly that the PTHF blocks were totally amorphous within this copolymer. The result is in agreement with the data of DSC.

The change of crystallization behavior of block copolymers should be due to the different molecular weight dependence of crystallization of PEG and PTHF blocks, respectively. As molecular weight increased, the melting point of PEG blocks increased

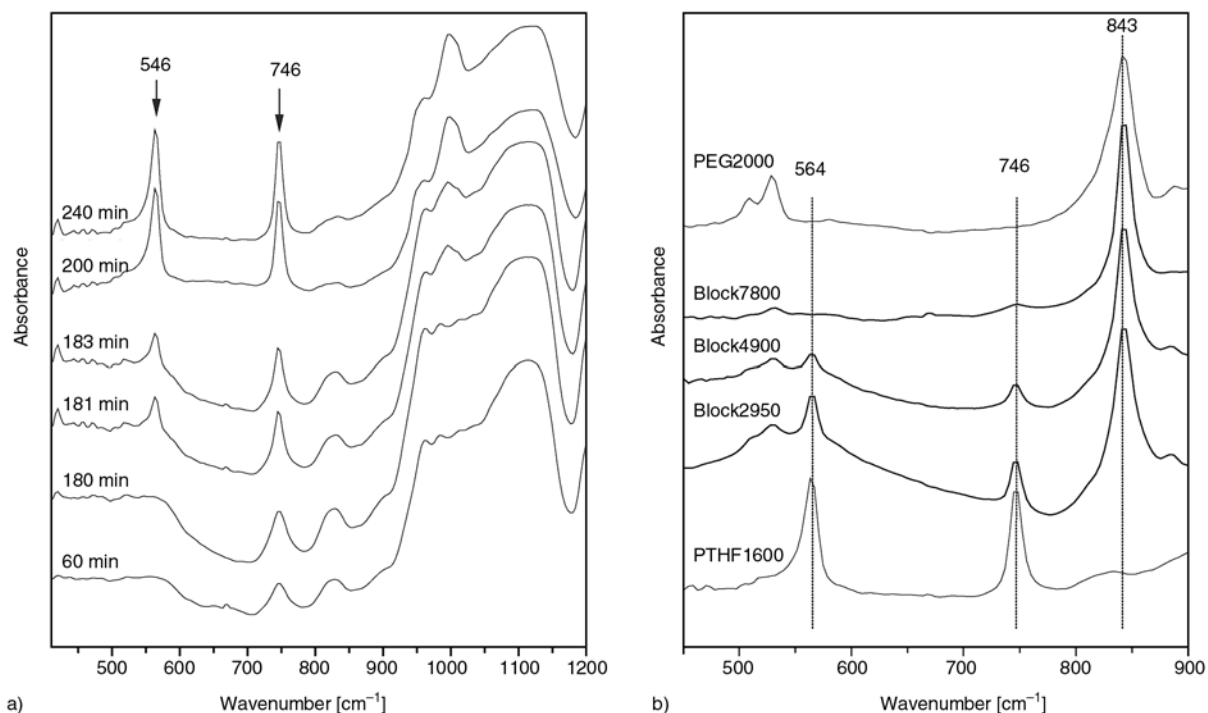


Figure 6. Time-dependent FTIR spectra (a) of PTHF2600 and FTIR spectra (b) for the indicated polymers

more rapidly than that of PTHF blocks, resulting in the further separation of melting temperatures of the two blocks (Figure 4). In general, when the melting temperatures of both blocks are near enough, a coincident crystallization phenomenon of both blocks can be obtained. Conversely, when the melting temperature of one block is far from the other, the latter crystallized component undergoes a confined crystallization process [5]. So the crystallization of PTHF blocks was steadily confined by PEG blocks as molecular weight increased, even causing PTHF blocks to be amorphous.

3.3. Spherulite morphology

For inspection of triblock copolymer's crystalline morphology changing with the molecular weight, the POM was employed to obtain micrographs of spherulites as shown in Figure 7. Obviously, the spherulites formed in Block2950 and Block4900 are closely packed with a broad size distribution. Similar phenomenon was observed in crystallization of PEG homopolymer, which may be attributed to different particle size fractions and the change of heat transfer under fast cooling conditions [41]. These spherulites exhibit negative Maltese crosses patterns, suggesting that the highest refractive index in the spherulites was tangential and coincided with the chain direction [27, 42]. Clearly, the amorphous

domains were intercalated in the spherulites leading to minor color aberration of birefringent pattern and fibrillar crystals grow in the radial direction with short branches.

Following the increase in the molecular weight to 7800, the numbers of spherulites were obviously reduced. Upon deepening quench to -30°C , fewer loose negative spherulites with much smaller size can be observed (Figure 7c). After carefully examining Figure 7c, it was found that many lamellar stacks were formed around the spherulites and seemed to orient randomly. Interestingly, when the crystallization temperature changed from -30 to 4°C , the original spherulites kept a negative pattern but the lamellar outside oriented to form Maltese crosses with positive pattern (Figure 7d). As a result, the spherulites morphology of double concentric spherulites was observed, which was similar with the report of double crystalline PEG/PCL block copolymer [26–28].

3.4. Formation of double concentric spherulites

According to our study, crystallization process of Block7800 was able to lead to double concentric spherulites with T_c in range from 4 to 25°C or wider. The formation process of double concentric spherulites was studied by POM during isothermal crystallization at 22°C . The real-time micrographs

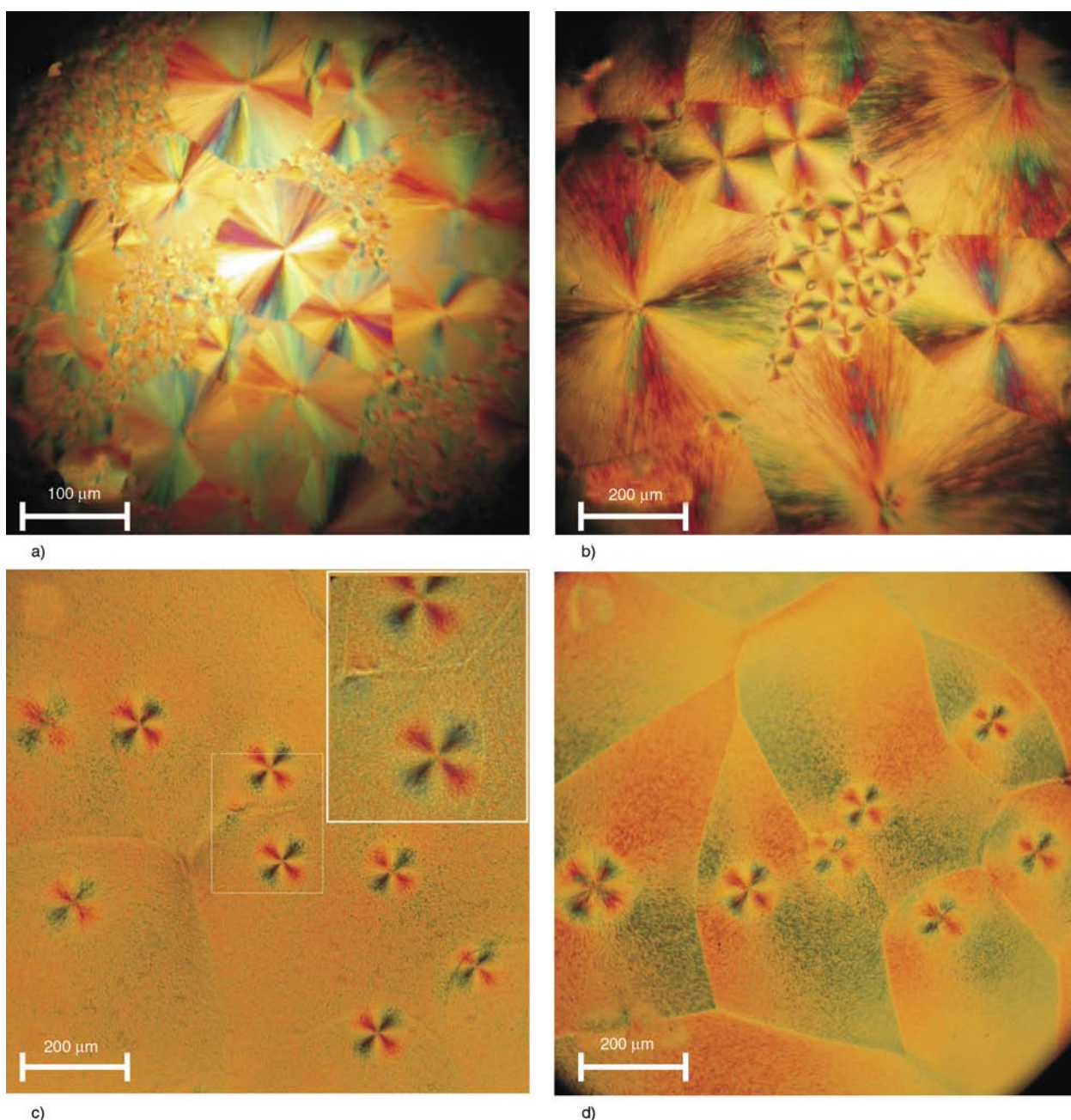


Figure 7. POM micrographs: (a) Block2950, $T_c = -30^\circ\text{C}$; (b) Block 4900, $T_c = -30^\circ\text{C}$; (c) Block7800, $T_c = -30^\circ\text{C}$; (d) Block7800, $T_c = 4^\circ\text{C}$. All samples were melted at 80°C for 10 min and then transferred into thermostat to crystallize for 48 h.

of Block7800 are presented in Figure 8. As shown, there are two spherulites with double concentric birefringence patterns formed in sequence, signed as spherulites 1 and spherulite 2 respectively. The formation processes of both of them are as follows. At the beginning, small initial spherulite with clear outline emerged and the birefringence showed a negative character. The growth rates G of the initials spherulites in spherulite 1 and 2 were approximately 2.6 and 2.4 $\mu\text{m/s}$ respectively, as shown in Figure 9. As the spherulite grew up, a new positive

birefringence diffused on the edge of the spherulite, resulting in the formation of a relatively perfect spherulite with a double concentric feature. After that, the initial spherulite continued to grow and the growth rate remained constant. Before long, the initial spherulite stopped growing and its outline became indistinct. Moreover, the final sizes of both initial spherulites were similar (about 100 μm). At the same time, the outer birefringence pattern spread out with a much higher growth rate (8.4 $\mu\text{m/s}$ for spherulite 1 and 7.4 $\mu\text{m/s}$ for spherulite 2) to cover

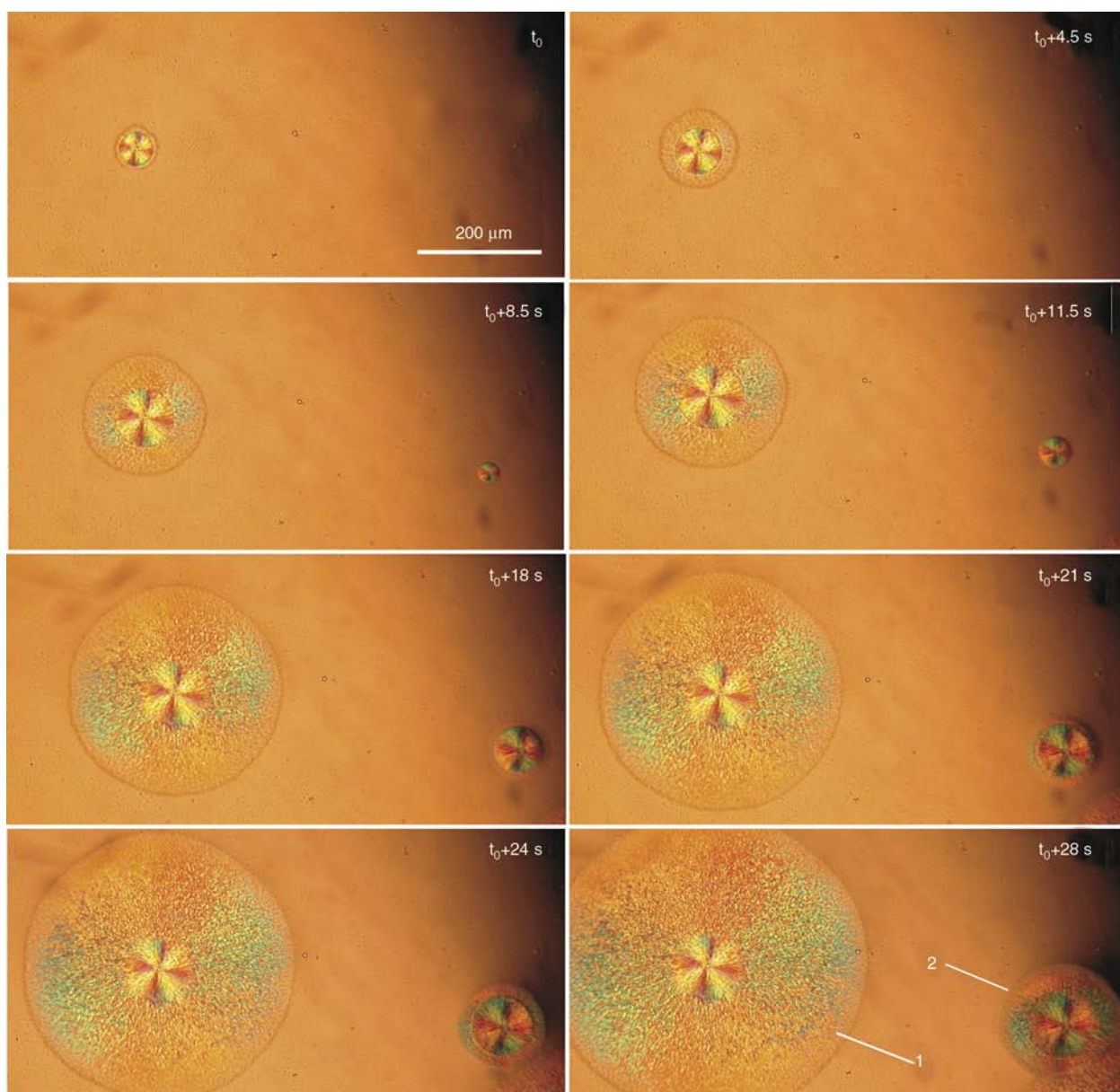


Figure 8. In situ POM micrographs of the isothermal crystallization of Block7800 at 22°C

all the remaining regions of sample. Finally, the whole birefringence was invariable, and the final texture of the double concentric spherulites was constructed.

The growth of double concentric spherulites was further investigated by time-dependent FTIR spectroscopy as presented in Figure 10. To ensure the accuracy, measurements were repeated at least 3 times with different areas of sample detected. Results of FTIR confirmed that the PTHF segments were totally amorphous because there is no characteristic absorption at 564 cm^{-1} and the absorption at 746 cm^{-1} is constant. This means that both inner and outer spherulites were formed by the crystallization of PEG segments. This point was well illustrated by the continuous increase of vibrational

bands at 843 cm^{-1} during the whole crystallization process.

This morphology was further investigated by SEM, as shown in Figure 11. In the initial spherulites, interlocked fibrillar structures were formed and the orientation was roughly in accordance with the radial direction (see Figure 11a). While, at the boundary between the initial spherulite and the outer part, the reticular structure vanished quickly. Then a new morphology containing dot-like and worm-like microzones formed, and spread out to construct the outer part of double concentric spherulites (see Figure 11b and Figure 11c).

As it has been observed that the initial spherulites formed in Block7800 at 22°C had a constant final size of about $100\text{ }\mu\text{m}$ even if the nucleation times

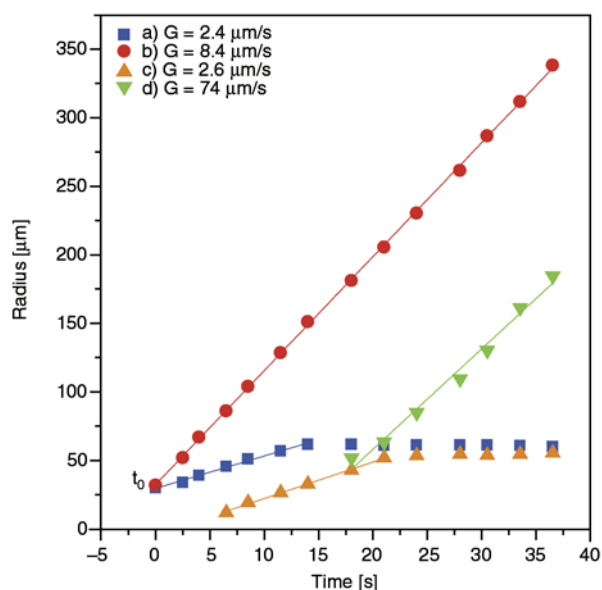


Figure 9. Spherulite radius plotted against the crystallization time at 22°C for Block7800. The slope of the straight line was taken as the radius growth rate G . (a) initial spherulite of spherulite 1. (b) outer part of spherulite 1. (c) initial spherulite of spherulite 2. (d) outer part of spherulite 2.

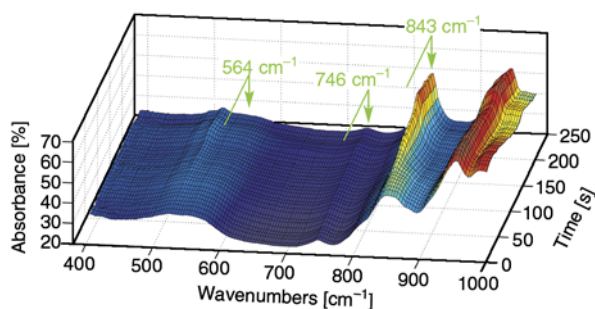


Figure 10. Time-dependent FTIR spectra of Block7800 at 22°C

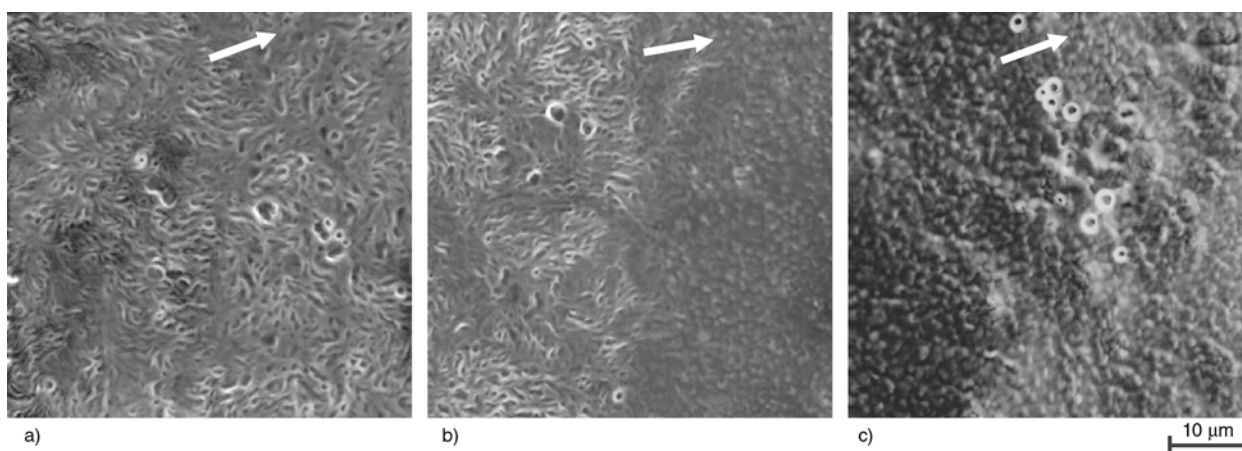


Figure 11. Morphology in different regions of double concentric spherulites (formed at 4°C) observed by SEM: (a) morphology of initial spherulite; (b) morphology at the boundary between the initial spherulite and outer part; (c) morphology of the outer part. The arrow indicates the radial direction from the center.

were different, we made an attempt to change the size of initial spherulite by adjusting the cooling rate during non-isothermal crystallization process. Morphologies of Block7800 with different cooling rates are illustrated in Figure 12. Unexpectedly, though the size of the outer part of double concentric spherulites increased dramatically as cooling rate slowed down, only feeble enlargement of initial spherulites was observed when the cooling rate dropped from 20 to 2°C/min. After size reach about 100 μm, the initial spherulites did not grow any more even with an extremely slow cooling rate of 0.1°C/min. Therefore, there was a size limit of initial spherulite. According to our observations in both isothermal crystallization processes with different temperatures and non-isothermal crystallization processes with different cooling rates, the maximum size was about 100 μm in diameter.

Herein, our work reveals the fact that the crystals of semicrystalline ABA triblock copolymers are able to form double concentric spherulites under polarized-light microscopy. That is quite different from previous work [26–28], in which the morphologies of inner and outer parts of concentric spherulites are dominated by the crystallization of different segments of double crystalline block copolymer. This phenomena is confused and puzzling, but really interesting.

Though the triblock copolymer was prepared with high purity as mentioned above, we still suspected that the product contained traces of PEG diol. To find out whether the PEG diol was the cause of the formation of double concentric spherulites, we blended Block7800 with a small amount of PEG8000 and

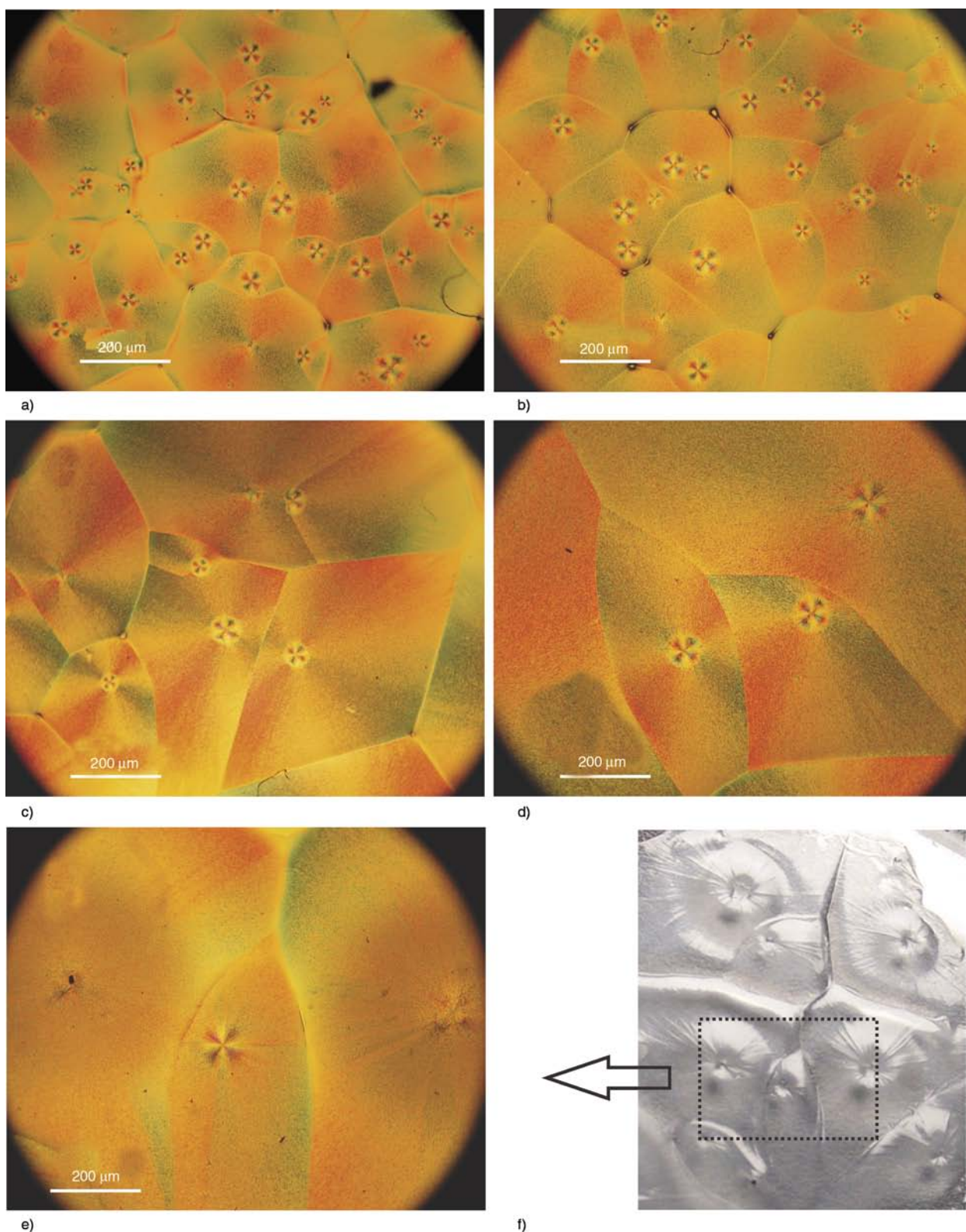


Figure 12. Morphologies of Block7800 formed at different cooling rates: (a) (20°C/min), (b) (10°C/min), (c) (2°C/min), (d) (0.5°C/min) and (e) (0.1°C/min) were taken by POM; (f) (0.1°C/min) was taken by camera with the micro distance photography pattern

PEG2000 (10 wt%) respectively. The PEG diols added in had a similar molecular weight of Block7800 or its PEG blocks. The morphologies are shown in Figure 13. As shown, the formation of

double concentric spherulites was difficult in both blends. The initial spherulites were much smaller and hard to find. If the PEG diol caused the formation of double concentric spherulites, it should

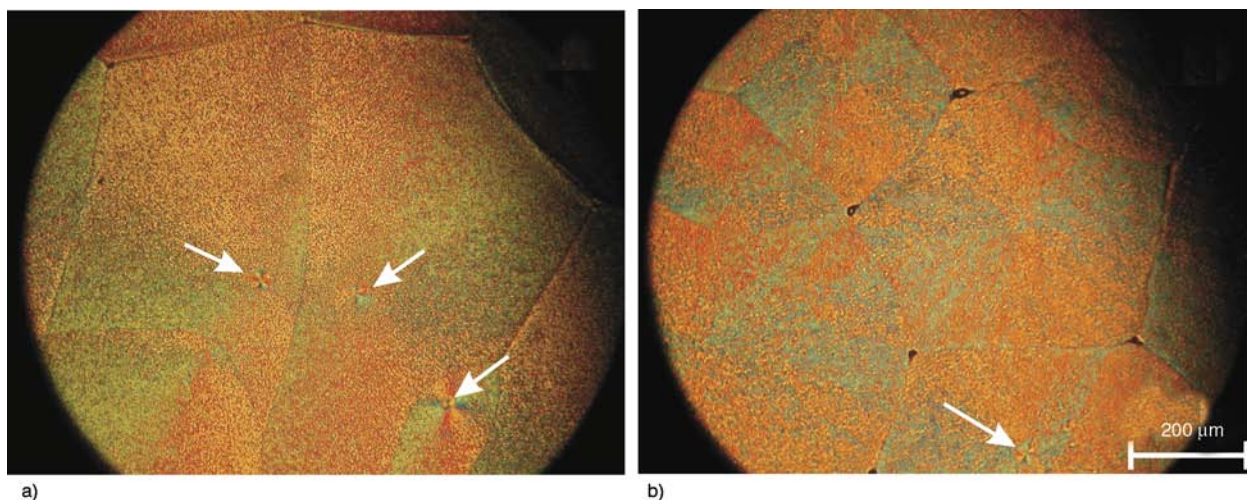


Figure 13. POM micrographs: (a) Block7800 containing 10 wt% PEG2000; (b) Block7800 containing 10 wt% PEG8000. Polymer blends were melted at 80°C for 10 min and crystallized at 22°C. The arrows point to the initial spherulites.

nucleate and crystallize earlier than block copolymer to form the initial spherulite, and then the number of the initial spherulite (or double concentric spherulites) would increase as PEG diol is added. This conjecture was denied by our observation. Hence the PEG diol was not the cause of the formation of double concentric spherulites.

Recently, Shi *et al.* [43] reported the concentric structure which was caused by the lamellar orientation inversion of PEG crystals due to the intervention of phase separation. When phase separation occurred, due to the dynamic competition between phase separation and crystallization process, PEG lamellas tended to array along different directions and formed different spherulitic morphology forms [32, 44]. As Block7800 was proved to be crystalline-amorphous, the resulting crystal morphologies can be significantly influenced by microphase separation [5, 6]. That may help to explain the formation of double concentric spherulites discovered in our study. Possible formation mechanism may be as follows. Firstly, the initial spherulites were formed and grew up, following the nucleation in polymer melt. After a certain period, phase separation occurred. Then the PEG lamellar crystals were formed with the intervention of phase separation and adopted a different orientation, resulting in the formation of the outer part with a much different birefringence pattern. However, the detailed phase separation progress still needs to be intensively studied and the reason why the initial spherulite had a size limit has not been found out. Further investigation is in

progress, and the results will be published elsewhere.

4. Conclusions

In this study, PEG-PTHF-PEG triblock copolymers with different molecular weights but the same block ratio were conveniently synthesized. The hydroxyl-ended PTHF reacted with NaH firstly, and its sodium alcoholate was used as macroinitiator for anionic ring-opening polymerization of EO to obtain PEG-PTHF-PEG triblock copolymer.

The molecular weights of triblock copolymers with the same block ratio exhibited a significant effect on their crystallization behavior, and even led to the transition of triblock copolymer from double crystalline to a crystalline-amorphous. At a low molecular weight of 2950, both PEG and PTHF blocks were crystallizable, and after the molecular weight of block copolymer increased to 4900, crystallization of PEG blocks became dominant. With the molecular weight increased to 7800, only PEG blocks could crystallize and PTHF blocks were amorphous, where double concentric spherulites were formed. In addition, there is an upper limit for the size of the initial spherulite in double concentric spherulites.

Acknowledgements

This work was supported by the National Science Foundations of China (No. 21274116 and No. 21004049) and scientific research project of Ministry of Industry and Information Technology of P. R. China (No. J142011A001).

References

- [1] Hamley I. W.: Crystallization in block copolymers. *Advances in Polymer Science*, **148**, 113–137 (1999). DOI: [10.1007/3-540-48836-7_2](https://doi.org/10.1007/3-540-48836-7_2)
- [2] Müller A. J., Balsamo V., Arnal M. L.: Nucleation and crystallization in diblock and triblock copolymers. *Advances in Polymer Science*, **190**, 1–63 (2005). DOI: [10.1007/12_001](https://doi.org/10.1007/12_001)
- [3] Nandan B., Hsu J.-Y., Chen H.-L.: Crystallization behavior of crystalline – Amorphous diblock copolymers consisting of a rubbery amorphous block. *Journal of Macromolecular Science Part C: Polymer Reviews*, **46**, 143–172 (2006). DOI: [10.1080/15321790600646802](https://doi.org/10.1080/15321790600646802)
- [4] Müller A. J., Arnal M. L., Balsamo V.: Crystallization in block copolymers with more than one crystallizable block. *Lecture Notes in Physics*, **714**, 229–259 (2007). DOI: [10.1007/3-540-47307-6_13](https://doi.org/10.1007/3-540-47307-6_13)
- [5] Castillo R. V., Müller A. J.: Crystallization and morphology of biodegradable or biostable single and double crystalline block copolymers. *Progress in Polymer Science*, **34**, 516–560 (2009). DOI: [10.1016/j.progpolymsci.2009.03.002](https://doi.org/10.1016/j.progpolymsci.2009.03.002)
- [6] Shin D., Shin K., Aamer K. A., Tew G. N., Russell T. P., Lee J. H., Jho J. Y.: A morphological study of a semicrystalline poly(L-lactic acid-*b*-ethylene oxide-*b*-L-lactic acid) triblock copolymer. *Macromolecules*, **38**, 104–109 (2005). DOI: [10.1021/ma0481712](https://doi.org/10.1021/ma0481712)
- [7] Hong S., MacKnight W. J., Russell T. P., Gido S. P.: Structural evolution of multilayered, crystalline–amorphous diblock copolymer thin films. *Macromolecules*, **34**, 2876–2883 (2001). DOI: [10.1021/ma002032c](https://doi.org/10.1021/ma002032c)
- [8] Sun L., Liu Y., Zhu L., Hsiao B. S., Avila-Orta C. A.: Pathway-dependent melting in a low-molecular-weight polyethylene-*block*-poly(ethylene oxide) diblock copolymer. *Macromolecular Rapid Communications*, **25**, 853–857 (2004). DOI: [10.1002/marc.200300320](https://doi.org/10.1002/marc.200300320)
- [9] Lin M.-C., Wang Y.-C., Chen J.-H., Chen H.-L., Müller A. J., Su C. J., Jeng U.-S.: Orthogonal crystal orientation in double-crystalline block copolymer. *Macromolecules*, **44**, 6875–6884 (2011). DOI: [10.1021/ma201124u](https://doi.org/10.1021/ma201124u)
- [10] Maglio G., Migliozzi A., Palumbo R.: Thermal properties of di- and triblock copolymers of poly(L-lactide) with poly(oxyethylene) or poly(ϵ -caprolactone). *Polymer*, **44**, 369–375 (2003). DOI: [10.1016/S0032-3861\(02\)00764-4](https://doi.org/10.1016/S0032-3861(02)00764-4)
- [11] Sun L., Liu Y., Zhu L., Hsiao B. S., Avila-Orta C. A.: Self-assembly and crystallization behavior of a double-crystalline polyethylene-*block*-poly(ethylene oxide) diblock copolymer. *Polymer*, **45**, 8181–8193 (2004). DOI: [10.1016/j.polymer.2004.09.063](https://doi.org/10.1016/j.polymer.2004.09.063)
- [12] Weiyu C., Tashiro K., Hanesaka M., Takeda S., Masunaga H., Sasaki S., Takata M.: Relationship between morphological change and crystalline phase transitions of polyethylene–poly(ethylene oxide) diblock copolymers, revealed by the temperature-dependent synchrotron WAXD/SAXS and infrared/Raman spectral measurements. *The Journal of Physical Chemistry B*, **113**, 2338–2346 (2009). DOI: [10.1021/jp8092435](https://doi.org/10.1021/jp8092435)
- [13] Bogdanov B., Vidts A., Schacht E., Berghmans H.: Isothermal crystallization of poly(ϵ -caprolactone–ethylene glycol) block copolymers. *Macromolecules*, **32**, 726–731 (1999). DOI: [10.1021/ma980226a](https://doi.org/10.1021/ma980226a)
- [14] Shiomi T., Imai K., Takenaka K., Takeshita H., Hayashi H., Tezuka Y.: Appearance of double spherulites like concentric circles for poly(ϵ -caprolactone)-*block*-poly(ethylene glycol)-*block*-poly(ϵ caprolactone). *Polymer*, **42**, 3233–3239 (2001). DOI: [10.1016/S0032-3861\(00\)00597-8](https://doi.org/10.1016/S0032-3861(00)00597-8)
- [15] Takeshita H., Fukumoto K., Ohnishi T., Ohkubo T., Miya M., Takenaka K., Shiomi T.: Formation of lamellar structure by competition in crystallization of both components for crystalline–crystalline block copolymers. *Polymer*, **47**, 8210–8218 (2006). DOI: [10.1016/j.polymer.2006.09.043](https://doi.org/10.1016/j.polymer.2006.09.043)
- [16] Nojima S., Fukagawa Y., Ikeda H.: Interactive crystallization of a strongly segregated double crystalline block copolymer with close crystallizable temperatures. *Macromolecules*, **42**, 9515–9522 (2009). DOI: [10.1021/ma901964a](https://doi.org/10.1021/ma901964a)
- [17] Castillo R. V., Müller A. J., Raquez J.-M., Dubois P.: Crystallization kinetics and morphology of biodegradable double crystalline PLLA-*b*-PCL diblock copolymers. *Macromolecules*, **43**, 4149–4160 (2010). DOI: [10.1021/ma100201g](https://doi.org/10.1021/ma100201g)
- [18] Salmerón Sánchez M., Mathot V. B. F., Vanden Poel G., Gómez Ribelles J. L.: Effect of the cooling rate on the nucleation kinetics of poly(L-lactic acid) and its influence on morphology. *Macromolecules*, **40**, 7989–7997 (2007). DOI: [10.1021/ma0712706](https://doi.org/10.1021/ma0712706)
- [19] Lee L.-B. W., Register R. A.: Equilibrium control of crystal thickness and melting point through block copolymerization. *Macromolecules*, **37**, 7278–7284 (2004). DOI: [10.1021/ma049143m](https://doi.org/10.1021/ma049143m)
- [20] Li S., Myers S. B., Register R. A.: Solid-state structure and crystallization in double-crystalline diblock copolymers of linear polyethylene and hydrogenated polynorbornene. *Macromolecules*, **44**, 8835–8844 (2011). DOI: [10.1021/ma201951j](https://doi.org/10.1021/ma201951j)
- [21] Sun J., Chen X., He C., Jing X.: Morphology and structure of single crystals of poly(ethylene glycol)–poly(ϵ -caprolactone) diblock copolymers. *Macromolecules*, **39**, 3717–3719 (2006). DOI: [10.1021/ma0603074](https://doi.org/10.1021/ma0603074)

- [22] Hobbs J. K., Register R. A.: Imaging block copolymer crystallization in real time with the atomic force microscope. *Macromolecules*, **39**, 703–710 (2006). DOI: [10.1021/ma0514020](https://doi.org/10.1021/ma0514020)
- [23] Zhu L., Cheng S. Z. D., Calhoun B. H., Ge Q., Quirk R. P., Thomas E. L., Hsiao B. S., Yeh F., Lotz B.: Crystallization temperature-dependent crystal orientations within nanoscale confined lamellae of a self-assembled crystalline–amorphous diblock copolymer. *Journal of the American Chemical Society*, **122**, 5957–5967 (2000). DOI: [10.1021/ja000275e](https://doi.org/10.1021/ja000275e)
- [24] Li C. Y., Cheng S. Z. D., Ge J. J., Bai F., Zhang J. Z., Mann I. K., Chien L.-C., Harris F. W., Lotz B.: Molecular orientations in flat-elongated and helical lamellar crystals of a main-chain nonracemic chiral polyester. *Journal of the American Chemical Society*, **122**, 72–79 (1999). DOI: [10.1021/ja993249t](https://doi.org/10.1021/ja993249t)
- [25] Kong J., Fan X., Qiao W., Xie Y., Si Q., Tang Y.: Study of a skin-core type of crystallinity distribution within polyethylene specimen crystallized under high pressure. *Polymer*, **46**, 7644–7651 (2005). DOI: [10.1016/j.polymer.2005.04.108](https://doi.org/10.1016/j.polymer.2005.04.108)
- [26] He C., Sun J., Deng C., Zhao T., Deng M., Chen X., Jing X.: Study of the synthesis, crystallization, and morphology of poly(ethylene glycol)–poly(ϵ -caprolactone) diblock copolymers. *Biomacromolecules*, **5**, 2042–2047 (2004). DOI: [10.1021/bm049720e](https://doi.org/10.1021/bm049720e)
- [27] He C., Sun J., Zhao T., Hong Z., Zhuang X., Chen X., Jing X.: Formation of a unique crystal morphology for the poly(ethylene glycol)–poly(ϵ -caprolactone) diblock copolymer. *Biomacromolecules*, **7**, 252–258 (2006). DOI: [10.1021/bm050627f](https://doi.org/10.1021/bm050627f)
- [28] He C., Sun J., Ma J., Chen X., Jing X.: Composition dependence of the crystallization behavior and morphology of the poly(ethylene oxide)–poly(ϵ -caprolactone) diblock copolymer. *Biomacromolecules*, **7**, 3482–3489 (2006). DOI: [10.1021/bm060578m](https://doi.org/10.1021/bm060578m)
- [29] Zhu W., Xie W., Tong X., Shen Z.: Amphiphilic biodegradable poly(CL-*b*-PEG-*b*-CL) triblock copolymers prepared by novel rare earth complex: Synthesis and crystallization properties. *European Polymer Journal*, **43**, 3522–3530 (2007). DOI: [10.1016/j.eurpolymj.2007.04.024](https://doi.org/10.1016/j.eurpolymj.2007.04.024)
- [30] Albuerné J., Márquez L., Müller A. J., Raquez J. M., Degée P., Dubois P., Castelletto V., Hamley I. W.: Nucleation and crystallization in double crystalline poly(*p*-dioxanone)-*b*-poly(ϵ -caprolactone) diblock copolymers. *Macromolecules*, **36**, 1633–1644 (2003). DOI: [10.1021/ma025766t](https://doi.org/10.1021/ma025766t)
- [31] Jiang S., He C., An L., Chen X., Jiang B.: Crystallization and ring-banded spherulite morphology of poly(ethylene oxide)-*block*-poly(ϵ -caprolactone) diblock copolymer. *Macromolecular Chemistry and Physics*, **205**, 2229–2234 (2004). DOI: [10.1002/macp.200400204](https://doi.org/10.1002/macp.200400204)
- [32] Shi W., Yang J., Zhang Y., Luo J., Liang Y., Han C. C.: Lamellar orientation inversion under dynamic interplay between crystallization and phase separation. *Macromolecules*, **45**, 941–950 (2012). DOI: [10.1021/ma202046c](https://doi.org/10.1021/ma202046c)
- [33] Hevus I., Kohut A., Voronov A.: Amphiphilic invertible polyurethanes: Synthesis and properties. *Macromolecules*, **43**, 7488–7494 (2010). DOI: [10.1021/ma101175k](https://doi.org/10.1021/ma101175k)
- [34] Niu L., Nagarajan R., Guan F., Samuelson L. A., Kumar J.: Biocatalytic synthesis of multi-block copolymer composed of poly(tetrahydrofuran) and poly(ethylene oxide). *Journal of Macromolecular Science Part A: Pure and Applied Chemistry*, **43**, 1975–1981 (2006). DOI: [10.1080/10916460600997744](https://doi.org/10.1080/10916460600997744)
- [35] Ikeda T., Lee W. K., Ooya T., Yui N.: Thermodynamic analysis of inclusion complexation between α -cyclodextrin-based molecular tube and poly(ethylene oxide)-*block*-poly(tetrahydrofuran)-*block*-poly(ethylene oxide) triblock copolymer. *The Journal of Physical Chemistry B*, **107**, 14–19 (2003). DOI: [10.1021/jp020817+](https://doi.org/10.1021/jp020817+)
- [36] Pomel C., Leborgne C., Cheradame H., Scherman D., Kichler A., Guegan P.: Synthesis and evaluation of amphiphilic poly(tetrahydrofuran-*b*-ethylene oxide) copolymers for DNA delivery into skeletal muscle. *Pharmaceutical Research*, **25**, 2963–2971 (2008). DOI: [10.1007/s11095-008-9698-9](https://doi.org/10.1007/s11095-008-9698-9)
- [37] De Witte I. C., Goethals E. J.: Synthesis and block-specific complexation of poly(ethylene oxide)–poly(tetrahydrofuran)–poly(ethylene oxide) triblock copolymers. *Polymers for Advanced Technologies*, **10**, 287–292 (1999). DOI: [10.1002/\(SICI\)1099-1581\(199905\)10:5<287::AID-PAT877>3.0.CO;2-F](https://doi.org/10.1002/(SICI)1099-1581(199905)10:5<287::AID-PAT877>3.0.CO;2-F)
- [38] Libera M., Trzebiecka B., Kowalczyk A., Watach W., Dworak A.: Synthesis and thermoresponsive properties of four arm, amphiphilic poly(*tert*-butyl-glycidyl-ether)-*block*-polyglycidol stars. *Polymer*, **52**, 250–257 (2011). DOI: [10.1016/j.polymer.2010.12.001](https://doi.org/10.1016/j.polymer.2010.12.001)
- [39] Feng X.-S., Taton D., Chaikof E. L., Gnanou Y.: Toward an easy access to dendrimer-like poly(ethylene oxide)s. *Journal of the American Chemical Society*, **127**, 10956–10966 (2005). DOI: [10.1021/ja0509432](https://doi.org/10.1021/ja0509432)

- [40] Müller A. J., Albuérne J., Marquez L., Raquez J-M., Degée P., Dubois P., Hobbs J., Hamley I. W.: Self-nucleation and crystallization kinetics of double crystalline poly(*p*-dioxanone)-*b*-poly(ϵ -caprolactone) diblock copolymers. *Faraday Discuss*, **128**, 231–252 (2005).
DOI: [10.1039/b403085k](https://doi.org/10.1039/b403085k)
- [41] Delahaye N., Duclos R., Saiter J. M.: Characterization of PEG6000 phase transitions: Influence of kinetic conditions. *International Journal of Pharmaceutics*, **157**, 27–34 (1997).
DOI: [10.1016/S0378-5173\(97\)00207-X](https://doi.org/10.1016/S0378-5173(97)00207-X)
- [42] Yin J. H., Mo Z. S.: *Modern polymer physics* (in Chinese). Science Press, Beijing (2001).
- [43] Shi W., Cheng H., Chen F., Liang Y., Xie X., Han C. C.: Concentric ring pattern formation in a competing crystallization and phase separation process. *Macromolecular Rapid Communications*, **32**, 1886–1890 (2011).
DOI: [10.1002/marc.201100490](https://doi.org/10.1002/marc.201100490)
- [44] Shi W., Han C. C.: Dynamic competition between crystallization and phase separation at the growth interface of a PMMA/PEO blend. *Macromolecules*, **45**, 336–346 (2011).
DOI: [10.1021/ma201940m](https://doi.org/10.1021/ma201940m)

Comparative study of filler influence on polylactide photooxidation

S. Bocchini^{1*}, A. Frache²

¹Center for Space Human Robotics@PoliTo, Istituto Italiano di Tecnologia, C.so Trento 21 10129 Turin, Italy

²Dipartimento di Scienza Applicata e Tecnologia, Politecnico di Torino sede di Alessandria, Viale Teresa Michel 5, 15121 Alessandria, Italy

Received 17 November 2012; accepted in revised form 26 January 2013

Abstract. Polylactide (PLA) based nanocomposites of organically modified montmorillonite and micro-talc based micro-composites were prepared with different compositions and were UV-light irradiated under artificial accelerated conditions representative of solar irradiation. The chemical modifications resulting from photo-oxidation were followed by infrared (IR) and ultraviolet (UV)-visible spectroscopies. The infrared analysis of PLA photooxidation shows the formation of a band at 1847 cm^{-1} due to the formation of anhydrides. The filler addition provokes an increase of anhydride formation rate dependent on filler nature, amount and dispersion degree on the matrix. The main factors that influence oxidation rate are the total extension of polymer/filler interfacial area and the presence of transition metal impurities of clays.

Keywords: nanocomposites, polylactide, photooxidation, biopolymers

1. Introduction

In the market of biodegradable polymers, polylactide (PLA) is undoubtedly one of the most promising candidates for further developments as it is not only biodegradable but also produced from renewable resources, such as sugar beet and corn starch. Due to its attractiveness, PLA is currently receiving considerable attention for conventional applications such as packaging, textile fibres and more recently, as (nano)composites for technical applications. Unfortunately the range of application of PLA is severely limited because of low glass transition temperature (around $55\text{--}60^\circ\text{C}$) thus in response to the demand for extending the range of PLA applications the main route to increase mechanical and thermomechanical properties of PLA was the preparation of PLA-based nanocomposites [1–5] achieving remarkable improvements of the polymer properties observed even at nanofiller content as low as

3–5 wt% without the loss of biodegradability [6, 7], or the addition of a nucleating/reinforcing agent such as talc [8] or calcium sulphate anhydrite [9, 10].

The resistance to ultraviolet (UV) light is a key factor for most outdoor applications of polymeric materials. In the last few years, the impact of light on polymer/clay nanocomposites has been studied [11–19]. The clay nanocomposites show a significant reduction of the oxidation induction time (OIT). In a previous series of papers concerning the photooxidation of montmorillonite/polypropylene [13–15] several hypotheses have been proposed to explain the oxidative degradation of these materials. The reduction of the OIT could result from the adsorption of antioxidants onto the nanofiller, and/or a catalytic effect of transition metal impurities of nanofillers, and also from additional initiation routes due to the oxidation of the organic modifiers in the

*Corresponding author, e-mail: sergio.bocchini@iit.it
© BME-PT

nanofillers. The most probable hypothesis was the presence of interactions between the nanofillers and the stabilizers: the antioxidants can be adsorbed on the nanofillers thus preventing their protective action [13–18]. In a previous article the photo-oxidation mechanism of PLA [19] was investigated. The proposed mechanism was the formation of anhydride functional groups by a radical peroxide mechanism (Figure 1). In the presence of moisture the successive anhydride hydrolysis promotes degradation of polylactide. These findings were confirmed by Gardette *et al.* [20]. In the same article they also explain that under the conditions typical of outdoor exposure other reaction such as Norrish II are improbable.

The photooxidation of PLA-nanocomposites with different types of nanoparticles was also studied [19]. As a general statement the nanoparticle addition does not change the mechanism but, on the basis of the nanoparticle type, an increase of anhydride formation was noted. The main factor responsible for this acceleration was identified in the presence of transition metal ions contained in the nanofillers as impurities and involved in the cat-

alytic hydroperoxide decomposition. The main effect of the eventual clay organic modifiers is instead the increase of initial dispersion of the nanofillers with a consequent increased interaction between nanofiller and PLA.

The aim of the present work is to study the effect of clay nanoparticles concentration on the photooxidation behaviour of PLA, moreover a comparison with a micrometric traditional filler such as talc often used in combination with PLA because of its nucleation properties [8, 21], and that already provoked an increase in photooxidation in polyonlefin/talc composites [22, 23], was made.

2. Experimental

2.1. Materials

Poly(L-lactic acid) ‘NatureWorks® PLA Polymer 3051D’, average molecular weight 160 kDa, ratio 96% L-Lactide to 4% D-Lactide units was purchased from Natureworks Minneapolis Minnesota (USA). Industrial microtalc masterbatch ‘PLA NA BIO L 6951’ with a composition of 30 wt% of micro-sized talc content based and 70 wt% of ‘NatureWorks® PLA Polymer 3051D’ was purchased from

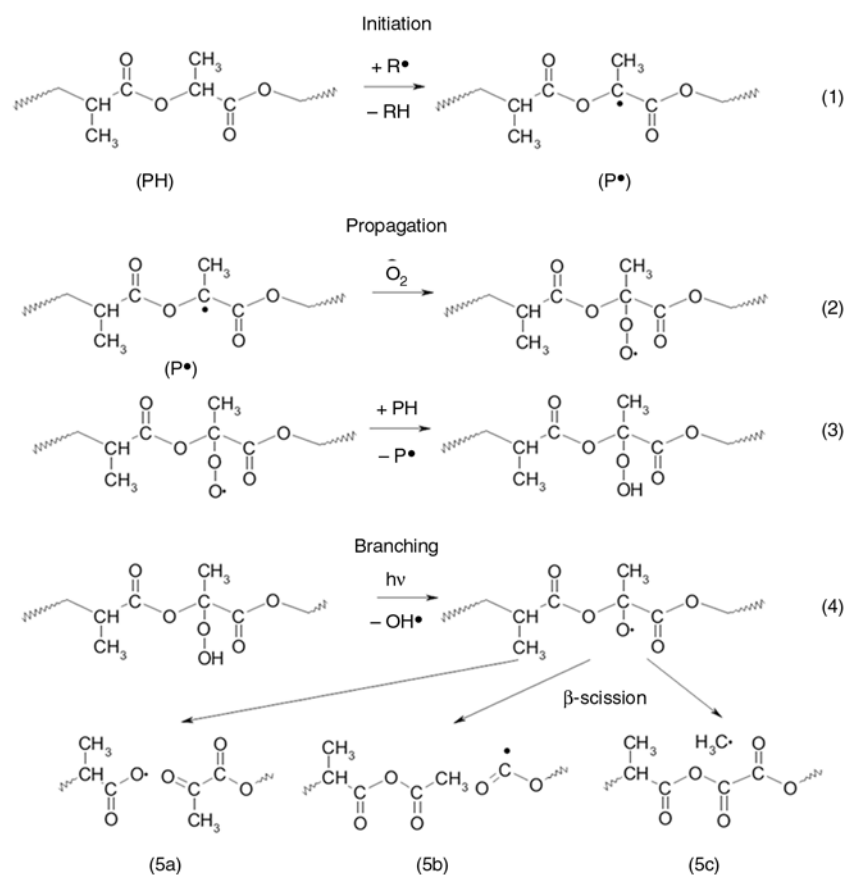
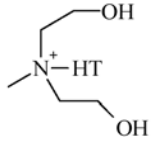
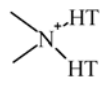


Figure 1. Radical oxidation process of irradiated PLA samples: hydroperoxide chain propagation and formation of anhydrides by photolysis of hydroperoxide [19] (Reproduced with permission)

Table 1. Characteristics of particles/nanoparticles used

Commercial name	Cloisite®30B	Cloisite®20A	NA BIO L6951
Type of nanoparticles	Montmorillonite		Talc
Chemical formula	$[\text{Al}_{3.34}\text{Mg}_{0.66}](\text{Si}_8\text{O}_{20})(\text{OH})_4^{-0.66}$	$\text{Mg}_3\text{Si}_4\text{O}_{10}(\text{OH})_2$	
Organic modifier type [wt%]			None
	30 ^{a)}	38 ^{a)}	–
Platelet length [μm]	0.5 ^{b)}		2–10 ^{c)}
EDS ^{d)}			
Si [wt%]	26.0±1.8	25.5±2.5	29.9±1.7
Al [wt%]	10.1±0.4	9.2±0.8	18.5±0.3
O [wt%]	59.5±2.7	61.2±3.8	51.6±1.7
Mg [wt%]	1.1±0.1	1.3±0.2	–
Fe [wt%]	3.1±1.1	2.3±0.4	–
Na [wt%]	0.1±0.1	0.5±0.2	–
Code	Cl30B	Cl20A	T

HT – hydrogenated linear alkyl chains: C8~18

^{a)}wt% obtained by calcination at 800°C

^{b)}On the basis of estimation from sodium montmorillonite precursor [24]

^{c)} Estimated from SEM analyses (Figure 4)

^{d)}Qualitative elemental analysis of by energy dispersive X-ray spectroscopy (EDS) wt% on the basis of the inorganic part (excluding organic modifiers)

Polyone Belgium SA Assesse (Belgium). Two different commercial nanoclays (Southern Clay Products, Inc.), Cloisite®30B (Cl30B), sodium montmorillonite modified with bis-(2-hydroxyethyl) methyl tallow alkyl ammonium cations and Cloisite®20A (Cl20A), sodium montmorillonite modified with dimethyl, dehydrogenated tallow, quaternary ammonium cations were used. The characteristics of the particles used in this work are listed in Table 1.

Prior to melt blending, PLA and talc masterbatch were dried at 80°C under vacuum until residual moisture measured by Karl Fisher was lower than 190 ppm. Similarly clays were dried at 100°C under vacuum until moisture lower than 400 ppm measured by Karl Fisher was achieved.

2.2. Materials processing

The composites were prepared via melt-processing using a Leistritz co-rotating twin screw extruder ($d = 18$ mm, $l/d = 40$). The flow was 4.0 kg/h, and the rotation speed was 150 rpm. The residence time was about 50 s. The screw configuration with the temperature profile from the feeding zone to the die, previously optimized to obtain the best filler dispersion inside PLA, is reported in Table 2.

The samples were prepared by direct addition of the different nanofiller and masterbatch in the feeding zone. The compositions are listed in Table 3. The

code PLAXX gives the filler content expressed as XX wt%.

$30 \times 30 \times 1$ mm³ samples for wide angle X-ray analyses were prepared using a hot-plate hydraulic press at 190°C. A pressure of 100 bar was applied for 1 minute and thus the samples were cooled at 10 °C min⁻¹.

Film samples for photooxidation were prepared from pellets using a hot-plate hydraulic press at 190 °C using a pressure of 100 bar for 1 minute and rapidly cooled to room temperature to avoid oxidation/degradation and PLA crystallization, in order to have oxygen saturation during film photo-oxidation the film thickness was kept under 15–20 μm .

2.3. Materials photooxidation process

Irradiations of specimens at $\lambda > 300$ nm were carried out in air in a SEPAP 12/24 unit at 45°C. This apparatus is equipped with four medium-pressure mercury lamps with borosilicate envelope which filters wavelengths below 300 nm and it is designed for the study of polymer photodegradation in artificial conditions that are relevant to natural outdoor weathering [25].

2.4. Characterization

Wide angle X-ray diffractograms (WAXS) were recorded at room temperature in the range 1–30°

Table 2. Description of screw and temperature profiles from the feeding zone to the die

Element ^{a)}	Type ^{b)}	Number of element	Length	Temperature [°C]
GFF 2-30-90	Conveying	1	90	Cooled
GFA 2-30-30	Conveying	2	60	195
KB4 2-15-30 RE	Kneading	2	30	195
KB4 2-15-60 RE	Kneading	2	30	192
KB4 2-15-90 RE	Kneading	2	30	192
GFA 2-30-60	Conveying	1	60	192
GFA 2-30-30	Conveying	1	30	190
GFA 2-20-30	Conveying	1	30	190
KB4 2-15-30 RE	Kneading	1	15	190
KB4 2-15-60 RE	Kneading	1	15	190
KB4 2-15-90 RE	Kneading	1	15	185
GFA 2-30-30	Conveying	1	30	185
GFA 2-15-15 LI	Kneading	1	15	185
GFA 2-20-30	Conveying	2	60	180
KB4 2-15-30 RE	Kneading	1	15	180
KB4 2-15-60 RE	Kneading	2	30	180
KB4 2-15-90 RE	Kneading	1	15	175
GFA 2-30-60	Conveying	1	60	175
GFA 2-20-60	Conveying	1	60	170
GFA 2-15-30	Conveying	1	30	165

^{a)}the letters stand for G – corotating; F (in the second position) – conveying; A – free-meshing; F (in the third position) – freely cut; KB – kneading block; RE – conveying. LI – counterflow

^{b)}Conveying block: the three numbers indicate the thread length, the pitch length, and the screw element respectively; kneading block: the three numbers stand for the kneading block, the thread number, the length of the kneading block, and the twisting angle of the kneading segments.

Table 3. Composition of melt-blended samples

Samples name	Cloisite [wt%] (Type)	Masterbatch [wt%] of talc
PLA	–	–
PLA2.5CI20A	2.5 (CI20A)	–
PLA5CI20A	5.0 (CI20A)	–
PLA2.5CI30B	2.5 (CI30B)	–
PLA5CI30B	5.0 (CI30B)	–
PLA5T	–	5.0
PLA10T	–	10.0

(2θ) (step size = 0.02°, scanning rate = 2 s/step) by using filtered Cu K_{α} radiation ($\lambda = 1.54 \text{ \AA}$) with a Thermo ARL diffractometer X-tra 48.

Specimens for Transmission Electron Microscopy (TEM) characterizations were microtomed at -196°C with an Ultramicrotome Leica UCT to obtained thickness about 90 nm. The grid was 50 meshes, coated with SPI-Chem™ Pioloform® B Resin. The analyses were performed with a Philips CM 120 microscope.

Scanning Electron Microscopy (SEM) was carried out on the cryogenic fracture surfaces of the 0.6 mm specimens previously coated by sputtering with gold, using a Leo 14050 VP SEM apparatus. Energy dispersive X-ray spectroscopy (EDS) was performed on the original CI20A and CI30B and on microtalc

obtained by calcination of PLA NA BIO L 6951. The results were the statistic of 12 different sampling.

Infrared spectra (FT-IR) of films were recorded with a Perkin-Elmer Spectrum GX Infrared Spectrometer. Spectra were obtained using 16 scans and a 4 cm^{-1} resolution.

Photooxidation of PLA was followed by the intensity of the 1847 cm^{-1} peak $\nu_{\text{C=O}}$ of anhydride, which was plotted as a function of time; to avoid differences due to film thickness, it was normalized using the infrared (IR) absorption band at 2997 cm^{-1} $\nu_{\text{C-H}}$ (asymmetric ν_{CH_3} band of PLA).

UV-visible spectra (UVvis) of films were recorded on a Shimadzu UV-2101 PC spectrometer equipped with an integrating sphere.

3. Results and discussions

3.1. Morphology

WAXS is one of the methods used to assess the dispersion of clay in a polymeric matrix. From the position of the first peak in the diffractogram the distance d_{001} , commonly named ‘interlayer-spacing’, is calculated using the Bragg’s law. The WAXS analyses of PLA-nanocomposites used in this work

were already reported in a previous work [26], thus for the sake of brevity only a resume of the results is reported. The d_{001} for C120A, C130B and the respective PLA nanocomposites are reported in Table 4. C120A is characterized by a first diffraction peak at $2\theta = 3.5^\circ$ [19] corresponding to an interlayer distance (d_{001}) related to the presence of the organic modifier molecules between clay layers and accounting for a $d_{001} = 2.5$ nm. When C120A is blended in PLA a shift of this peak to lower angles is observed, corresponding to the increase of the C120A interlayer distance to 3.5 nm, indicating the formation of an intercalated structure. In the case of PLAC130B the d_{001} peak shifts from the original value of $2\theta = 4.7^\circ$ (1.8 nm) of C130B to $2\theta = 2.4^\circ$ (3.6 nm) showing that also in this case an intercalated structure is achieved. Moreover, there is no sensible effect of clay concentration on X-rays diffractograms either in the case of C120A or in that of C130B in the range of concentration of Table 3. As expected there are no traces of PLA crystalline structure both for PLA (Figure 2) and for PLA nanocomposites based on clay nanoparticles, as already reported in literature for PLA/organically modified montmorillonite nanocomposites [19, 26–28]. These observations are in perfect agreement with the previously published data [5, 19, 27–29] on similar materials.

The WAXS pattern of PLA is characterized by a broad band with maximum at $2\theta \approx 17^\circ$, indicating a completely amorphous structure (Figure 2). The WAXS diffractogram of talc is characterized by the presence of three diffraction peaks in the range 2θ 1–30, at $2\theta = 9.5, 19.1$ and 28.7° [30]. Crystalline structure of the polymer matrix is significantly affected by the presence of talc: the composites containing talc show the presence of the three talc peaks and a new peak at 16.6° due to the crystalline phase of the PLA (inset Figure 2) [31]. Thus, as expected talc enhances PLA crystallization, a detailed analysis of the effect of talc on PLA was previously reported by our group [8], in the case of samples

Table 4. d_{001} interlayer distance for clay and nanocomposites

Sample name	Interlayer distance [nm]	
	Clay	Nanocomposite
PLA2.5C120A	2.5±0.05	3.5±0.05
PLA5C120A	2.5±0.05	3.5±0.05
PLA2.5C130B	1.7±0.05	3.6±0.05
PLA5C130B	1.7±0.05	3.6±0.05

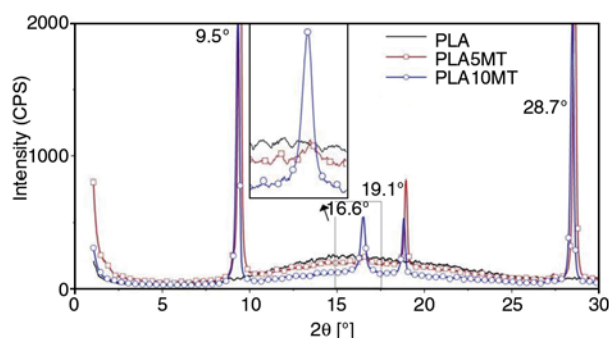


Figure 2. X-ray diffraction of melt-blended samples (inset: magnification of PLA characteristic peak)

prepared with similar cooling rate ($10^\circ\text{C min}^{-1}$) the crystalline content seems to be proportional to talc content even if taking into account the thickness of the sample (1 mm) and the inaccurate cooling-method (the water cooling of hydraulic press) these measures should be considered only qualitatively and with low precision.

PLA based nanocomposites were further analysed by means of TEM (Figure 3). The incorporation of C120A in the PLA matrix (Figure 3a–3d) shows certain level of intercalation as well as the occurrence of exfoliated silicate layers. When correlating these observations with X-ray diffraction (XRD) results, we can conclude that the C120A forms partially exfoliated nanocomposites. PLA nanocomposites based on C130B show a high level of intercalation and exfoliation of the silicate layers (Figure 3e–3h), as small stacks of swollen clay layers and single dispersed layers can be observed in the TEM micrograph, results that are in accordance with WAXS analyses.

In the case of talc-PLA composites taking into account the expected formation of micrometric composites SEM analyses was preferentially performed (Figure 4a). In the two composites (PLA5T and PLA10T) talc particles show a good dispersion at micrometric level (Figure 4).

From WAXS and TEM results, it is clear that the dispersion and interaction of the C130B in PLA is better than that obtained with C120A.

From Table 1, XRD and TEM data the following conclusions can be achieved: the dispersion of C130B is higher than the dispersion of C120A in the different nanocomposites thus the total interfacial area polymer/nanofiller is higher for the nanocomposites containing C130B than for the nanocomposites containing C120A. Taking into account the thickness of few nanometres for the C120A and C130B platelets

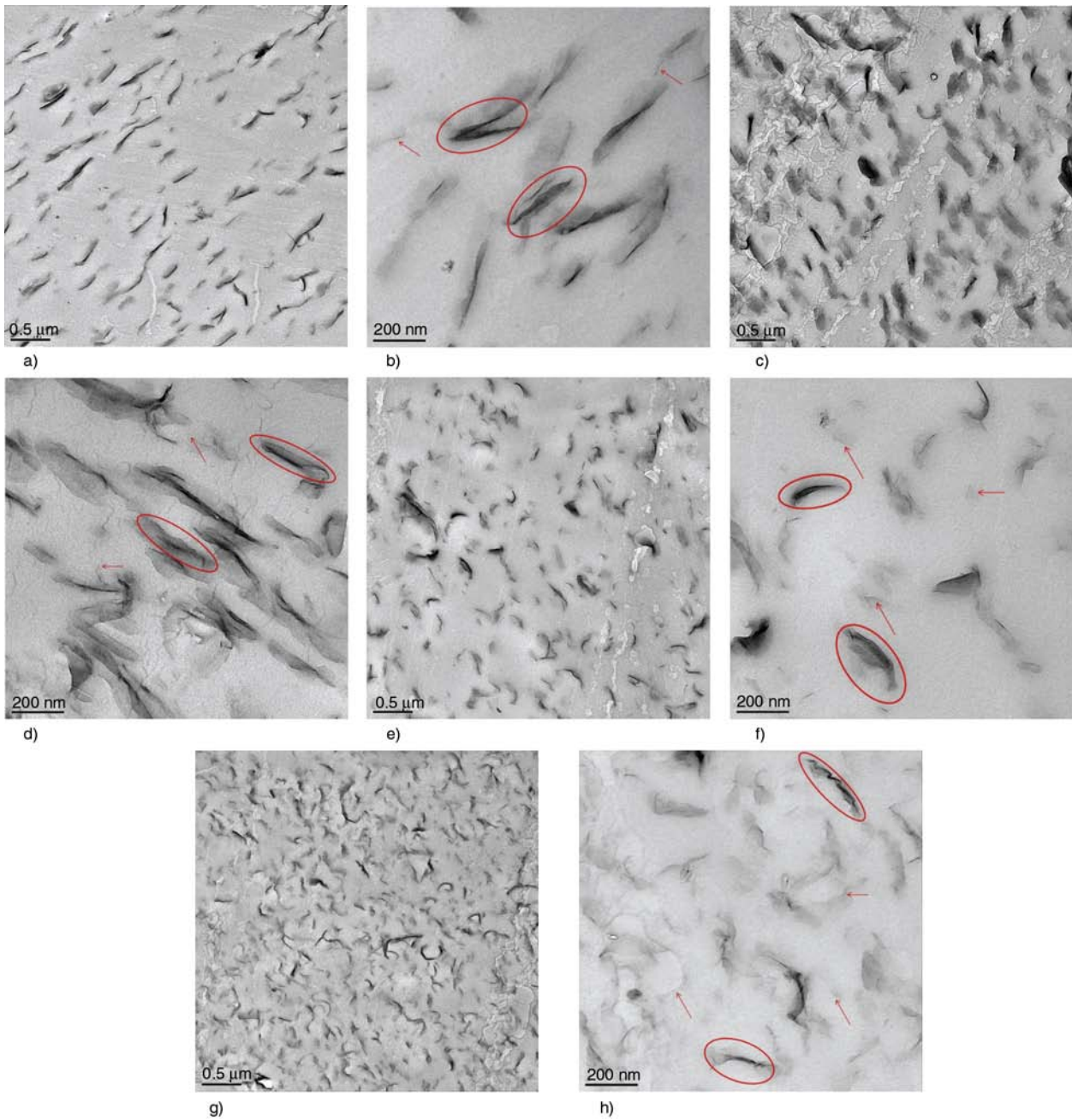


Figure 3. TEM micrographs of nanocomposites, example of exfoliated lamellae are indicated by arrows, example of intercalated lamellae are encircled a), b) PLA2.5CI20A, c), d) PLA5CI20A e), f) PLA2.5CI30B, g), h) PLA5CI30B

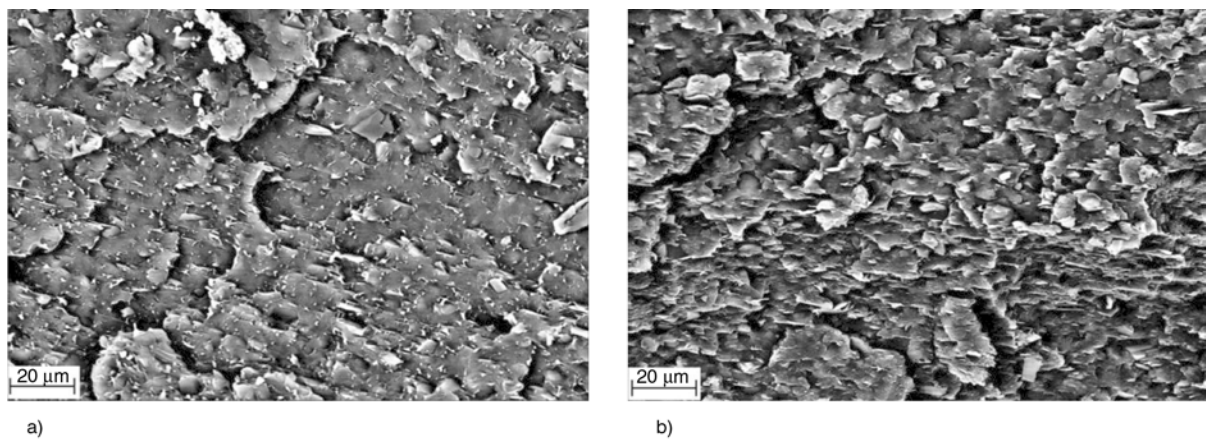


Figure 4. Scanning electron micrographs on cryogenic fractured, gold coated surfaces for (a) PLA5T (b) PLA10T

and the thickness of talc lamellar, of 2–3 orders of magnitude higher, the interfacial areas of C120A and C130B nanocomposites are of some order of magnitude higher respect to PLA/Talc microcomposites.

3.2. UV-vis characterization

Figure 5a shows the UV-vis spectra of pure PLA and nanocomposites. For PLA there is a saturation of the spectra below about 230 nm due to the absorbance of PLA ester groups whereas the nanocomposites show also an absorbance between 230–300 nm that is assigned to a O^{2-} octahedral Fe^{3+} charge transfer in the montmorillonite structure [32] and was reported for other montmorillonite-based nanocomposites such as polyvinylalcohol sodium montmorillonite nanocomposites [33, 34]. The PLA-talc composites (Figure 5b) do not have absorption bands specific for talc in the UV-vis region however in the whole visible region the light-scattering by the filler particles, proportional to the talc concentration, was found as expected for composite containing micrometric-size filler. The absorbances in the UV-vis region over 300 nm are quite low and similar for all the samples. Discrepancies in the temperature of samples caused by different absorbance during the photooxidation test can be thus excluded.

3.3. Infrared characterization

The peak assignments for neat PLA and the different nanocomposites are shown in Table 5. These assignments are based on values provided in the literature [35].

The IR spectrum of the different nanocomposites (Figure 6) corresponds to those expected from melt blending of the nanofillers with PLA. The main absorbance bands of nanofillers are covered by the saturation of the PLA bands, for the sake of brevity

Table 5. Band Assignments of PLA [cm^{-1}] [35]

Assignment	Assignment	Assignment	Assignment
$\nu_{as}CH_3$	2997	$\delta CH + \nu COC$	1265
$\nu_s CH_3$	2945	$\nu_{as}COC$ $r_{as}CH_3$	1209–1186
νCH	2881	$r_{as}CH_3$	1132
νCO	1759	ν_sCOC	1090
$\delta_{as}CH_3$	1454	ν_sC-CH_3	1046
δ_sCH_3	1348–1384	$rCH_3 + \nu CC$	960–925
$\delta_1CH + \delta_sCH_3$	1368–1360	$\nu C-COO$	870
δ_2CH	1315–1300	δCO	756

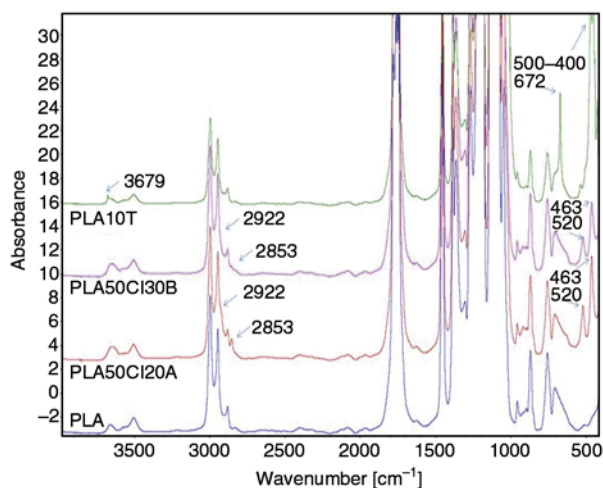


Figure 6. FTIR spectrum of PLA, PLA5C120A, PLA5C130B and PLA10T

only the spectra of PLA composites with the higher filler concentration are shown, the other samples show the same bands with lower intensity.

In PLA5C120A and PLA5C130B the bands that are readily recognizable are 520 and 463 cm^{-1} that are due to absorbance of the inorganic moieties [36], at the same time it is possible to recognize the $\nu_{as}CH_2$ and ν_sCH_2 of the organic modifiers respectively at 2924 and 2854 cm^{-1} . In the case of PLA10T the main differences are due to the sharp νOH of talc at 3679 cm^{-1} and the libration modes of the MgOH terminal groups at about 672 cm^{-1} and between 500 and 400 cm^{-1} [37]. Both for PLA and PLA micro/

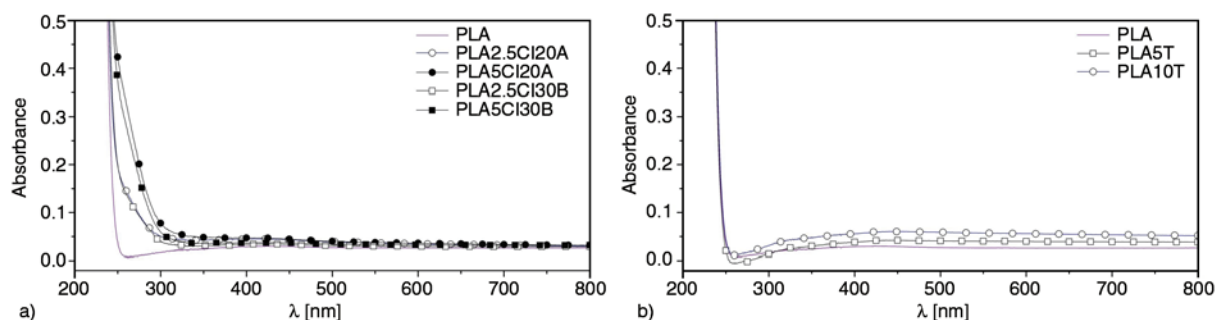


Figure 5. UV spectra a) PLA nanocomposites, b) PLA-talc composites

nanocomposites peaks that can be referred directly to crystal phase are completely absent [38] confirming that the film samples prepared by rapid cooling contains PLA in the amorphous phase.

3.4. Samples photo-oxidation

The reactions that occur to PLA during photooxidation were already discussed in previous articles [19, 20] and reported in Figure 1. Photooxidation usually begins by radicals formed from impurities by UV-irradiation or thermal decomposition. The reaction with higher probability is the abstraction of tertiary hydrogen from PLA chain with the formation of a tertiary radical $P\cdot$ (1). This radical can react with oxygen to form a peroxide radical (2), the reaction propagates by abstraction of another tertiary hydrogen with the formation of an hydroperoxide and the initial radical $P\cdot$ (3). The hydroperoxide could undergoes photolysis (4) with formation of $HO\cdot$ and a $PO\cdot$ radicals that can further evolve by β -scission (5). Taking into account the stability of the different fragments the most probable β -scission is the (5b) reaction that leads to the formation of an anhydride. The photolysis of the hydroperoxides is responsible for the branching character of polymer photooxidation processes. The results of this mechanism is the formation of a band with a maximum at 1847 cm^{-1} due to the asymmetric stretching of anhydride groups [39] and an absorption in the hydroxyl region (a broad band in the $4000\text{--}3000\text{ cm}^{-1}$) that corresponds to by-products of the photooxidation mechanism such as hydroperoxides and alcohols [17, 18]. These results were confirmed by photooxidation of PLA (Figure 7a).

The evolution of photooxidation by FTIR spectra of a nanocomposite (PLA5Cl30B Figure 7b) and a talc composite (PLA5T Figure 7c) vs time are shown. The addition of Cl30B does not change the infrared spectra modification; the appearance of the 1847 cm^{-1} absorption and of a broad band in the $4000\text{--}3000\text{ cm}^{-1}$ region. Similar behaviour was obtained for all nanocomposites. The oxidation rate increases with the nanofiller concentration and it is higher for Cl30B nanocomposites. In the case of PLA/talc microcomposites a similar spectra evolution was found but the increase of the two characteristic bands with time is less pronounced.

The increase of oxidation rate due to addition of nanoclays such as Cl20A or Cl30B was qualitatively attested in a previous article [19]. It was attrib-

uted to the transition metal impurities of clay. However no quantitative assessment of the effect of concentration on oxidation rate was performed. Taking into account the linearity between time and absorbance of the 1847 cm^{-1} peak, reported also from other groups such as Gardette *et al.* [20], in this work the oxidation rate was evaluated by linear regression of the normalized absorbance as a function of time (Figure 8, Table 6). From the obtained data it is evident that the oxidation rate of PLA increases linearly with fillers, such as talc, or nanofillers, such as Cl20A or Cl30B concentrations.

The main differences between the different micro/nanocomposites are: the presence of organic modifiers, the presence of iron in detectable amount for montmorillonite nanofillers (EDS in Table 1), the filler concentration and the different interfacial area.

As previously reported for nanocomposites containing Cl20A [19], the CH_2 stretching bands at 2922 and 2853 cm^{-1} of the nanocomposites containing Cl20A and Cl30B and assigned to the organic modifier completely disappear in the first hours of oxidation (Figure 9), evidencing that the organic modifiers are easily photodegraded in the beginning of photooxidation. Provided that no evidence of low photostability of alkyl chains in onium salts are reported in literature, the rapid decomposition of the organic modifier accounts for a photodegradation activity of montmorillonite surface, this effect is ascribed to a catalytic effect of montmorillonite, possibly linked to the presence of transition metals in the clay structure. Because of this early disappearance, a chemical influence of organic modifiers in the photoodegradation mechanism could be excluded except eventually as a supplementary source of radicals (reaction (1) Figure 1) in the early stage.

The oxidation rate for PLA-clay nanocomposites is not comparable with the increase due to the pres-

Table 6. Oxidation rate (slope) obtained from normalised absorption at 1847 cm^{-1} of PLA composites and nanocomposites

Sample	Slope $\cdot 10^{-6}$ [h^{-1}]
PLA	12.9 \pm 0.7
PLA5T	18.8 \pm 0.5
PLA10T	22.6 \pm 0.1
PLA2.5Cl20A	868.8 \pm 9.2
PLA5Cl20A	1800 \pm 29.3
PLA2.5Cl30B	1500 \pm 21.9
PLA5Cl30B	3140 \pm 31.5

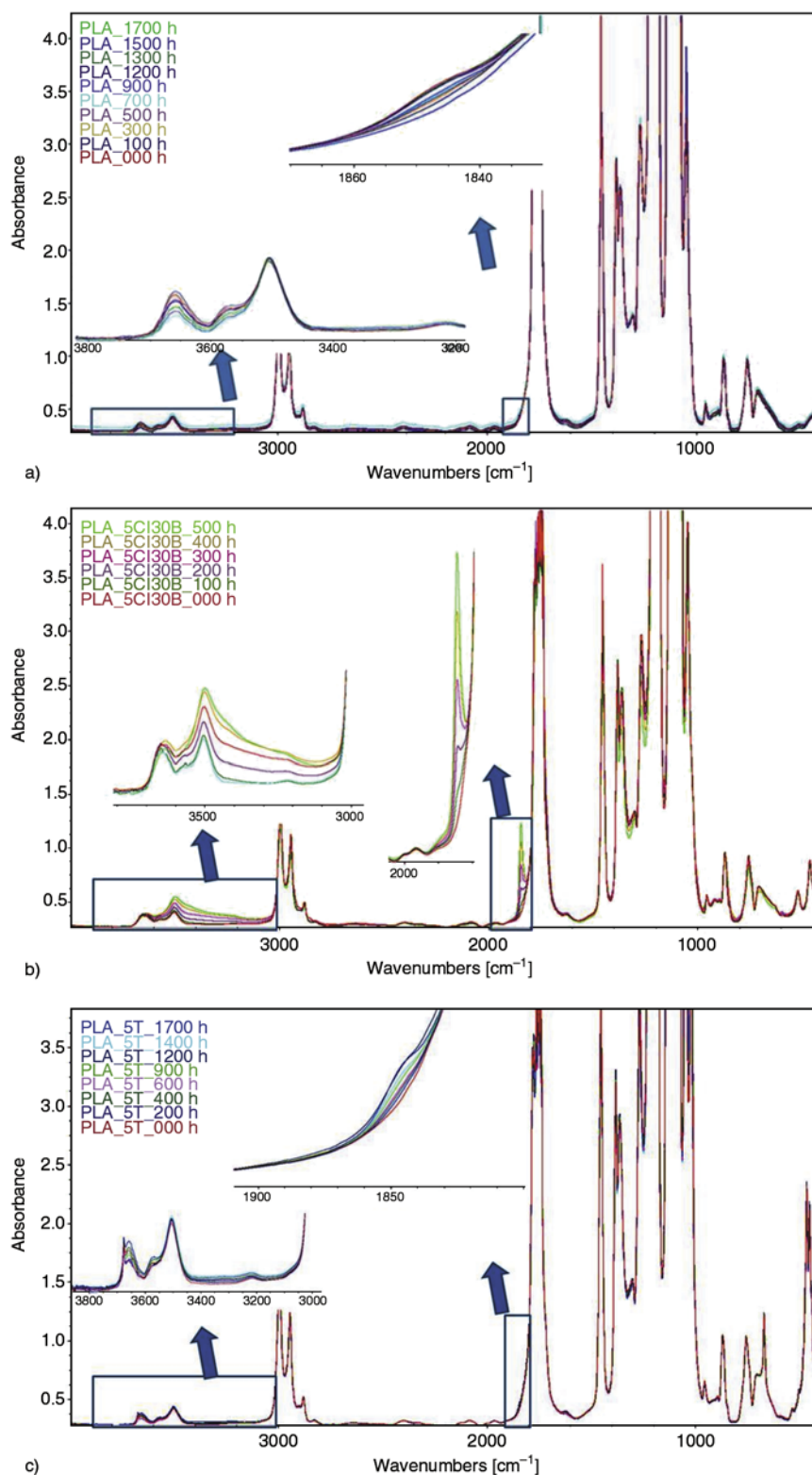


Figure 7. FTIR spectrum vs photooxidation time a) PLA, b) PLA5Cl30B, c) PLA5T

ence of talc. The oxidation rate for PLA-clay nanocomposites is two orders of magnitude higher (Table 6). The oxidation rate of PLA-clay nanocomposites depends on the type of organic modifier. The Cl30B nanocomposites, in which there is a better dispersion of the nanofiller, have higher oxi-

dation rates. The oxidation rate for both types of clay nanocomposites is directly proportional to clay concentration and thus, taking into account the similar concentration of iron for the two clays (Table 1), the increase of oxidation rate is linked to the increase of interfacial area. In fact interfacial area

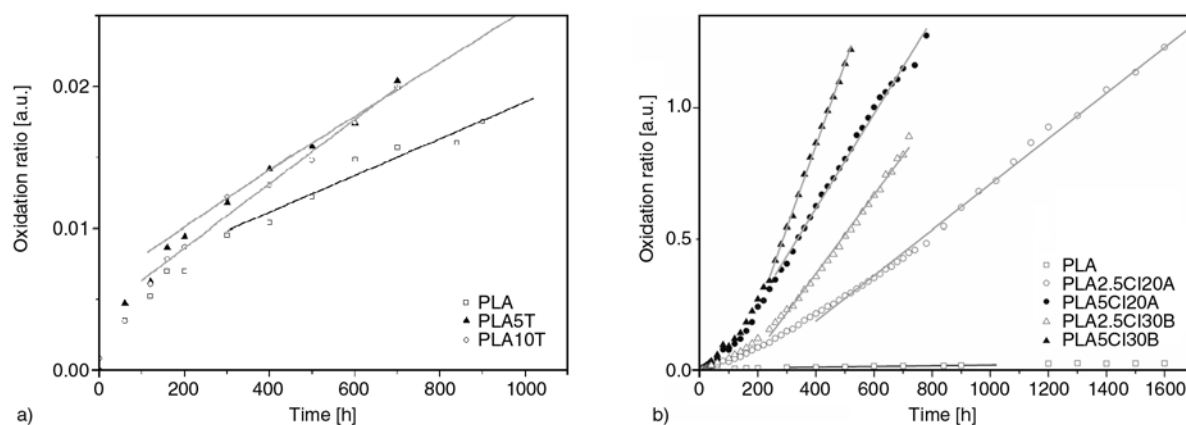


Figure 8. Evolution of 1847 cm^{-1} anhydride peak vs time a) talc composites b) clay nanocomposites

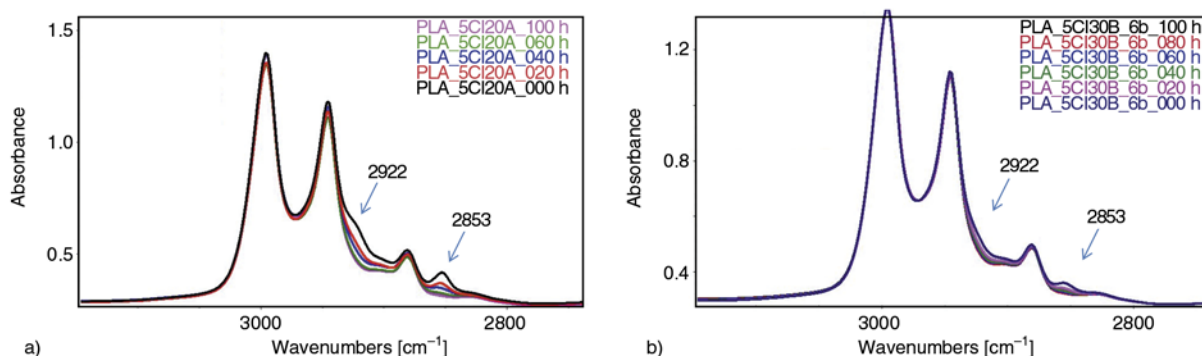


Figure 9. FTIR spectrum (νCH zone) vs photooxidation time a) PLA5Cl20A b) PLA5Cl30B

increases increasing dispersion degree (e.g. from Cl20A nanocomposites to Cl30B nanocomposites as demonstrated in the morphology part) and increasing filler concentration.

The main factor responsible for the increased oxidation rate is the peroxide decomposition in the presence of transition metal impurities. The catalytic effect of metallic compounds has been widely reported and is well-known [40]. Metal ions can cause an acceleration of the oxidation of polymers by various processes including the decomposition of hydroperoxides (Figure 10). The concentration of iron is responsible for the higher oxidation rate for nanocomposites. However a catalytic activity in the peroxide decomposition by Brønsted and Lewis acids groups previously described by Okamoto [41] can be also assumed and could be the responsible for the increase in oxidation rate for the talc micro-

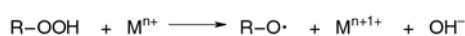


Figure 10. Photocatalytic decomposition of hydroperoxides by transition metal ions: transition metal ion catalyzes the hydroperoxide decomposition

composites. All these species can interact better with peroxide by the increase of interfacial area where the polymer is directly in contact with micro/nanofiller surface.

4. Conclusions

The absorbance at 1847 cm^{-1} is a linear function of irradiation time both for PLA/talc microcomposites and PLA/clay nanocomposites. The addition of filler increases the anhydride formation rate; this increase depends on the size/type of the filler and on iron concentration. Nanoparticles such as clays, with a high interfacial area and a high iron concentration, increase of two orders of magnitude the PLA photooxidation. This increase in the photooxidation rate also depends from the filler concentration and dispersion degree increasing thus with the surface of contact of PLA/nanoclay. On the other end a small effect of the acidic sites on the filler surface cannot be excluded.

Acknowledgements

The authors would thank Prof Giovanni Camino of Politecnico di Torino (Politecnico di Torino sede di Alessandria) for the feedback and useful comments.

References

- [1] Jana S. C., Jain S.: Dispersion of nanofillers in high performance polymers using reactive solvents as processing aids. *Polymer*, **42**, 6897–6905 (2001). DOI: [10.1016/S0032-3861\(01\)00175-6](https://doi.org/10.1016/S0032-3861(01)00175-6)
- [2] Solarski S., Mahjoubi F., Ferreira M., Devaux E., Bachelet P., Bourbigot S., Delobel R., Coszach P., Murariu M., Da Silva Ferreira A., Alexandre M., Degee P., Dubois P.: (Plasticized) polylactide/clay nanocomposite textile: Thermal, mechanical, shrinkage and fire properties. *Journal of Materials Science*, **42**, 5105–5117 (2007). DOI: [10.1007/s10853-006-0911-0](https://doi.org/10.1007/s10853-006-0911-0)
- [3] Paul M. A., Alexandre M., Degée P., Henrist C., Rulmont A., Dubois P.: New nanocomposite materials based on plasticized poly(L-lactide) and organo-modified montmorillonites: Thermal and morphological study. *Polymer*, **44**, 443–450 (2003). DOI: [10.1016/S0032-3861\(02\)00778-4](https://doi.org/10.1016/S0032-3861(02)00778-4)
- [4] Chang J-H., An Y. U., Sur G. S.: Poly(lactic acid) nanocomposites with various organoclays. I. Thermomechanical properties, morphology, and gas permeability. *Journal of Polymer Science Part B: Polymer Physics*, **41**, 94–103 (2003). DOI: [10.1002/polb.10349](https://doi.org/10.1002/polb.10349)
- [5] Fukushima K., Tabuani D., Camino G.: Nanocomposites of PLA and PCL based on montmorillonite and sepiolite. *Materials Science and Engineering: C*, **29**, 1433–1441 (2009). DOI: [10.1016/j.msec.2008.11.005](https://doi.org/10.1016/j.msec.2008.11.005)
- [6] Ray S. S., Yamada K., Okamoto M., Ueda K.: Control of biodegradability of polylactide via nanocomposite technology. *Macromolecular Materials and Engineering*, **288**, 203–208 (2003). DOI: [10.1002/mame.200390013](https://doi.org/10.1002/mame.200390013)
- [7] Fukushima K., Tabuani D., Arena M., Gennari M., Camino G.: Effect of clay type and loading on thermal, mechanical properties and biodegradation of poly(lactic acid) nanocomposites. *Reactive and Functional Polymers*, **73**, 540–549 (2013). DOI: [10.1016/j.reactfunctpolym.2013.01.003](https://doi.org/10.1016/j.reactfunctpolym.2013.01.003)
- [8] Battagazzore D., Bocchini S., Frache A.: Crystallization kinetics of poly(lactic acid)-talc composites. *Express Polymer Letters*, **5**, 849–858 (2011). DOI: [10.3144/expresspolymlett.2011.84](https://doi.org/10.3144/expresspolymlett.2011.84)
- [9] Murariu M., Da Silva Ferreira A., Degée P., Alexandre M., Dubois P.: Polylactide compositions. Part 1: Effect of filler content and size on mechanical properties of PLA/calcium sulfate composites. *Polymer*, **48**, 2613–2618 (2007). DOI: [10.1016/j.polymer.2007.02.067](https://doi.org/10.1016/j.polymer.2007.02.067)
- [10] Sobkowicz M. J., Feaver J. L., Dorgan J. R.: Clean and green bioplastic composites: Comparison of calcium sulfate and carbon nanospheres in polylactide composites. *Clean*, **36**, 706–713 (2008). DOI: [10.1002/clen.200800076](https://doi.org/10.1002/clen.200800076)
- [11] Tidjani A., Wilkie C. A.: Photo-oxidation of polymeric-inorganic nanocomposites: Chemical, thermal stability and fire retardancy investigations. *Polymer Degradation and Stability*, **74**, 33–37 (2001). DOI: [10.1016/S0141-3910\(01\)00061-1](https://doi.org/10.1016/S0141-3910(01)00061-1)
- [12] Qin H., Zhao C., Zhang S., Chen G., Yang M.: Photo-oxidative degradation of polyethylene/montmorillonite nanocomposite. *Polymer Degradation and Stability*, **81**, 497–500 (2003). DOI: [10.1016/S0141-3910\(03\)00136-8](https://doi.org/10.1016/S0141-3910(03)00136-8)
- [13] Mailhot B., Morlat S., Gardette J-L., Boucard S., Duchet J., Gérard J-F.: Photodegradation of polypropylene nanocomposites. *Polymer Degradation and Stability*, **82**, 163–167 (2003). DOI: [10.1016/S0141-3910\(03\)00179-4](https://doi.org/10.1016/S0141-3910(03)00179-4)
- [14] Morlat S., Mailhot B., Gonzalez D., Gardette J-L.: Photo-oxidation of polypropylene/montmorillonite nanocomposites. 1. Influence of nanoclay and compatibilizing agent. *Chemistry of Materials*, **16**, 377–383 (2004). DOI: [10.1021/cm031079k](https://doi.org/10.1021/cm031079k)
- [15] Morlat-Thérias S., Mailhot B., Gonzalez D., Gardette J-L.: Photooxidation of polypropylene/montmorillonite nanocomposites. 2. Interactions with antioxidants. *Chemistry of Materials*, **17**, 1072–1078 (2005). DOI: [10.1021/cm040172i](https://doi.org/10.1021/cm040172i)
- [16] Morlat-Thérias S., Mailhot B., Gardette J-L., Da Silva C., Haidar B., Vidal A.: Photooxidation of ethylene-propylene-diene/montmorillonite nanocomposites. *Polymer Degradation and Stability* **90**, 78–85 (2005). DOI: [10.1016/j.polymdegradstab.2005.01.040](https://doi.org/10.1016/j.polymdegradstab.2005.01.040)
- [17] Bocchini S., Morlat-Thérias S., Gardette J-L., Camino G.: Influence of nanodispersed boehmite on polypropylene photooxidation. *Polymer Degradation and Stability*, **92**, 1847–1856 (2007). DOI: [10.1016/j.polymdegradstab.2007.07.002](https://doi.org/10.1016/j.polymdegradstab.2007.07.002)
- [18] Bocchini S., Morlat-Thérias S., Gardette J. L., Camino G.: Influence of nanodispersed hydrotalcite on polypropylene photooxidation. *European Polymer Journal*, **44**, 3473–3481 (2008). DOI: [10.1016/j.eurpolymj.2008.08.035](https://doi.org/10.1016/j.eurpolymj.2008.08.035)
- [19] Bocchini S., Fukushima K., Di Blasio A., Fina A., Frache A., Geobaldo F.: Polylactic acid and polylactic acid-based nanocomposite photooxidation. *Biomacromolecules*, **11**, 2919–2926 (2010). DOI: [10.1021/bm1006773](https://doi.org/10.1021/bm1006773)
- [20] Gardette M., Thérias S., Gardette J-L., Murariu M., Dubois P.: Photooxidation of polylactide/calcium sulfate composites. *Polymer Degradation and Stability*, **96**, 616–623 (2011). DOI: [10.1016/j.polymdegradstab.2010.12.023](https://doi.org/10.1016/j.polymdegradstab.2010.12.023)
- [21] Li H., Huneault M. A.: Effect of nucleation and plasticization on the crystallization of poly(lactic acid). *Polymer*, **48**, 6855–6866 (2007). DOI: [10.1016/j.polymer.2007.09.020](https://doi.org/10.1016/j.polymer.2007.09.020)

- [22] Leong Y. W., Abu Bakar M. B., Mohd Ishak Z. A., Ariffin A.: Characterization of talc/calcium carbonate filled polypropylene hybrid composites weathered in a natural environment. *Polymer Degradation and Stability*, **83**, 411–422 (2004).
DOI: [10.1016/j.polymdegradstab.2003.08.004](https://doi.org/10.1016/j.polymdegradstab.2003.08.004)
- [23] Rotzinger B.: Talc-filled PP: A new concept to maintain long term heat stability. *Polymer Degradation and Stability*, **91**, 2884–2887 (2006).
DOI: [10.1016/j.polymdegradstab.2006.09.008](https://doi.org/10.1016/j.polymdegradstab.2006.09.008)
- [24] Utracki L. A., Broughton B., González-Rojano N., de Carvalho L. H., Achete C. A.: Clays for polymeric nanocomposites. *Polymer Engineering and Science*, **51**, 559–572 (2011).
DOI: [10.1002/pen.21807](https://doi.org/10.1002/pen.21807)
- [25] Philippart J-L., Sinturel C., Gardette J-L.: Influence of light intensity on the photooxidation of polypropylene. *Polymer Degradation and Stability*, **58**, 261–268 (1997).
DOI: [10.1016/S0141-3910\(97\)00056-6](https://doi.org/10.1016/S0141-3910(97)00056-6)
- [26] Wei P., Bocchini S., Camino G.: Nanocomposites combustion peculiarities. A case history: Polylactide-clays. *European Polymer Journal*, in press (2013).
DOI: [10.1016/j.eurpolymj.2012.11.010](https://doi.org/10.1016/j.eurpolymj.2012.11.010)
- [27] Fukushima K., Murariu M., Camino G., Dubois P.: Effect of expanded graphite/layered-silicate clay on thermal, mechanical and fire retardant properties of poly(lactic acid). *Polymer Degradation and Stability*, **95**, 1063–1076 (2010).
DOI: [10.1016/j.polymdegradstab.2010.02.029](https://doi.org/10.1016/j.polymdegradstab.2010.02.029)
- [28] Fukushima K., Fina A., Geobaldo F., Venturello A., Camino G.: Properties of poly(lactic acid) nanocomposites based on montmorillonite, sepiolite and zirconium phosphonate. *Express Polymer Letters*, **6**, 914–926 (2012).
DOI: [10.3144/expresspolymlett.2012.97](https://doi.org/10.3144/expresspolymlett.2012.97)
- [29] Pluta M., Galeski A., Alexandre M., Paul M-A., Dubois P.: Polylactide/montmorillonite nanocomposites and microcomposites prepared by melt blending: Structure and some physical properties. *Journal of Applied Polymer Science*, **86**, 1497–1506 (2002).
DOI: [10.1002/app.11309](https://doi.org/10.1002/app.11309)
- [30] Rayner J. H., Brown G.: The crystal structure of talc. *Clays and Clay Minerals*, **21**, 103–114 (1973).
DOI: [10.1346/CCMN.1973.0210206](https://doi.org/10.1346/CCMN.1973.0210206)
- [31] Xiao H. W., Li P., Ren X., Jiang T., Yeh J-T.: Isothermal crystallization kinetics and crystal structure of poly(lactic acid): Effect of triphenyl phosphate and talc. *Journal of Applied Polymer Science*, **118**, 3558–3569 (2010).
DOI: [10.1002/app.32728](https://doi.org/10.1002/app.32728)
- [32] Karickhoff S. W., Baley G. W.: Optical absorption spectra of clay minerals. *Clays and Clay Minerals*, **21**, 59–70 (1973).
DOI: [10.1346/CCMN.1973.0210109](https://doi.org/10.1346/CCMN.1973.0210109)
- [33] Strawhecker K. E., Manias E.: Structure and properties of poly(vinyl alcohol)/Na⁺ montmorillonite nanocomposites. *Chemistry of Materials*, **12**, 2943–2949 (2000).
DOI: [10.1021/cm000506g](https://doi.org/10.1021/cm000506g)
- [34] Ray S. S., Okamoto M.: Polymer/layered silicate nanocomposites: A review from preparation to processing. *Progress in Polymer Science*, **28**, 1539–1641 (2003).
DOI: [10.1016/j.progpolymsci.2003.08.002](https://doi.org/10.1016/j.progpolymsci.2003.08.002)
- [35] Kister G., Cassanas G., Vert M.: Effects of morphology, conformation and configuration on the IR and Raman spectra of various poly(lactic acid)s. *Polymer*, **39**, 267–273 (1998).
DOI: [10.1016/S0032-3861\(97\)00229-2](https://doi.org/10.1016/S0032-3861(97)00229-2)
- [36] Vantelon D., Pelletier M., Michot L. J., Barres O., Thomas F.: Fe, Mg and Al distribution in the octahedral sheet of montmorillonites. An infrared study in the OH-bending region. *Clay Minerals*, **36**, 369–379 (2001).
- [37] Schroeder P. A.: Infrared spectroscopy in clay science. *CMS Workshop Lectures*, **11**, 181–206 (2002).
- [38] Krikorian V., Pochan D. J.: Crystallization behavior of poly(L-lactic acid) nanocomposites: Nucleation and growth probed by infrared spectroscopy. *Macromolecules*, **38**, 6520–6527 (2005).
DOI: [10.1021/ma050739z](https://doi.org/10.1021/ma050739z)
- [39] Mayo D. W.: Spectra of carbonyl compounds of all kinds (factors affecting carbonyl group frequencies). in ‘Course notes on the interpretation of infrared and raman spectra’ (eds.: Mayo D. W., Miller F. A., Hannah R. W.) Wiley, New York, 179–204 (2003).
- [40] Rånby B., Rabek J. F.: Photodegradation photo-oxidation and photostabilisation of polymers. Wiley, London (1975).
- [41] Okamoto K., Toshima K., Matsumura S.: Degradation of poly(lactic acid) into repolymerizable oligomer using montmorillonite K10 for chemical recycling. *Macromolecular Bioscience*, **5**, 813–820 (2005).
DOI: [10.1002/mabi.200500086](https://doi.org/10.1002/mabi.200500086)

Phase behavior, interaction and properties of acetic acid lignin-containing polyurethane films coupled with aminopropyltriethoxy silane

H. H. Wang^{a,b*}, J. Mou^a, Y. H. Ni^b, G. Q. Fei^a, C. L. Si^c, J. Zou^a

^aKey laboratory of Auxiliary Chemistry & Technology for Chemical Industry, Ministry of Education. Shaanxi University of Science & Technology, 710021, Xi'an Shaanxi, China

^bLimerick Pulp and Paper Center, University of New Brunswick, E3B 5A3 Fredericton, NB, Canada

^cTianjin Key Laboratory of Pulp and Paper, Tianjin University of Science and Technology, 300457 Tianjin, China

Received 4 December 2012; accepted in revised form 2 February 2013

Abstract. A series of novel acetic acid lignin-containing polyurethane (LPU) films coupled with aminopropyltriethoxy silane (APTS) (LPUSi) or the mixture of APTS and trimethylol propane (TMP) (LPUSiT) were prepared. With 2% APTS addition, the crosslinking density increased, and the resultant films were endowed with good mechanical properties and water resistance. It was also found that the hydrogen bonding interaction between –NH and –C=O of urethane was destroyed, and new hydrogen bonds between APTS and LPU were formed. However, when APTS content was greater than 4%, significant phase aggregation were detected, resulting in poor mechanical properties and water resistance. In contrast, the crosslinking density, tensile strength and water resistance can be further improved with TMP addition at 2% APTS. The simultaneous addition of APTS and TMP was beneficial for phase mixing and the formation of uniform network. And the surface morphology of LPUSiT films became smoother and more homogeneous.

Keywords: polymer composites, acetic acid lignin, polyurethane, aminopropyltriethoxy silane, crosslinking

1. Introduction

The world plastics consumption has consistently grown for decades and was about 268 million tonnes in 2007 [1]. Production of polymers has long relied on fossil resources to provide raw materials. Usage of fossil oil is directly associated with environmental issue. In addition, the ever declining fossil reserves and increasing demand have caused the skyrocketing of the price of petroleum product [2]. Therefore biomass becomes a promising resource that can replace fossil oil for sustainable production of chemicals [3]. Lignin, as one of the most abundant aromatic biopolymers [4–5], constitutes about 15–30% of the wood and 12–20% of the annual plants [6]. Due to the renewable and biodegradable nature,

wide availability, non-agricultural based economy and reactivity, the utilization of lignin as a source of polymeric materials attracts more and more attention, albeit in different molecular weights and specific structures caused by the chemical processes associated with the production of cellulose pulp for papermaking [7].

Organosolv methods are recognized as viable sulfur-free alternatives to traditional pulping techniques. Oxoacid-based method has been demonstrated to be among the most successful method which allows efficient delignification of both woody [8–9] and non-woody materials [10]. Two oxoacids have achieved particularly good delignification result: formic acid [11–14], and acetic acid [10, 15]. Acetic

*Corresponding author, e-mail: wseafflower@126.com

acid acidolysis method is shown to be an efficient method to extract lignin with better yield and much lower content in impurities than for conventional acidolysis [16]. Pulp yields for the acetic acid treatment are also demonstrated to be higher than for formic acid [10]. In addition, conventional hydrolysis modifies the lignin polymer, causing the cleavage of some aryl-ether linkages. While acetic acid method is less damaging [16], the resulting partial acetylation of primary alcoholic groups has to be regarded as a non-negative point when considering further analytical characterization.

The use of lignin fragments as such, or after suitable chemical modifications, as macromonomers has been extensively investigated through the implication of both their phenolic and aliphatic hydroxyl groups to prepare polyurethanes [7]. A wide range of lignin-based polyurethane materials, such as rigid foams [17], hydrogels [18] and elastomers, have been synthesized and the corresponding mechanical and thermal properties have been evaluated. With respect to lignin-derived polyurethane plastics, most researches focused on Alcell lignin [19], kraft lignin [20]. Ciobanu *et al.* [21] prepared a series of flax soda lignin/polyurethane blends by solvent casting technique from dimethylformamide solutions. Better thermo-mechanical properties were found for the 4.2 wt% lignin-containing blend. Films containing more than 9.3 wt% lignin were heterogeneous. Ni *et al.* [19] synthesized Alcell lignin-based polyurethane with and without a polymerization catalyst. Hatakeyama *et al.* [22] obtained polyurethane from alcoholysis and kraft lignin-based polycaprolactones. Zhang and Huang [23] found that polyurethane-nitrolignin (NL) film with 2.8% nitrolignin which was prepared by tetrahydrofuran solution casting was most miscible, and its tensile strength was 2 times higher than that of PU films. A suitable content of NL plays an important role in the promotion of PU network formation, resulting in the enhancement of crosslinking density, whose contribution effectively enhances strength and hardness. Heretofore there are only few reports related to acetic acid lignin-containing polyurethane films, which have potential application in plastics [24–25]. Effects of acetic acid lignin content and annealing on mechanical and thermal properties were simply investigated, it was demonstrated PU containing

20% acetic acid lignin possesses better tensile strength. While at higher lignin content, the corresponding PU became hard and brittle.

Preparation of polyurethane films from lignin is not an easy process because of the structure of lignin, which on direct reaction with isocyanate gives brittle polyurethane [26]. In order to improve the lignin content in PU formulation for a product with suitable performance and extensive application, oxypropylation of lignin has been recognized as a promising method [20]. However, the high cost associated to the implementation of such chemical modification processes makes difficult to endow lignin with a high added value, delaying the industrial exploration of this renewable polymer [6]. In addition, linear polyols with high molecular weight are often incorporated into PU backbone to overcome the above shortcomings. For polyol with very high molecular weight, the efficiency decreases again as a result of increasing dilution factor of hydroxyl groups [4, 27]. Under such circumstances, how to make the network formation more efficient and increasing lignin content in PU become critical in increasing the mechanical properties of lignin-containing PU.

In our previous studies, a maximum acetic acid lignin (AL) content of 43.3% can be reached for the continuous polyurethane film formation [28]. The incorporation of trimethylol propane (TMP) and 3-aminopropyltriethoxysilane (APTS) is demonstrated to be beneficial to the thermal property of AL-containing polyurethane (LPU) films. Based on the information mentioned above, we used the acetic acid lignin on an ‘as received’ basis with no pretreatment or modification. The objective was to gain fundamental knowledge of chemistry and physics of the network formation of LPU films, and compare the properties of AL-containing polyurethanes coupled with APTS and TMP of different contents. To our best knowledge, APTS and TMP haven’t been simultaneously introduced into LPU system to improve the corresponding properties. In this study, effects of APTS content and TMP on the crosslinking density, morphology, hydrogen bonding, phase behavior, water resistance and mechanical properties of AL-containing polyurethane films were systematically investigated. These results can provide fundamental information for optimization of acetic acid lignin-containing polyurethane films.

2. Experimental section

2.1. Materials

Methylene diphenyl diisocyanate (MDI), polyethylene glycol (PEG, the number average molecular weight was 1000 g mol^{-1}), 3-aminopropyltriethoxysilane (APTS), trimethylolpropane (TMP) and N,N-dimethylacetamide (DMAc) were purchased from Aldrich Chemicals Co. Inc. (Canada). The above-mentioned materials were of analytical grade and were directly used without further purification. Acetic acid, HCl, dioxane and diethyl ether were also purchased from Aldrich Chemicals Co. Inc. (Canada).

2.2. Preparation and characterization of acetic acid lignin

Spruce wood chips were submitted to a treatment with 90% acetic-acid solutions (500 mL) catalyzed by small amount (0.6%) of HCl (8.3 g). Experiments were performed at boiling temperature using a liquor/wood ratio equal to 5 g/g for 3 h. Subsequently they were cooled to room temperature [28]. The spent liquor obtained by filtration was concentrated through rotary vacuum evaporator at 60°C , and approximately 100 mL concentrated sample was obtained, thereafter, 900 mL deionized water was added to precipitate the dissolved lignin. After 24 h, brown acetic acid lignin (AL) was obtained by filtration.

The lignin samples were acetylated before gel permeation chromatography (PL-GPC 50, England). The average number molecular weight (M_n) of AL was 3515 g mol^{-1} ; the average weight molecular weight was 6215 g mol^{-1} and the polydispersity index (PDI) was 1.768. Carboxylic, phenolic and aliphatic hydroxyl group contents were determined by non-aqueous potentiometric titration and ^1H NMR spectrometry (Bruker Advanced 400 MHz spectrometer, Germany) of the acetylated lignin [10]. The content of phenolic and aliphatic hydroxyl group was 4.96 and 4.57 wt%, respectively; and the content of carboxylic group was 5.76 wt%.

2.3. Preparation of AL-containing polyurethane

AL, TMP and PEG were dissolved in DMAc. MDI was added dropwise into the system. The mixture was kept stirring in a water bath at 60°C for 2 h. Then the temperature was increased to 70°C . After 1.5 h, different contents of APTS were added and

Table 1. Chemical composition of AL-containing polyurethanes

Sample	n(NCO)/n(OH)	Lignin [%] ^a	APTS [%] ^b	TMP [%] ^b
LPU	1.7:1	43.3	0	0
LPUSi1	1.7:1	43.3	1	0
LPUSi2	1.7:1	43.3	2	0
LPUSi3	1.7:1	43.3	4	0
LPUSi4	1.7:1	43.3	5	0
LPUSiT	1.7:1	43.3	2	1

^awith respect to PEG.

^bwith respect to total monomer mass.

the reaction was continued for another 0.5 h. The experimental conditions for preparing AL-containing polyurethane are given in Table 1. The experiment schemes and model of AL-containing polyurethane were illustrated in Figure 1 and 2, respectively.

2.4. Preparation of AL-containing polyurethane films

After the polymerization, the solution was immediately transferred to a polytetrafluoroethylene (PTFE) plate, which was allowed to dry at room temperature for 2 days and then at 100°C for 6 h. After demolding, the film was submitted to vacuum drying over phosphorous pentoxide for 5 days.

2.5. Swelling test

Samples of approximately $3 \text{ mm} \times 3 \text{ mm}$ were immersed in glass flasks containing dimethyl formamide (DMF) and allowed them to stand at ambient temperature. After 5 days equilibrium, samples were removed from DMF and patted with lint-free tissue paper to remove excess solvent, and the dimensions were measured again. The crosslink density [mol/cm^3] of the NCO–OH bonds for each specimen was estimated using Equation (1) which was proposed by Flory and Rehner [19, 29]:

$$\frac{\nu_c \left[\frac{\text{mol}}{\text{cm}^3} \right]}{V_0} = \frac{-2[\nu + \chi\nu^2 + \ln(1 - \nu)]}{V_1(2\nu^{1/3} - \nu)} \quad (1)$$

where ν_c is the effective number of moles of crosslinked chains, V_1 is molar volume of solvent, χ is the polymer-solvent interaction parameter, ν is the volume fraction of polymer in swollen gel ($\nu = V_0/V$), V_0 is volume of dry polymer, and V is volume of swollen gel at equilibrium.

In order to determine χ for our polyurethane-DMF system, swelling tests were carried out at 25, 30 and

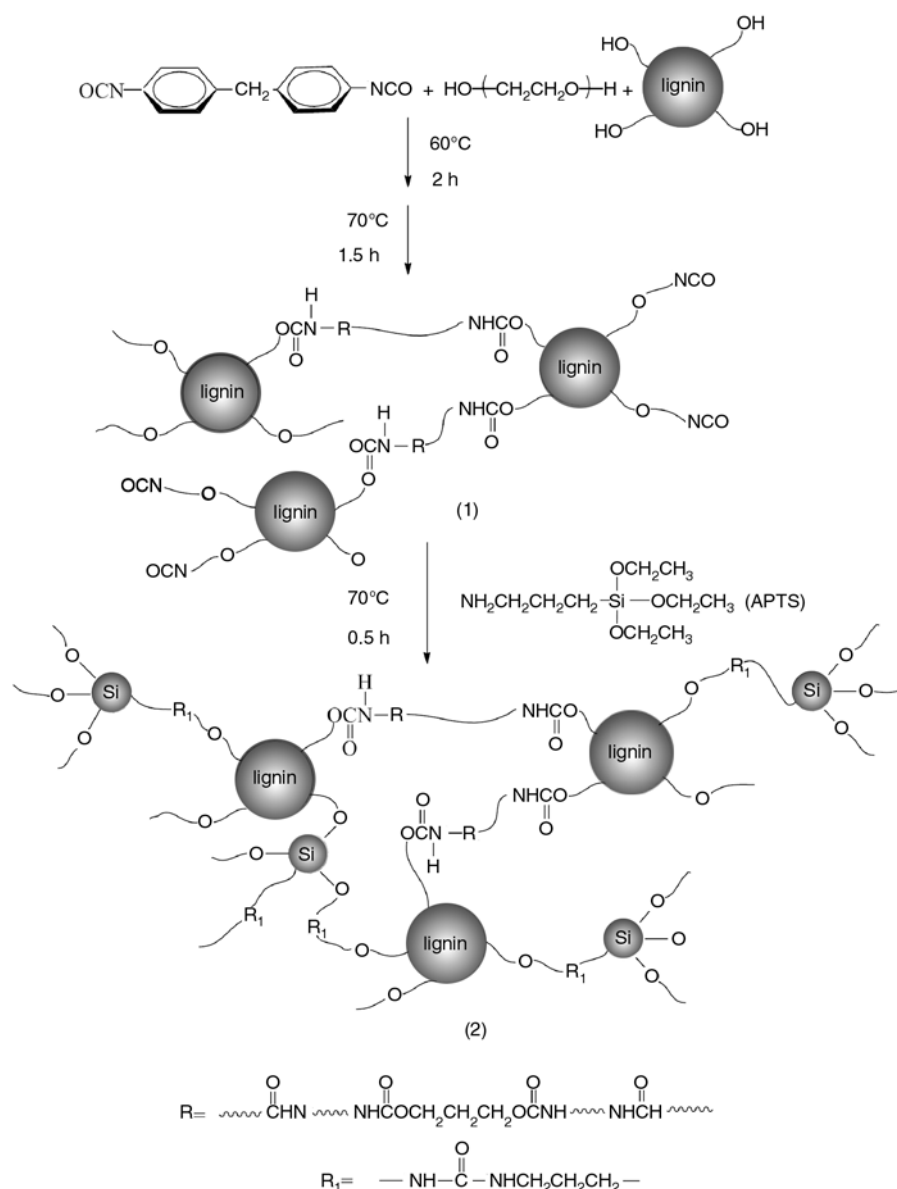


Figure 1. Experimental scheme and model for AL-containing polyurethane modified with APTS

35°C. From the temperature dependency of the swelling volume, χ value was obtained according to Equation (2). In the present study, the polymer-solvent interaction parameter (χ) was determined to be 0.49:

$$\frac{\delta \ln \nu}{\delta \ln T} = \frac{-3\chi(1-\nu)}{5(1-\chi)} \quad (2)$$

2.6. Characterization

Fourier transform infrared (FT-IR) spectra of all samples were recorded on an American Perkin-Elmer spectrum 100 FT-IR spectrometer in the range of 4000–500 cm^{-1} .

Dynamic mechanical analysis (DMA) was performed on an American TA DMA Q800 dynamic

mechanical analyzer with a clamp type of tension film. The heating rate was maintained at 3°C/min from –110 to 200°C. The strain and frequency were 0.04% and 1 Hz respectively.

The tensile strength (σ) was measured on a CMT6503 universal testing machine (Shenzhen SANS Test Machine Co. Ltd., Shenzhen, P.R. China) with a crosshead rate of 200 mm/min according to GB13022-91. An average of five replicates of each sample was taken.

Environmental scanning electron microscope (ESEM), coupled with an EDAX energy dispersive X-ray (EDX) system, was carried out on a Hitachi SU-70 SEM (Japan). The surface of polyurethane films was coated by carbon to remove the side effect of charge.

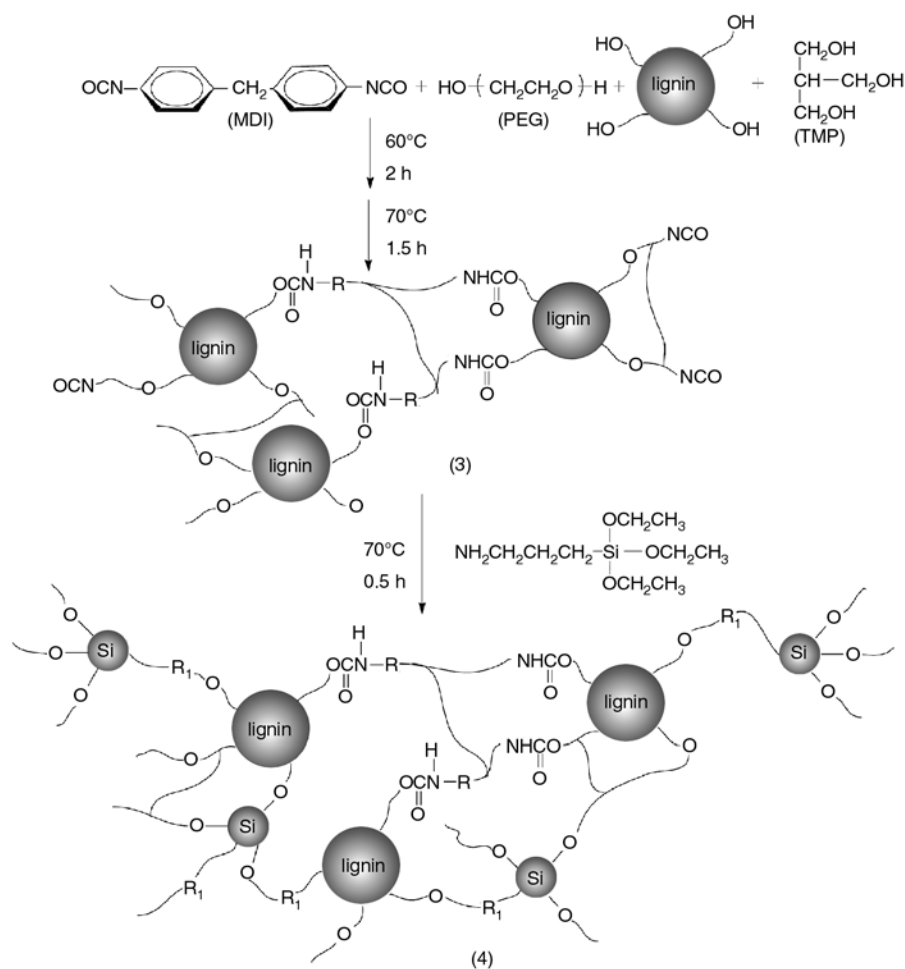


Figure 2. Experimental scheme and model for AL-containing polyurethane modified with APTS and TMP

Angular dependent X-ray photoelectron spectroscopy (XPS) was performed on a Perkin-Elmer physical Electronic Model 5400 (America) with a hemisphere analyzer and a position sensitive detector. The spectrometer was equipped with an Mg/K α (1253.6 eV) achromatic X-ray source operated at a power of 400 W and angles 45° were used with the X-ray source. Pass energy of 89.45 eV was chosen for all angle-dependent acquisitions. The spectrometer was typically run at the 6.7·10⁻⁷ Torr vacuum range. A wide scan (0–1000 eV) was recorded for each sample.

Contact angles were measured with a JJC-I contact angle goniometer (Chengde Tester factory, P.R. China) at 25°C with water as medium.

The AL-containing polyurethane films were cut into circular disks by using a sharp-edged stainless steel die with inner diameter of 20 mm. The samples were dried in vacuum oven for 24 h to determine their dry weight (W). Absorption of films was determined by immersing the films in a beaker of water for 24 h. After wiping off the surface water

with a piece of filter paper, its weight (W_1) was determined. The water absorption (WS) of the films was calculated by Equation (3):

$$WS = \frac{W_1 - W}{W} \cdot 100\% \quad (3)$$

3. Results and discussion

3.1. Crosslinking density and mechanical properties

The crosslinking density and tensile strength of LPU films modified with different APTS and TMP contents are shown in Table 2. It is reported that crosslinking density has important effects on mechanical property, thermal behavior and water resistance of lignin-containing polyurethane films [19, 23], all of which are important characteristic parameters for polymeric materials. The crosslinking density is determined from swelling tests in DMF as described previously. Since DMF is a very strong solvent for lignin, lignin that is not incorporated into the polymer network will be dissolved to

produce a dark colored solution [19]. In this study, the absence of a colored solution suggests that acetic acid lignin is an active ingredient in the polyurethane system. At a given lignin content, the crosslinking density increases from $3.10 \cdot 10^{-4}$ to $3.88 \cdot 10^{-3} \text{ mol cm}^{-3}$ when APTS content increases from 0 to 2%. As the APTS content increases, more reactive groups ($-\text{SiOH}$) are generated by the hydrolysis of trialkoxy groups in APTS, which are available to crosslink with isocyanate groups and hydroxyl groups, resulting in dramatic increase in the crosslinking density (as shown in Figure 1). The increased crosslinking density is generally responsible for increasing strength, therefore the tensile strength of corresponding films increases from 16.2 to 22.9 MPa.

Further increase in the APTS content from 2 to 5% does not strengthen, but even lead to inferior tensile strength. It is also found that the crosslinking density decreases from $3.88 \cdot 10^{-3}$ to $1.64 \cdot 10^{-3} \text{ mol cm}^{-3}$. This is probably due to over-crosslinking of LPU network and the lack of uniformity distribution of APTS in AL-containing polyurethane. APTS is likely to self-aggregate instead interact with AL-containing polyurethane chains at higher APTS content. This behavior is also confirmed by FT-IR and ESEM studies (as shown in Figure 3 and 4), and suggests a phase-separated morphology for LPUSi when the APTS content is greater than 4%. At given APTS content, the crosslinking density of LPUSiT increases from $3.88 \cdot 10^{-3}$ to $5.01 \cdot 10^{-3} \text{ mol cm}^{-3}$ with TMP addition, resulting in highest tensile strength of 25.6 MPa. This might be explained by the fact that the number of available sites for crosslinking in AL-containing polyurethane is insufficient when APTS content is 2%, only a partial network is established. The addition of TMP at the first step is beneficial for the formation of more uniform network, and more reactive groups are thereby participated in the crosslinking to make the network well formed, as shown in Figure 2. The attempt to increase the crosslinking density and tensile strength merely through increasing APTS content is infeasible, which might be attributed to self-aggregative characteristic of APTS. The above-mentioned information indicates that there is good synergistic effect between APTS and TMP.

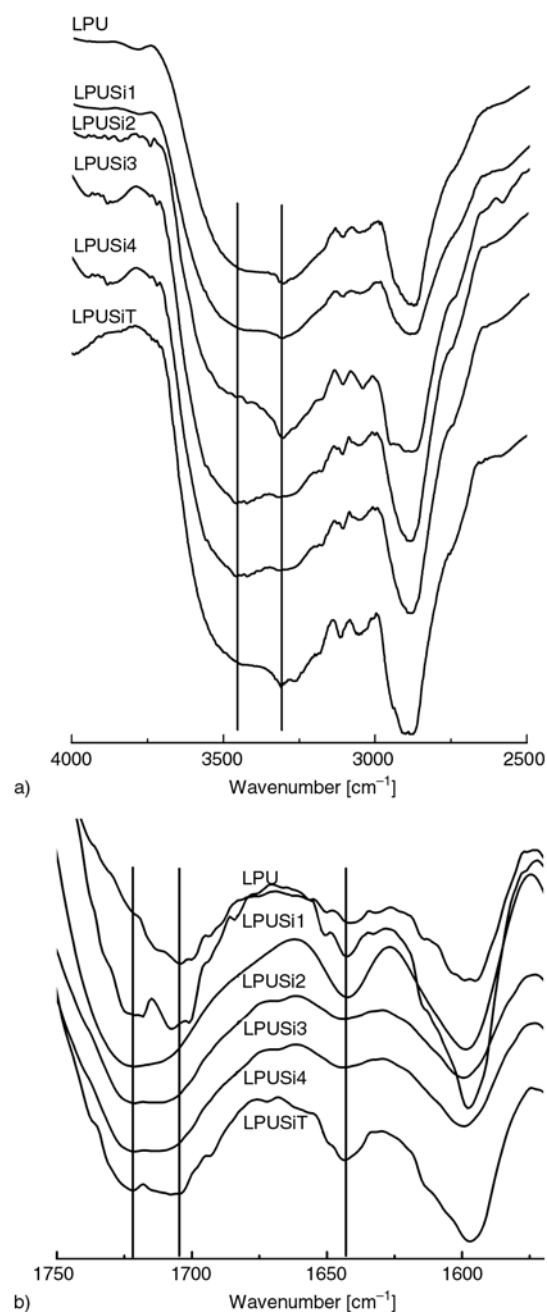


Figure 3. FT-IR spectra of LPU, LPUSi1, LPUSi2, LPUSi3, LPUSi4 and LPUSiT

3.2. Hydrogen-bonding interactions in LPU, LPUSi and LPUSiT films

The hydrogen bonding interactions in AL-containing polyurethane were investigated based on the FT-IR technique. It has been extensively reported by many researchers that FT-IR technique is an effective method to characterize the hydrogen bonding in polyurethane [30–31]. The FT-IR spectra of LPU,

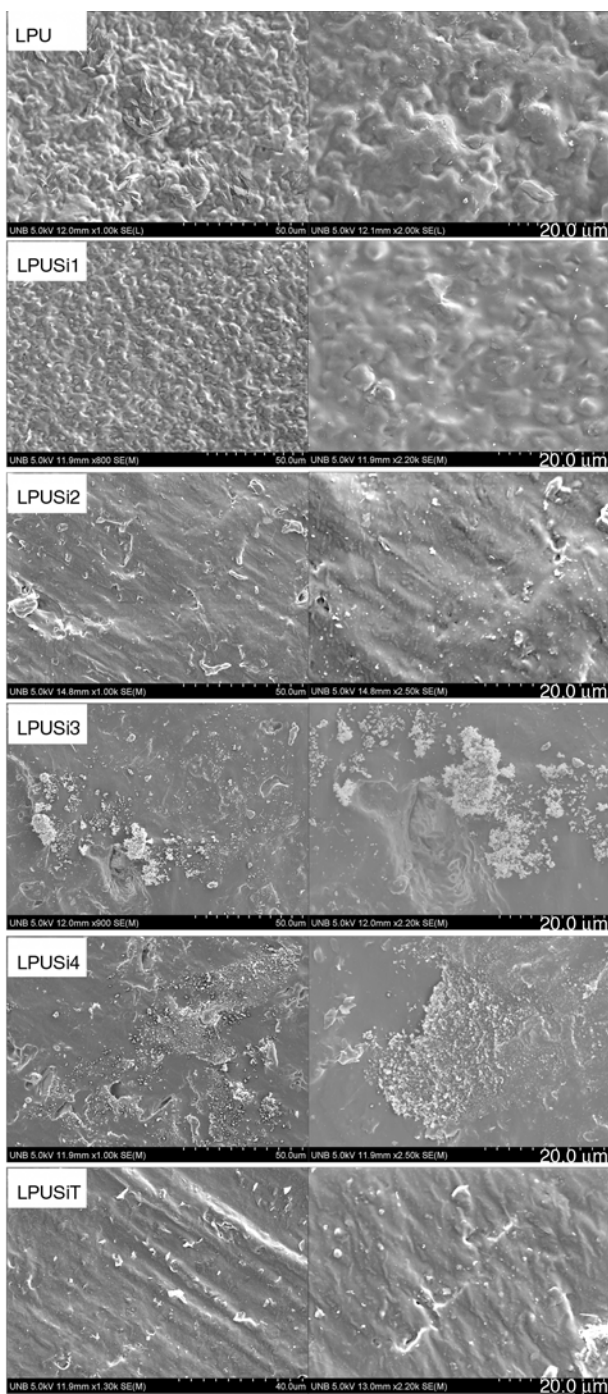


Figure 4. ESEM morphology of LPU, LPUSi and LPUSiT films at different magnification

LPUSi and LPUSiT are shown in Figure 3. The band at about $\sim 3310\text{ cm}^{-1}$ corresponds to stretching vibration of hydrogen-bonded -NH [32]. The band around $\sim 3446\text{ cm}^{-1}$ is assigned to free -NH [33–34]. The intensity of hydrogen-bonded -NH increases with increasing APTS addition from 0 to 2%. Intensity decay in free N-H band is apparent for LPUSi2, indicating that most of -NH groups are involved in the hydrogen bonding. As the APTS content is greater than 4%, the intensity of hydrogen-bonded

-NH decreases, while the intensity of free -NH increases.

The stretching bands at ~ 1721 , ~ 1709 and $\sim 1642\text{ cm}^{-1}$ are attributed to the absorption of free -C=O in urethane, hydrogen-bonded -C=O in urethane and hydrogen-bonded -C=O in urea, respectively [35–36]. The characteristic absorption of -C=O in urea at 1642 cm^{-1} becomes more pronounced with APTS addition, confirming the reactions between -NCO and APTS [36]. It can be also observed that the intensity increases with increasing APTS content from 1 to 2%, but decreases when APTS content is greater than 4%.

In contrast to hydrogen-bonded -C=O , the intensity of free -C=O is enhanced as to LPUSi1 and LPUSi2, whereas the intensity of hydrogen-bonded -NH increases. It indicates that APTS addition results in the damage of hydrogen bonds between -NH and -C=O that are existed in LPU, and new hydrogen bonds between APTS and LPU are formed. The increased intensity of hydrogen-bonded -NH might result from the hydrogen bonding between -NH and -Si-O-Si- (and/or -C=O in urea). For the LPUSi3 and LPUSi4 samples, the intensity of hydrogen-bonded -NH decreases, as well as the intensity of -C=O in urea. It suggests that the hydrogen bonds between APTS and LPU are damaged, due to the phase aggregation between LPU and APTS.

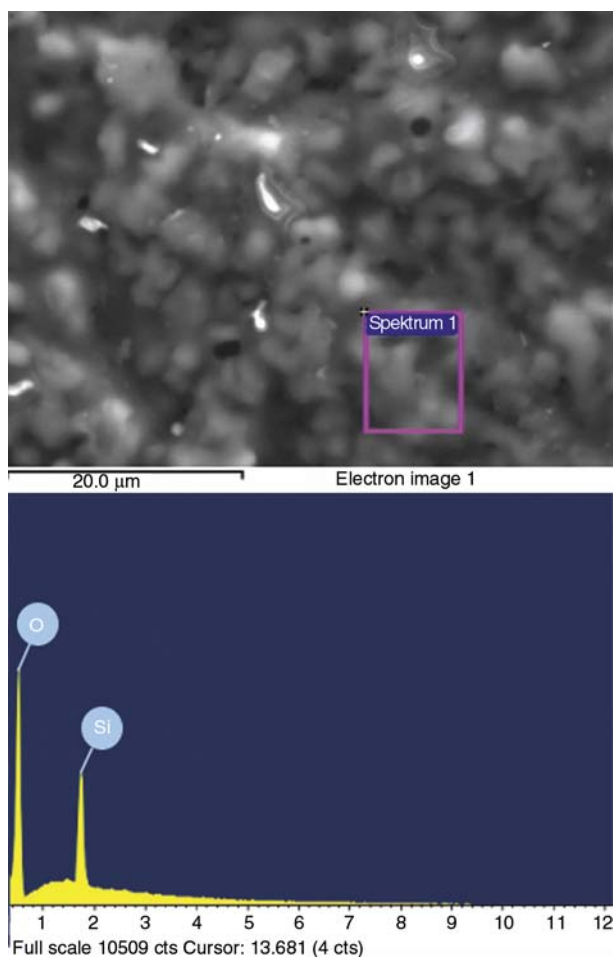
Furthermore, with simultaneous addition of APTS and TMP, the intensity of hydrogen-bonded -C=O and hydrogen-bonded -NH is further enhanced, so is the -C=O in urea. This indicates a more uniform network is formed. The results are in good agreement with those of strength and crosslinking density.

3.3. Morphology analysis

The morphology of polyurethane (PU) depends on the state of the compatibility and phase behavior between hard and soft segments [37]. The ESEM morphology of LPU, LPUSi and LPUSiT films is shown in Figure 4. As the APTS content increases from 0 to 2%, a transition is evident from rough surface of granular shape to a smooth and more homogeneous surface. It can be attributed to the increased crosslinking density (Table 2), and the more uniform network [38]. As the APTS content increases further to 5% (LPUSi3 and LPUSi4), the phase aggregation becomes more apparent, resulting in

Table 2. Effects of APTS and TMP content on crosslinking density and tensile strength

Sample	V_0	V	$v = V_0/V$	v_2	$v^{1/3}$	Crosslinking density [$\cdot 10^{-3} \text{ mol cm}^{-3}$]	Tensile strength [MPa]
LPU	21.949	73.359	0.29920	0.08952	0.66884	0.3102	16.2
LPUSi1	15.122	28.889	0.52346	0.27401	0.80593	1.9819	18.9
LPUSi2	24.179	38.770	0.62365	0.38894	0.85437	3.8818	22.9
LPUSi3	11.966	21.694	0.55159	0.30425	0.82011	2.4349	12.3
LPUSi4	23.194	46.671	0.49696	0.24697	0.79209	1.6426	–
LPUSiT	32.740	49.357	0.66333	0.44000	0.87212	5.0133	25.6

**Figure 5.** The energy-dispersive spectrum of LPUSi4

inhomogenous surface, as shown in Figure 4. It is found that more precipitated particles are generated on the surface of LPUSi3 and LPUSi4 films. In order to identify the components of the precipitated particles at the higher APTS addition, the EDX spectroscopy is conducted to observe the elemental composition of the precipitated particles, as shown in Figure 5. In addition, the chemical model for LPUSi3 and LPUSi4 are illustrated in Figure 6, respectively. As shown in Figure 5, the main components of the precipitated particles on the surface of LPUSi4 are Si and O elements. It has also been reported by Xia *et al.* that silica nanoparticles were

formed by hydrolysis of the silicon ethoxy groups in water and silanol polycondensation [39]. Therefore, it can be concluded that the precipitated particles on the surface of LPUSi4 are SiO_2 particles, which are generated by the hydrolysis of APTS. It also suggests the phase aggregation of excessive APTS on the surface of LPUSi3 and LPUSi4, which may be responsible for the decreased strength and water resistance.

With the addition of both APTS and TMP, the LPUSiT film again shows a smooth and homogeneous surface, which is again attributed to the increased crosslinking density and the formation of more uniform network. Increased crosslinking density indicates more hard domains with smaller inter-domain spacing, which tends to strengthen the elasticity of network and therefore results in enhancement in mechanical properties. On the other hand, the interaction between domains gets enhanced and phase separation behavior is weakened, therefore more homogeneous films can be obtained [36].

3.4. Dynamic mechanical analysis

The temperature dependence of storage modulus (G') and loss factor ($\tan \delta$) for LPU, LPUSi and LPUSiT films is shown in Figure 7. The storage moduli of the glassy state for LPU, LPUSi and LPUSiT films are in the order of $10^{3.5}$ MPa, typical for polymer glasses [40]. Highest storage modulus is detected for LPUSiT, since the increased crosslinking density is simultaneously responsible for the increase of rubbery modulus [41].

DMA is also a powerful technique to study initial motion of frozen polymer segments through α -relaxation at molecular-level. It is found that $T_{\alpha, \max}$ increases with the increase of APTS content from 0 to 2%. It suggests that the motion freedom of some chain segments is weakened. The addition of APTS restricts the motion of AL-containing polyurethane chains by virtue of entanglement and newly formed hydrogen bonds between APTS and urethane $-\text{NH}$,

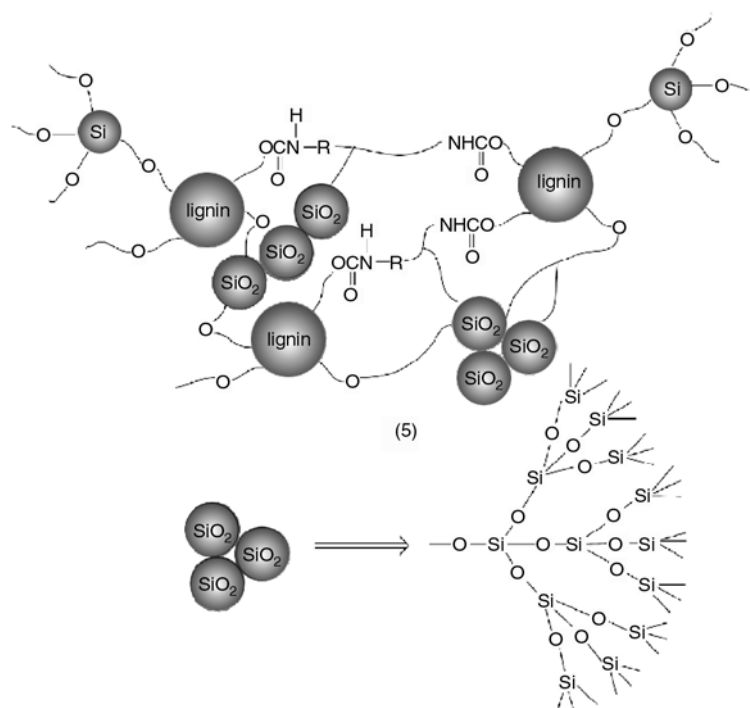


Figure 6. The chemical model for LPUSi3 and LPUSi4

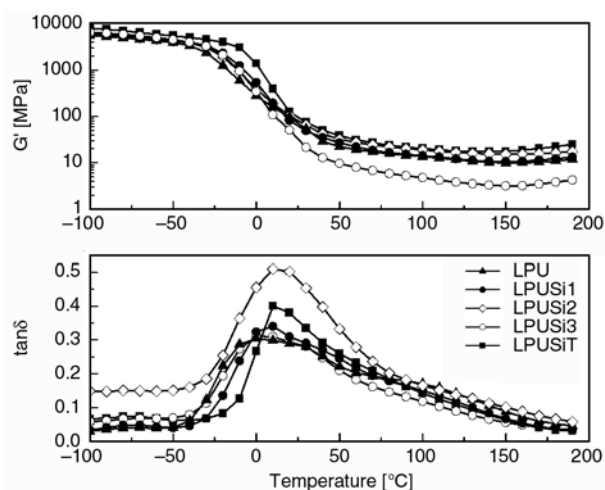


Figure 7. Temperature dependence of storage modulus and $\tan \delta$ for LPU, LPUSi and LPUSiT

also supported by the FT-IR results. The above tendency can also be explained by the increased crosslinking density. The higher the crosslinking density, the more restricted is the main chain motion and thus the higher is $T_{\alpha, \max}$ [41].

However, $T_{\alpha, \max}$ decreases with further increase in APTS content, suggesting that the mobility of soft segment is enhanced. Combined with the increased intensity of free $-\text{NH}$ and free $-\text{C}=\text{O}$ in FT-IR spectra, it can be concluded that hydrogen bonds between $-\text{NH}$ in hard segment and ether oxygen in soft segment are depressed.

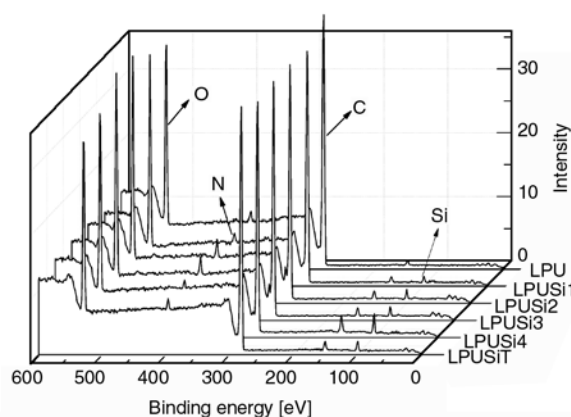
It is also found that the height of loss peak increases when APTS content increases from 0 to 2%, showing a tendency of changes similar to $T_{\alpha, \max}$. The loss-peak height represents the loss energy required by the motion of frozen segments [31]. It is consistent with the enhanced elongation and decreased Young's modulus, that is, higher toughness [42]. As a result, LPUSi2 and LPUSiT films are endowed with better toughness. However, the phase aggregation of APTS on the surface of films provided the higher motion freedom for soft segments in LPUSi3 and LPUSi4, resulting in lower $T_{\alpha, \max}$ and loss-peak height.

3.5. XPS analysis

XPS has been extensively utilized to study the surface functionalization and phase mixing for polyurethane materials [43–44]. The elemental compositions from the XPS survey spectra (Figure 8) and the peak area ratio from the de-convoluted spectra are presented in Table 3. The high resolution C1s XPS spectra of LPU, LPUSi and LPUSiT films are shown in Figure 9. The peaks at binding energies of 96–116, 280–305, 396–416, and 528–548 eV are ascribed to Si2p, C1s, N1s and O1s, respectively [45]. As the APTS content increases, the C–O/(C–C/C–H) ratio decreases from 0.919 to 0.510. It is reported that low surface energy soft segment resides towards the top surface and high surface

Table 3. Qualitative and quantitative XPS analysis for the surface of LPU, LPUSi and LPUSiT films

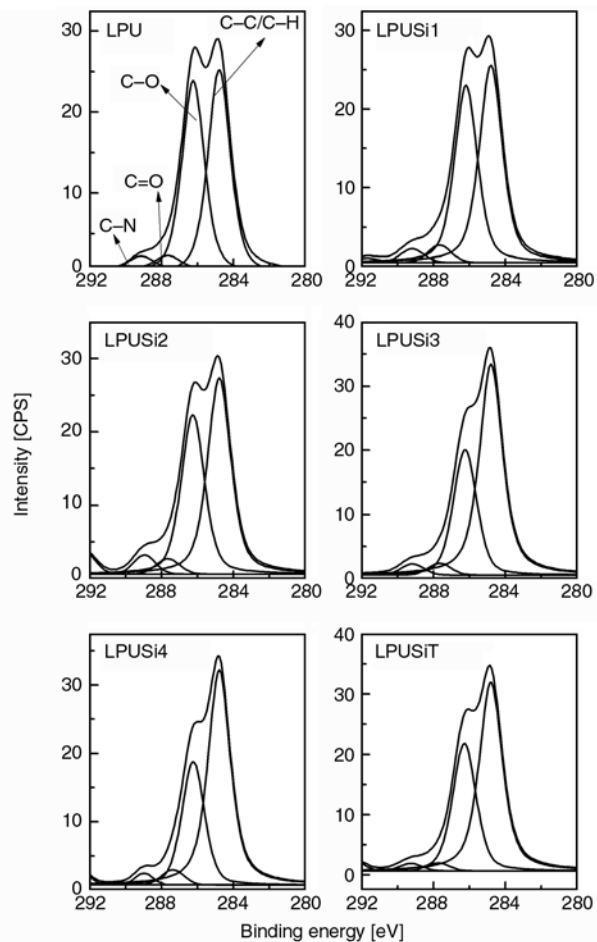
Sample	C-O/(C-C/C-H) (area ratio)	C=O/(C-C/C-H) (area ratio)	Si/C	N/C
LPU	0.919	0.0442	–	0.0179
LPUSi1	0.865	0.0585	0.0137	0.0293
LPUSi2	0.776	0.0760	0.0292	0.0339
LPUSi3	0.531	0.0404	0.0327	0.0179
LPUSi4	0.510	0.0343	0.0560	0.0148
LPUSiT	0.621	0.0292	0.0251	0.0156

**Figure 8.** XPS survey spectra of LPU, LPUSi and LPUSiT films

energy urethane/urea component resides inside the bulk of the polymer [44–45]. Therefore, it can be concluded that the addition of APTS promotes the phase mixing of polyurethane.

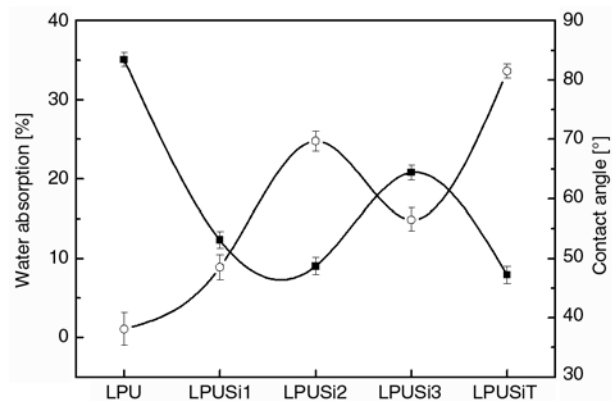
It can be also observed that the Si/C ratio increases with the increase of APTS content. At the same time, the highest C=O/(C-C/C-H) and N/C ratios are found for LPUSi2 sample. These results suggest the increased interactions between APTS and urethane on the surface of LPUSi2. However, the C=O/(C-C/C-H) and N/C ratios decrease with further increase in APTS content (LPUSi3 and LPUSi4). Increased Si/C ratio, together with lower C=O/(C-C/C-H) and N/C ratios, indicates weaker interactions between APTS and urethane and thus, enhanced phase aggregation.

Upon the addition of TMP at 2% APTS (LPUSi2 versus LPUSiT), it is worth noting that the C-O/(C-C/C-H), C=O/(C-C/C-H) and N/C ratios decrease, accompanied with the decrease in Si/C, all of which support the enhanced phase mixing with the simultaneous addition of APTS and TMP. It may be also postulated that the APTS surface aggregation may be decreased with TMP addition, as supported by the ESEM and FT-IR results.

**Figure 9.** High resolution C1s XPS spectra of LPU, LPUSi and LPUSiT films

3.6. Water resistance analysis

As shown in Figure 10, the water absorption decreases from 35.1 to 9.03% and contact angle increases from 38.1 to 69.7° when APTS content increases from 0 to 2%, and LPUSi2 with higher crosslinking density is endowed with lower water

**Figure 10.** Water absorption and contact angles for LPU, LPUSi and LPUSiT films

absorption and higher contact angle. It suggests that the increase in the crosslinking density is beneficial for the improvement of water resistance. However, the water absorption increases to 20.8% and the contact angle decreases to 56.5° as the APTS content increases to 5%, which can be due to the phase aggregation and decrease in crosslinking density. The addition of TMP (LPUSiT versus LPUSi2 samples) leads to the decrease of water absorption to 7.92% and increase of contact angle to 81.5° , which are explained by the increased crosslinking density and more homogeneous surface morphology together with enhanced phase mixing, as discussed in the previous sections.

4. Conclusions

Novel acetic acid lignin-containing polyurethane (LPU) films have been synthesized by a simple method without oxyalkylation of lignin. APTS and TMP were utilized instead to form three-dimensional bridge between MDI, PEG and acetic acid lignin. With 2% APTS addition, the crosslinking density increased from $3.10 \cdot 10^{-4}$ to $3.88 \cdot 10^{-3} \text{ mol cm}^{-3}$. The hydrogen bonds that were existed in LPU were damaged, and new hydrogen bonds between APTS and LPU were formed. In addition, smooth and homogenous surface morphology were obtained, which can be attributed to higher crosslinking density and phase mixing degree, the resultant films were endowed with good mechanical property and water resistance. However, further increase in APTS content was not effective to improve the film performance, and decreases in crosslinking density and phase aggregation were detected when APTS content were higher than 4%, resulting in performance attenuation. It was also worth to mention that the crosslinking density of LPUSiT increased from $3.88 \cdot 10^{-3}$ to $5.01 \cdot 10^{-3} \text{ mol cm}^{-3}$ with TMP addition at 2% APTS, resulting in enhanced tensile strength and water resistance. Further systematic study will be made on the synergistic effect of APTS and TMP on the properties of acetic acid-containing polyurethanes.

Acknowledgements

Funding for this project are from National Natural Science Foundation of China (21204046), NSERC CRD grant (CRDPJ 363811-07), the Canada Research Chairs program, the project sponsored by the Scientific Research Foundation for the Returned Overseas Chinese Scholars, State Education Ministry, Research Foundation of Education Bureau of Shaanxi Province (2010JK440, 2010JK433) and Academic Leaders Cultivation Program of Shaanxi University of Science & Technology (XSG2010014).

References

- [1] Shen L., Worrell E., Patel M.: Present and future development in plastics from biomass. *Biofuel, Bioproducts and Biorefining*, **4**, 25–40 (2010). DOI: [10.1002/bbb.189](https://doi.org/10.1002/bbb.189)
- [2] Naik S. N., Goud V. V., Rout P. K., Dalai A. K.: Production of first and second generation biofuels: A comprehensive review. *Renewable and Sustainable Energy Reviews*, **14**, 578–597 (2010). DOI: [10.1016/j.rser.2009.10.003](https://doi.org/10.1016/j.rser.2009.10.003)
- [3] Pan H.: Synthesis of polymers from organic solvent liquefied biomass: A review. *Renewable and Sustainable Energy Reviews*, **15**, 3454–3463 (2011). DOI: [10.1016/j.rser.2011.05.002](https://doi.org/10.1016/j.rser.2011.05.002)
- [4] Borges da Silva E. A., Zábokva M., Araújo J. D., Cateto C. A., Barreiro M. F., Belgacem M. N., Rodrigues A. E.: An integrated process to produce vanillin and lignin-based polyurethanes from *Kraft* lignin. *Chemical Engineering Research and Design*, **87**, 1276–1292 (2009). DOI: [10.1016/j.cherd.2009.05.008](https://doi.org/10.1016/j.cherd.2009.05.008)
- [5] Kubo S., Kadla J. F.: Poly(ethylene oxide)/organosolv lignin blends: Relationship between thermal properties, chemical structure, and blend behavior. *Macromolecules*, **37**, 6904–6911 (2004). DOI: [10.1021/ma0490552](https://doi.org/10.1021/ma0490552)
- [6] Cateto C. A., Barreiro M. F., Rodrigues A. E., Belgacem M. N.: Kinetic study of the formation of lignin-based polyurethanes in bulk. *Reactive and Functional Polymers*, **71**, 863–869 (2011). DOI: [10.1016/j.reactfunctpolym.2011.05.007](https://doi.org/10.1016/j.reactfunctpolym.2011.05.007)
- [7] Gandini A.: Polymers from renewable resources: A challenge for the future of macromolecular materials. *Macromolecules*, **41**, 9491–9504 (2008). DOI: [10.1021/ma801735u](https://doi.org/10.1021/ma801735u)
- [8] Abad S., Santos V., Parajó J. C.: Multistage organosolv pulping: A method for obtaining pulps with low hemicellulose contents. *Collection of Czechoslovak Chemical Communications*, **68**, 1163–1174 (2003). DOI: [10.1135/cccc20031163](https://doi.org/10.1135/cccc20031163)

- [9] Vila C., Santos V., Parajó J. C.: Dissolving pulp from TCF bleached Acetosolv beech pulp. *Journal of Chemical Technology and Biotechnology*, **79**, 1098–1104 (2004).
DOI: [10.1002/jctb.1090](https://doi.org/10.1002/jctb.1090)
- [10] Ligeró P., Villaverde J. J., de Vega A., Bao M.: Delignification of *Eucalyptus globulus* saplings in two organosolv systems (formic and acetic acid): Preliminary analysis of dissolved lignins. *Industrial Crops and Products*, **27**, 110–117 (2008).
DOI: [10.1016/j.indcrop.2007.08.008](https://doi.org/10.1016/j.indcrop.2007.08.008)
- [11] Jahan M. S., Chowdhury D. A. N., Islam M. K.: Atmospheric formic acid pulping and TCF bleaching of dhaincha (*Sesbania aculeata*), kash (*Saccharum spontaneum*) and banana stem (*Musa Cavendish*). *Industrial Crops and Products*, **26**, 324–331 (2007).
DOI: [10.1016/j.indcrop.2007.03.012](https://doi.org/10.1016/j.indcrop.2007.03.012)
- [12] Lam H. Q., Le Bigot Y., Delmas M., Avignon G.: Formic acid pulping of rice straw. *Industrial Crops and Products*, **14**, 65–71 (2001).
DOI: [10.1016/S0926-6690\(00\)00089-3](https://doi.org/10.1016/S0926-6690(00)00089-3)
- [13] Dapía S., Santos V., Parajó J. C.: Study of formic acid as an agent for biomass fractionation. *Biomass and Bioenergy*, **22**, 213–221 (2002).
DOI: [10.1016/S0961-9534\(01\)00073-3](https://doi.org/10.1016/S0961-9534(01)00073-3)
- [14] Caridad R., Ligeró P., Vega A., Bao M.: Formic acid delignification of *Miscanthus sinensis*. *Cellulose Chemistry and Technology*, **38**, 235–244 (2004).
- [15] Zhao X., Liu D.: Chemical and thermal characteristics of lignins isolated from Siam weed stem by acetic acid and formic acid delignification. *Industrial crops and Products*, **32**, 284–291 (2010).
DOI: [10.1016/j.indcrop.2010.05.003](https://doi.org/10.1016/j.indcrop.2010.05.003)
- [16] Lachenal D., Mortha G., Sevillano R-M., Zaroubine M.: Isolation of residual lignin from softwood kraft pulp. Advantages of the acetic acid acidolysis method. *Comptes Rendus Biologies*, **327**, 911–916 (2004).
DOI: [10.1016/j.crv.2004.09.002](https://doi.org/10.1016/j.crv.2004.09.002)
- [17] Cateto C. A., Barreiro M. F., Rodrigues A. E., Belgacem M. N.: Optimization study of lignin oxypropylation in view of the preparation of polyurethane rigid foams. *Industrial and Engineering Chemistry Research*, **48**, 2583–2589 (2009).
DOI: [10.1021/ie801251r](https://doi.org/10.1021/ie801251r)
- [18] Peng Z., Chen F.: Synthesis and properties of lignin-based polyurethane hydrogels. *International Journal of Polymeric Materials*, **60**, 674–683 (2011).
DOI: [10.1080/00914037.2010.551353](https://doi.org/10.1080/00914037.2010.551353)
- [19] Ni P., Thring R. W.: Synthesis of polyurethanes from solvolysis lignin using a polymerization catalyst: Mechanical and thermal properties. *International Journal of Polymeric Materials*, **52**, 685–707 (2003).
DOI: [10.1080/00914030304931](https://doi.org/10.1080/00914030304931)
- [20] Li Y., Ragauskas A. J.: Kraft lignin-based rigid polyurethane foam. *Journal of Wood Chemistry and Technology*, **32**, 210–224 (2012).
DOI: [10.1080/02773813.2011.652795](https://doi.org/10.1080/02773813.2011.652795)
- [21] Ciobanu C., Ungureanu M., Ignat L., Ungureanu D., Popa V. I.: Properties of lignin–polyurethane films prepared by casting method. *Industrial Crops and Products*, **20**, 231–241 (2004).
DOI: [10.1016/j.indcrop.2004.04.024](https://doi.org/10.1016/j.indcrop.2004.04.024)
- [22] Hatakeyama T., Izuta Y., Hirose S., Hatakeyama H.: Phase transitions of lignin-based polycaprolactones and their polyurethane derivatives. *Polymer*, **43**, 1177–1182 (2002).
DOI: [10.1016/S0032-3861\(01\)00714-5](https://doi.org/10.1016/S0032-3861(01)00714-5)
- [23] Zhang L., Huang J.: Effects of nitrolignin on mechanical properties of polyurethane–nitrolignin films. *Journal of Applied Polymer Science*, **80**, 1213–1219 (2001).
DOI: [10.1002/app.1206](https://doi.org/10.1002/app.1206)
- [24] Zhou B. A., Sha Z., Li Y., Feng Y.: Modified polyurethane with acetic acid lignin and its property. *China Pulp and Paper*, **28**, 22–25 (2009).
- [25] Yang W.: Aorigele: Effect of annealing on properties of lignin-based polyurethane films. in ‘16th International Symposium on Wood, Fiber and Pulping Chemistry- Proceedings, ISWFPC. Tianjin, China’, **2**, 1334–1337 (2011).
- [26] Sarkar S., Adhikari B.: Synthesis and characterization of lignin–HTPB copolyurethane. *European Polymer Journal*, **37**, 1391–1401 (2001).
DOI: [10.1016/S0014-3057\(00\)00264-0](https://doi.org/10.1016/S0014-3057(00)00264-0)
- [27] Thring R. W., Ni P., Aharoni S. M.: Molecular weight effects of the soft segment on the ultimate properties of lignin-derived polyurethanes. *International Journal of Polymeric Materials*, **53**, 507–524 (2004).
DOI: [10.1080/00914030490267627](https://doi.org/10.1080/00914030490267627)
- [28] Wang H., Ni Y., Jahan M. S., Liu Z., Schafer T.: Stability of cross-linked acetic acid lignin-containing polyurethane. *Journal of Thermal Analysis and Calorimetry*, **103**, 293–302 (2011).
DOI: [10.1007/s10973-010-1052-x](https://doi.org/10.1007/s10973-010-1052-x)
- [29] Flory P. J., Rehner J.: Statistical mechanics of cross-linked polymer networks II. Swelling. *The Journal of Chemical Physics*, **11**, 521–526 (1943).
DOI: [10.1063/1.1723792](https://doi.org/10.1063/1.1723792)
- [30] Huo S-P., Nie M-C., Kong Z-W., Wu G-M., Chen J.: Crosslinking kinetics of the formation of lignin-aminated polyol-based polyurethane foam. *Journal of Applied Polymer Science*, **125**, 152–157 (2012).
DOI: [10.1002/app.35401](https://doi.org/10.1002/app.35401)
- [31] Cui G., Fan H., Xia W., Ai F., Huang J.: Simultaneous enhancement in strength and elongation of waterborne polyurethane and role of star-like network with lignin core. *Journal of Applied Polymer Science*, **109**, 56–63 (2008).
DOI: [10.1002/app.28052](https://doi.org/10.1002/app.28052)
- [32] Luo N., Wang D-N., Ying S-K.: Hydrogen bonding between urethane and urea: Band assignment for the carbonyl region of FTi.r. spectrum. *Polymer*, **37**, 3045–3047 (1996).
DOI: [10.1016/0032-3861\(96\)89403-1](https://doi.org/10.1016/0032-3861(96)89403-1)

- [33] Srichatrapiumuk V. W., Cooper S. L.: Infrared thermal analysis of polyurethane block polymers. *Journal of Macromolecular Science Part B: Physics*, **15**, 267–311 (1978).
DOI: [10.1080/00222347808212599](https://doi.org/10.1080/00222347808212599)
- [34] Coleman M. M., Skrovanek D. J., Hu J., Painter P. C.: Hydrogen bonding in polymer blends. 1. FTIR studies of urethane-ether blends. *Macromolecules*, **21**, 59–65 (1988).
DOI: [10.1021/ma00179a014](https://doi.org/10.1021/ma00179a014)
- [35] Jiang X., Li J., Ding M., Tan H., Ling Q., Zhong Y., Fu Q.: Synthesis and degradation of nontoxic biodegradable waterborne polyurethanes elastomer with poly(ϵ -caprolactone) and poly(ethylene glycol) as soft segment. *European Polymer Journal*, **43**, 1838–1846 (2007).
DOI: [10.1016/j.eurpolymj.2007.02.029](https://doi.org/10.1016/j.eurpolymj.2007.02.029)
- [36] Yi H., Yan K-L.: Polyurethane modified with 3-aminopropyltriethoxysilane as wool antifelting agent. *Journal of Applied Polymer Science*, **109**, 2169–2175 (2008).
DOI: [10.1002/app.28012](https://doi.org/10.1002/app.28012)
- [37] Desai S., Thakore I. M., Sarawade B. D., Devi S.: Structure-property relationship in polyurethane elastomers containing starch as a crosslinker. *Polymer Engineering and Science*, **40**, 1200–1210 (2000).
DOI: [10.1002/pen.11247](https://doi.org/10.1002/pen.11247)
- [38] Bonini C., D’Auria M., Emanuele L., Ferri R., Pucciariello R., Sabia A. R.: Polyurethanes and polyesters from lignin. *Journal of Applied Polymer Science*, **98**, 1451–1456 (2005).
DOI: [10.1002/app.22277](https://doi.org/10.1002/app.22277)
- [39] Xia Y., Larock R. C.: Preparation and properties of aqueous castor oil-based polyurethane–silica nanocomposite dispersions through a sol–gel process. *Macromolecular Rapid Communication*, **32**, 1331–1337 (2011).
DOI: [10.1002/marc.201100203](https://doi.org/10.1002/marc.201100203)
- [40] Sormana J-L., Meredith J. C.: High-throughput discovery of structure–mechanical property relationships for segmented poly(urethane–urea)s. *Macromolecules*, **37**, 2186–2195 (2004).
DOI: [10.1021/ma035385v](https://doi.org/10.1021/ma035385v)
- [41] Noh S. H., Choi H. S., Noh S. T.: Synthesis and application of water-based urethane acrylate crosslinking agent containing unsaturated group. *Journal of Applied Polymer Science*, **78**, 1216–1223 (2000).
DOI: [10.1002/1097-4628\(20001107\)78:6<1216::AID-APP60>3.0.CO;2-8](https://doi.org/10.1002/1097-4628(20001107)78:6<1216::AID-APP60>3.0.CO;2-8)
- [42] Cui G., Xia W., Chen G., Wei M., Huang J.: Enhanced mechanical performances of waterborne polyurethane loaded with lignosulfonate and its supramolecular complexes. *Journal of Applied Polymer Science*, **106**, 4257–4263 (2007).
DOI: [10.1002/app.27077](https://doi.org/10.1002/app.27077)
- [43] Sanchis M. R., Calvo O., Fenollar O., Garcia D., Balart R.: Characterization of the surface changes and the aging effects of low-pressure nitrogen plasma treatment in a polyurethane film. *Polymer Testing*, **27**, 75–83 (2008).
DOI: [10.1016/j.polymertesting.2007.09.002](https://doi.org/10.1016/j.polymertesting.2007.09.002)
- [44] Chattopadhyay D. K., Sreedhar B., Raju K. V. S. N.: Effect of chain extender on phase mixing and coating properties of polyurethane ureas. *Industrial and Engineering Chemistry Research*, **44**, 1772–1779 (2005).
DOI: [10.1021/ie0492348](https://doi.org/10.1021/ie0492348)
- [45] Sreedhar B., Chattopadhyay D. K., Swapna V.: Thermal and surface characterization of polyurethane–urea clay nanocomposite coatings. *Journal of Applied Polymer Science*, **100**, 2393–2401 (2006).
DOI: [10.1002/app.23140](https://doi.org/10.1002/app.23140)

The effect of some disiloxane chain extenders on the thermal and mechanical properties of cross-linked poly(siloxane-urethane)s

E. Pusztai^{1*}, Cs. Kenyó², J. Nagy¹, Ö. Wagner¹

¹Budapest University of Technology and Economics, Department of Inorganic and Analytical Chemistry, H-1111 Budapest, Szent Gellért tér 4., Hungary

²Budapest University of Technology and Economics, Department of Physical Chemistry and Materials Science, H-1111 Budapest, Műgyetem rkp. 3., Hungary

Received 11 December 2012; accepted in revised form 2 February 2013

Abstract. Poly(siloxane-urethane) (PSiU) networks based on a bis(hydroxyorgano) disiloxane chain extender, a trifunctional polyether polyol as a cross-linker, methylene-diphenyl diisocyanate and α,ω -hydroxyethoxyethyl polydimethylsiloxane were synthesized in butyl acetate solution. The effect of the chain extenders and the cross-link density was investigated by using thermogravimetric analysis (TGA), dynamic mechanical thermal analysis (DMTA), swelling, hardness and tensile strength measurements. Isotherm thermogravimetric analyses were carried out for selected polymer compositions at 120 and 170°C and also the changes in tensile strength were followed. The different chain extenders have a strong effect on the hard segment structure, thus on the thermal and mechanical behaviour. The phase separation of the soft and hard segments was indicated by the two or three well distinguished $\tan\delta$ peaks, the maxima of which range within wide intervals depending on the polymer composition. The polymers of high cross-link density showed a very good thermal stability, high tensile strength (up to 68.7 MPa) and hardness (80–95 Shore A) even of high 13–36% dimethyl siloxane content. Changing the siloxane soft segment ratio and the cross-link density the physical properties can be adjusted.

Keywords: biocompatible polymers, poly(siloxane urethane) networks, thermal properties, mechanical properties, coatings

1. Introduction

Poly(siloxane-urethane) (PSiU) copolymers and networks have attracted a lot of researchers' attention for decades owing to the potential of blending the unique properties of polysiloxanes (PSi) and polyurethanes (PU). Combining the weather resistance, the biocompatibility (or hemocompatibility) and the thermal stability of PSis and the excellent mechanical properties of PUs makes PSiUs applicable as coating [1, 2], medical [3] or flame retardant [4] materials. PSiUs, first of all their mechanical properties, still have challenges for researchers.

PSiU and silicone-urea segmented copolymers were investigated by numerous research groups to understand the relationship between their structure and thermal or mechanical behaviour [5–10]. It was found that the polysiloxane chains are phase separated from the hard segments (HS), consisting of mostly 4,4'-methylene diphenylene diisocyanate (MDI) and 1,4-butanediol (BDO), and also from the polyether soft segments (SS). The two-phase structure was observable also by polarized light microscopy; and on transmission electron microscopy (TEM) images the phase-separated morphology did not seem to be dependent on the urethane structure

*Corresponding author, e-mail: pusztaierika@hotmail.com
© BME-PT

but on the used solvent [5]. Silicon based polyurethanes reflected the immiscibility of the inorganic/organic building blocks. There were several attempts to moderate the phase separation. With the optimal ratio of PSi [6] by using a comacrodilol [11] or different chain extenders [12, 13], the segment compatibility and in this way the mechanical and thermal properties could be improved. The cross-linked PSiUs also showed improved physical characteristics [2, 14, 15].

The thermal degradation of PSiU copolymers and networks was investigated in details in several papers [13, 16, 17]. The isothermal thermogravimetry is one of the best methods to investigate thermal stability [18]. The thermal degradation of PSiUs was studied by using thermogravimetric analysis (TGA) [2, 13, 14] sometimes coupled with a Fourier transform infrared spectroscopy (TG-FTIR) [16, 17], but the isothermal thermogravimetric analysis was usually not favoured [19]. In an earlier work thermal degradation of segmented PSiUs were observed to occur in two steps [13], later in the case of PSiU copolymers two basic steps and further sub-steps were revealed [17]; in some recent papers four steps were distinguished at various PSiU copolymers and networks [14, 16]. An improved thermal stability was obtained with poly(siloxane-urethane-imide) copolymers [16, 19].

The relationship between the structure and the mechanical properties of PSiUs was investigated extensively by using the dynamic mechanical thermal analysis (DMTA) [11, 12, 14, 15]. Depending on the composition of the polymers two or three glass transition temperatures (T_g) were observed according to $\tan\delta$, which indicates the phase separation. One T_g was observed from -128 to -90°C , which belongs to the glass transition of the siloxane soft segments, and T_g of the hard segments ranges between -15 and $+85^\circ\text{C}$ strongly depending on the structure of the HS. The cross-linked PSiUs showed definitely higher T_g -s, and different chain extenders had also very strong effect on the T_g of the HS [11, 12, 15].

The aim of our work was to synthesize new, cross-linked PSiUs by applying different bis(hydroxyalkyl) functional disiloxanes such as 1,3-bis(6-hydroxyhexanoylmethyl)-1,1,3,3-tetramethyl disiloxane (SIKOL, $M_w = 422$ g/mol), 1,3-bis(hydroxyethoxypropyl)-1,1,3,3-tetramethyl disiloxane (SIPA, $M_w = 338$ g/mol), 1,3-bis(2-hydroxypropanoyl-

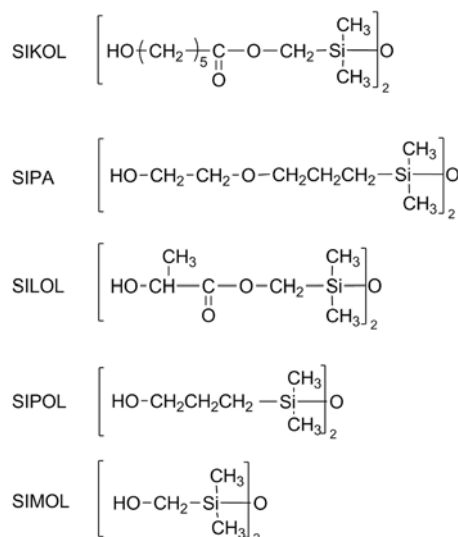


Figure 1. Molecular formula of the applied disiloxane chain extenders

methyl) tetramethyl disiloxane (SILOL, $M_w = 338$ g/mol), 1,3-bis(hydroxypropyl)-1,1,3,3-tetramethyl disiloxane (SIPOL, $M_w = 250$ g/mol), and 1,3-bis(hydroxymethyl)-1,1,3,3-tetramethyl disiloxane (SIMOL, $M_w = 194$ g/mol) as chain extenders (Figure 1), which showed good thermal stability and good mechanical properties. Synthesizing PSiUs of the possible highest tensile strength and of over 30% siloxane content was another objective of our work as previously ultimate tensile strength of only maximum 23 MPa was reported in siloxane-polyurethanes of high siloxane content [11, 12, 15], however, some applications require higher tensile strength (e.g. timing belts). We aimed to reveal the usability of the aforementioned disiloxanes in practice, thus we reacted them with a widely used diisocyanate monomer and used easily implementable techniques.

The tensile strength of all the samples was measured. Isothermal thermogravimetric analyses at 120 and 170°C for 230 hours were carried out on a set of samples of the best tensile strength which were synthesized by applying similar compositions. At the same time the changes in hardness and tensile strength were followed. TGA was carried out on the same set of the samples to investigate the effect of the chain extenders on thermal degradation, and also the effect of the PSi content was studied. More flexible polymers of high PSi content and moderate cross-link density were analysed by DMTA and by swelling measurements in THF. The average molecular weight between the cross-links (M_c) was determined by swelling measurements. The correlations

between M_{CS} , T_g s, PSi content, chain extenders and tensile strength were investigated.

2. Experimental section

2.1. Materials

1,4-butanediol (BDO) was purchased from Merck, Germany (>99%). Lupranol-1301 and Lupranol-1100 are products of BASF, Germany. Lupranol-1301 is a trifunctional polyether polyol with secondary OH groups ($M_w = 430$ g/mol); and Lupranol-1100 is a difunctional polypropylene glycol ($M_w = 1100$ g/mol). α,ω -hydroxyethoxyethyl polydimethylsiloxane (SLM-446060-15, $M_w = 700$ g/mol, henceforth abbreviated as SLM) was purchased from Wacker Chemie GmbH, Germany. All the aforementioned hydroxy functional compounds were dried under vacuum before use. A mixture of 2,4'- and 4,4'-methylene diphenyl diisocyanate (in 52:48 ratio, respectively, $M_w = 250$ g/mol), called Lupranat MI was obtained from BASF, Germany and it was used as received. Butyl acetate was purchased from Molar Chemicals Kft., Hungary (>99%), dried over molecular sieves and distilled before using. THF was purchased from Merck, Germany (>99%) and it was used as received. All disiloxane chain extenders were synthesized in our laboratory according to the methods published recently [20].

2.2. Polymer synthesis

PSiUs were synthesized in a two-step polymerization in butyl acetate solution without catalysts. Our

standard procedure is described below and the compositions are listed in Table 1. All the compounds except for the chain extenders were mixed in a round bottom flask under nitrogen and they were stirred for a couple of minutes at 115°C. As the mixture became viscous and the reaction started, butyl acetate was added to get a 25 w/w% diluted solution. After one hour reaction the chain extender was added to the solution and it was reacted for 10–15 minutes. Then the solutions were poured into flat sample holders and dried in normal ambient conditions at room temperature for one day. All the samples were annealed at 60°C for two hours and then at 120°C for 4 hours. Every sample was prepared in 5–10 g scale. The resulting sheets were 1 ± 0.1 mm thick except for the samples made for shock resistance (SR). 30 ± 5 μ m films were made on aluminum plates for SR. The plates were cleaned in iso-propyl alcohol before using, so the adhesion of the coatings was defect-free. The general scheme of the polymer structure is depicted in Figure 2.

2.3. Characterization methods and equipment

Mechanical testing was carried out on 4 mm dumbbell shaped test samples at room temperature by a Heckert ZMGi 250 machine (VEB Thüringer Industrialwerk, Ravenstein DDR, digitalized later on). A 1 kN load cell was used and the crosshead speed was 250 mm/min (MSZ 490-74 standard). The hardness of the samples was determined by a Bareiss HPE II-A – Shore A digital durometer hardness

Table 1. Composition (in mol) of the polymer samples made of the cross-linker (Lupranol-1301), the chain extenders (CE), the poly(dimethylsiloxane) (SLM), MDI, and weight percentage of the dimethyl siloxane content in the polymer composition

Sample name	Lupranol-1301 [mol]	CE [mol]	SLM [mol]	MDI [mol]	w/w% of [Me ₂ SiO] [%]	w/w% of disiloxane CE	w/w% of polysiloxane
PU	1.4	0	1.1*	3.3	0	0	0
PU-SIMOL	1	2	0	3.85	16.6	22	0
PU-SIPOL	1	2	0	3.85	15.6	26	0
PU-SIOL	1	2	0	3.85	14.3	33	0
PU-SIPA	1	2	0	3.85	13.1	33	0
PU-SIKOL	1	2	0	3.85	13.2	38	0
PU-BDO-SLM	0.2	2	0.9	3.6	24.6	0	39
PU-SIMOL-SLM	0.2	2	0.9	3.6	36.2	19	31
PU-SIPA-SLM	0.2	2	0.9	3.6	31.9	29	27
PU-SIKOL-SLM	0.2	2	0.9	3.6	29.8	34	26
PU-SIOL-SLM1	1	2	0.25	4.15	18.4	29	8
PU-SIOL-SLM2	1	2	1	5	26.6	22	23
PU-SIOL-SLM	0.2	2	0.9	3.6	31.9	29	27
PU-SIPOL-SLM1	1	2	0.25	4.15	19.9	23	8
PU-SIPOL-SLM2	1	2	1	5	28.3	17	24
PU-SIPOL-SLM	0.2	2	0.9	3.6	34.4	24	30

*instead of SLM, Lupranol-1100 was added

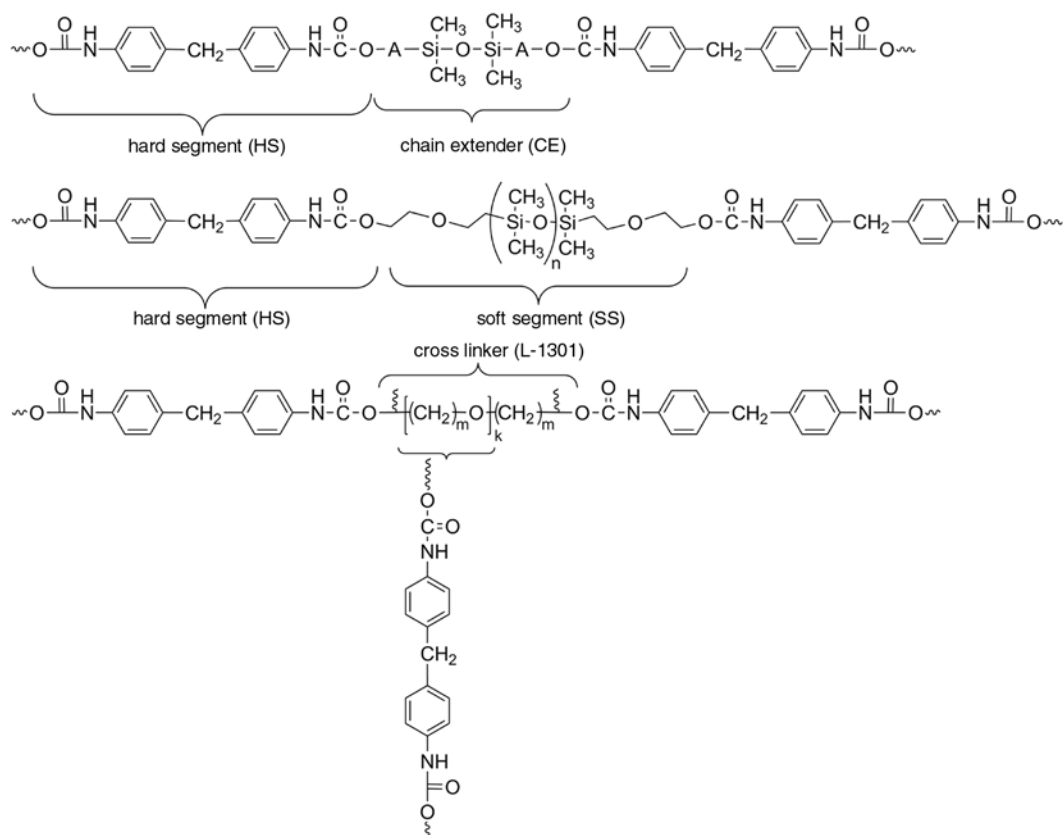


Figure 2. General schemes of the prepared PSiUs, A = $(\text{CH}_2)_5\text{-COO-CH}_2$, $(\text{CH}_2)_2\text{-O-(CH}_2)_3$, $\text{CH}(\text{CH}_3)\text{-COO-CH}_2$, C_3H_6 , CH_2

tester (Bareiss Prüfgeratebau GmbH, Oberdischingen, Germany) (DIN 53505 standard). The shock resistance was tested on aluminum plates with a 500g-hammer (Labor-MIM, Hungary) dropped from 50 cm.

A Binder FD115, (Binder GmbH Tuttlingen, Germany) air-circulating laboratory oven was used for the isothermal thermogravimetric analysis. Numerous dumb-bell shaped samples and also discs of 1 ± 0.1 g were placed in the oven at 120 or 170°C. Five replicates of each polymer composition were taken at one time for tensile strength and hardness measurements, and the discs were weighed and placed back into the oven for further tempering. The results represent the median values of the replicates. All these measurements were carried out after cooling down the samples to room temperature.

TGA was performed by using MOM Derivatograph Q-1500, Hungary (equipped with Derill-X digital system, the data processing was performed on Winder software) at a heating rate of 5°C/min under nitrogen or in air. The sample weights were 105 ± 5 mg. A Perkin Elmer Diamond, Perkin Elmer Instruments, Japan was used for DMTA measurements. All the test samples were heated at a heating rate of

2°C/min from -150 to 200°C at a 1 Hz frequency setting.

The density of the investigated PSiU polymers was determined by using a pycnometer and water at room temperature.

The swelling measurements were carried out at room temperature in THF solvent. All the samples were immersed in THF until their mass changed (m_s); then they were dried in normal air conditions at room temperature until constant mass was obtained (m_d).

3. Results and discussion

Every sample was clear, transparent and slightly yellow. The polymer compositions are listed in Table 1. The names of the compositions indicate the applied chain extender (CE) and whether they contained the polysiloxane diol (SLM) or not. PU sample contained Lupranol-1100, because the pure BDO/Lupranol-1301/MDI blend was brittle, so we formulated a pure organic polyurethane composition in order to obtain a polymer of similar mechanical properties like the other samples with siloxane chain extenders and without polysiloxane.

Our aim was to investigate our samples from a practical point of view, thus we let them dry under normal ambient conditions and we annealed them in air. To prevent the polymers from the negative impact of air humidity we applied 10% excess of isocyanates in each sample. Reacting with water the excess isocyanates form urea, so PUs can be protected or even improved.

3.1. Tensile strength and hardness

The tensile strength (UTS), the elongation at break, the Shore A hardness and the shock resistance (SR) of the polymers are listed in Table 2. Though these materials are very tough, all the samples (of 1 mm thickness) even the ones of negative shock resistance could be bended back by 180° without any damage. From these results it is evident that the structure of the chain extenders has a strong effect on the final physical properties. The chain extenders of higher molecular weight have more flexibility and provide moderate hardness and smaller tensile strength. At constant molar ratio of the polysiloxane the chain length of the disiloxane determines the tensile strength. The chain length of the chain extenders is reflected in their weight percentage as the molar ratios were constant in each group of the compositions (Table 1). Thus the effect of the different chain extenders with or without polysiloxane can be compared as depicted in Figure 3. UTS decreases by increasing the chain length except for SIPOL. In both series, regardless of the presence of SLM, samples containing SIPOL, despite its longer

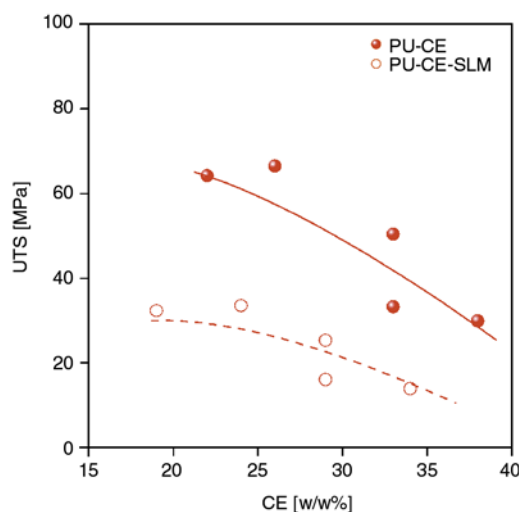


Figure 3. The effect of the different chain extenders (CE) on the ultimate tensile strength (UTS). PU-CE-SLM: polysiloxane incorporated, PU-CE: no polysiloxane in the samples

chains, had higher UTS than samples containing SIMOL. SILOL and SIPA are the same molecular weight, but SILOL has a branched side-chain, so it is shorter and accordingly it has higher UTS.

Trying to find the difference between bis(hydroxyalkylester) and the other disiloxanes (SIKOL-SILOL and SIMOL-SIPA-SIPOL, respectively), we found a less significant correlation between the type of the disiloxane and the tensile strength or the hardness. The chain length and the flexibility are more considerable factors regarding the investigated mechanical properties. Comparing PU-SILOL-SLMi variations with PU-SIPOL-SLMi samples, the ones containing SIPOL showed slightly higher tensile strength and less hardness. It indicates that the carboxyl group has no prevalent effect and the chain length determines the final properties, thus SIPOL with shorter chains has higher tensile strength, but the secondary hydroxyl group containing SILOL results in harder polymers (Figure 4a). Increasing the ratio of the polysiloxane compound induces a significant decrease in the tensile strength, the hardness (Figure 4b) and an increase in the elongation. This phenomenon proved our hypothesis: more flexible but less strong materials can be prepared by adding more polysiloxane SS.

Though the chain extenders and the polysiloxane content have a strong impact on the polymer characteristics, in our samples there is no simple linear relation between them and the resulting tensile strength or other physical properties. The structure of the chain extender has a strong effect on the

Table 2. The mechanical properties of the synthesized polymers

Sample name	UTS [MPa]	Elongation at break [%]	Shore A	SR
PU	35.6	6.1	77	+
PU-SIMOL	64.2	8.6	92	+
PU-SIPOL	66.5	6.9	91	+
PU-SILOL	50.4	5.7	92	-
PU-SIPA	33.2	10.0	69	-
PU-SIKOL	29.9	10.7	79	+
PU-BDO-SLM	41.8	14	68	+
PU-SIMOL-SLM	32.3	12	75	+
PU-SIPA-SLM	16.0	111	60	+
PU-SIKOL-SLM	13.9	192	67	+
PU-SILOL-SLM1	54.0	12	89	+
PU-SILOL-SLM2	33.9	14	85	+
PU-SILOL-SLM	25.3	15	81	+
PU-SIPOL-SLM1	56.2	10	87	+
PU-SIPOL-SLM2	34.6	14	82	+
PU-SIPOL-SLM	33.5	16	78	+

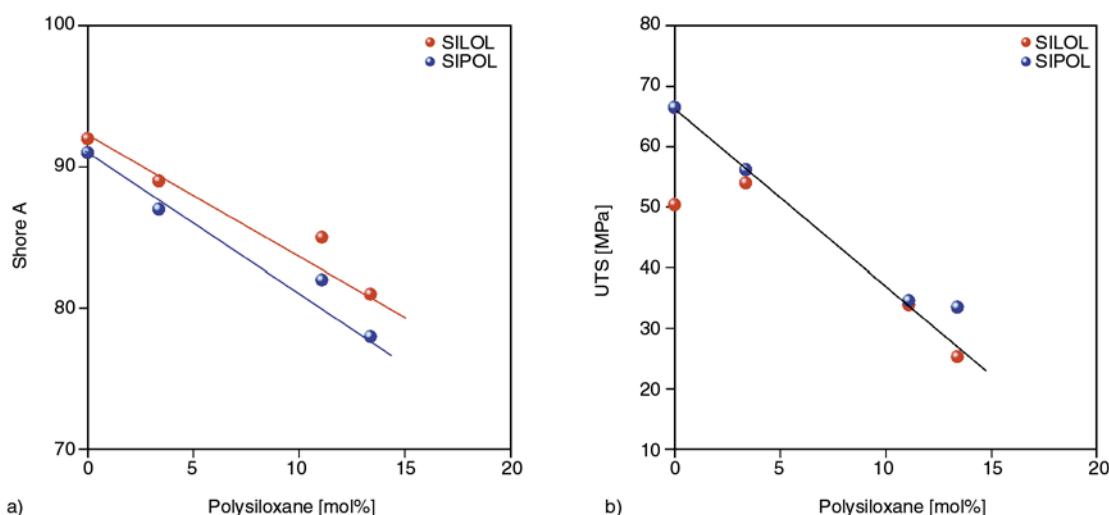


Figure 4. Shore A hardness (a) and UTS (b) in the function of the polysiloxane content when SILOL or SIPOL chain extenders were used

physical properties of the polymers and it determines dominantly the final characteristics together with the crosslink density. Besides, the overall dimethyl siloxane content incorporating the effect of the polysiloxane content and the structure of the disiloxane influence the physical properties as well. The structure of the disiloxanes appears in their weight percentage in the polymer, because their molecular weight increases as their chain length increases at constant molar ratio. Both increasing chain length and the higher polysiloxane content decrease the UTS. So we defined x as a numerical expression for these two factors (Equation (1)):

$$x = w/w\%(CE) \cdot w/w\%(PSi) \quad (1)$$

In the function of x still no exact equation can be determined, but x combined with the overall siloxane content allows us to fit a trend-plane or a trend-line to the represented data as depicted in Fig-

ures 5a and 5b, the corresponding data are listed in Table 3 (polymers without any disiloxane or polysiloxane are mostly not representative in this comparison). These equations can be useful in designing polymers made of similar compounds.

3.2. Isothermal thermogravimetric and mechanical analysis

The thermal stability of a selection of polymers of high UTS was investigated under isothermal conditions at 120 and 170°C, that can occur occasionally under any working condition where PSiUs might be used. The chosen polymer compositions were made of three compounds in which the ratio of the monomers was constant, only the chain extender was different in each material. The reference sample was a PU of which mechanical properties were similar to the other samples. The tensile strength, the elongation at break and the hardness properties at 120°C are listed in the function of time in Table 4,

Table 3. Relationship between the UTS, the overall siloxane content [Me₂SiO] [%], the chain length of the disiloxane chain extenders (incorporated in CE [w/w%]), and the polysiloxane content [w/w%]

Sample name	UTS [MPa]	[Me ₂ SiO] [%]	$x = (CE [w/w\%] \cdot polysiloxane [w/w\%])$	$x/[Me_2SiO]$ [%]
PU-SIPOL	66.5	15.6	0	0
PU-SIPOL-SLM1	56.2	19.9	191	9.58
PU-SILOL-SLM1	54.0	18.4	220	11.96
PU-SIPOL-SLM2	34.6	28.3	422	14.91
PU-SILOL-SLM2	33.9	26.6	507	19.05
PU-SIMOL-SLM	32.3	36.2	609	16.81
PU-SIPOL-SLM	33.5	34.4	704	20.45
PU-SILOL-SLM	25.3	31.9	811	25.41
PU-SIPA-SLM	16.0	36.2	811	22.39
PU-SIKOL-SLM	13.9	29.8	879	29.48

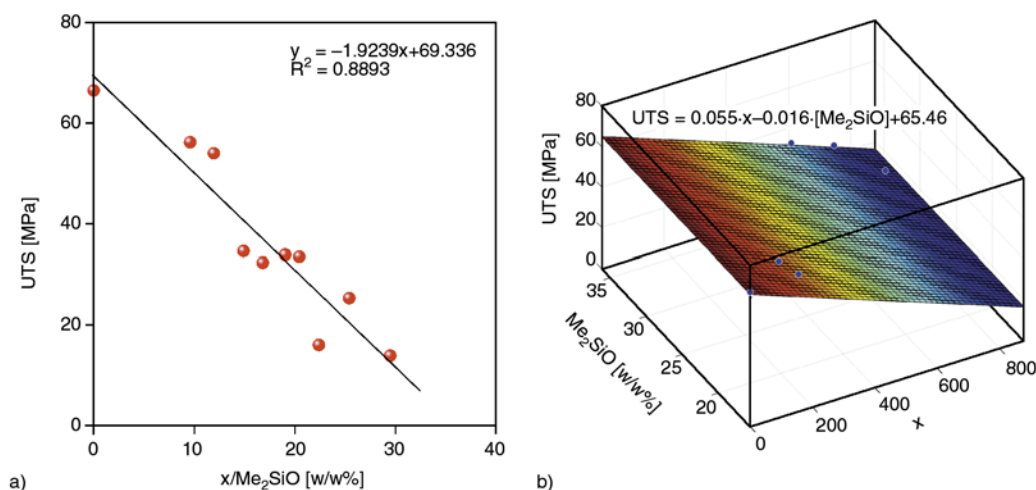


Figure 5. (a) Illustration of the relationship between the combined number made up of the siloxane unit, the chain extender and the polysiloxane content and UTS; (b) 3D diagram illustrating the relationship between the siloxane content, *x* (the combined number made up of the chain extender and polysiloxane content) and UTS

the results of the study at 170°C in Table 5. The weight losses are represented in Figure 6 and 7. Significant differences were observed by using diverse chain extenders in these simple compositions. The behaviour of PU-SILOL was very different from that of the other samples; it was decomposed after one day at 170°C and became too brittle to measure after two days at 120°C. This phenomenon can be attributed to the secondary hydroxy groups as they provide less stable urethane bonds [21]. Both chosen temperatures are lower than the decomposition temperature of the urethane bond, which is

thermally the least stable bond in PSiU systems [13, 16]. The annealing time and temperature were worked out previously by monitoring tensile strength and hardness changes, and this is why it was interesting that after the first day of tempering relatively big weight loss was observed at both temperatures. The most stable polymer samples turned out to be PU and PU-SIKOL. They lost 3.3–3.6% of their mass at 120°C and 14.3–14.6% at 170°C until the end of the study. The most degradable materials were PU-SIPA and PU-SIMOL (besides PU-SILOL) which lost 7.6–8.0% of their weight at 120°C and 23.7–26.8% at 170°C within eight days. Most of the

Table 4. Changes in the mechanical properties after tempering a selection of the samples at 120°C for a given time (with ‘–’ denoted samples were too brittle to measure)

120°C Sample\Time [h]	Tensile strength [MPa]					Elongation at break [%]					Shore A hardness				
	0	25	50	100	230	0	25	50	100	230	0	25	50	100	230
PU	35.6	35.6	31.8	31.6	32.4	6.1	6.1	0.8	2.0	13.0	77	77	89	89	98
PU-SIMOL	64.2	67.5	49.9	53.3	57.7	8.6	3.4	9.7	2.5	10.3	92	91	96	90	95
PU-SIPOL	66.5	49.6	63.5	52.9	68.5	6.9	0.3	8.0	7.9	7.5	91	87	98	98	97
PU-SILOL	50.4	54.1	–	–	–	5.7	12.0	–	–	–	92	94	96	100	100
PU-SIPA	33.2	49.5	45.1	46.6	47.1	10.0	9.0	10.0	0.3	7.0	69	90	87	96	99
PU-SIKOL	29.9	32.2	41.8	40.7	32.8	10.7	2.8	6.5	10.5	7.0	79	80	99	91	88

Table 5. Changes in the mechanical properties after tempering a selection of the samples at 170°C for a given time (with ‘–’ denoted samples were decomposed in the oven)

170°C Sample\Time [h]	Tensile strength [MPa]					Elongation at break [%]					Shore A hardness				
	0	25	50	100	200	0	25	50	100	200	0	25	50	100	200
PU	35.6	28.8	20.2	22.2	31.6	6.1	8.4	7.6	10.0	9.8	77	93	93	95	94
PU-SIMOL	64.2	60.9	37.0	54.5	30.9	8.6	6.7	5.5	5.2	6.6	92	99	100	95	100
PU-SIPOL	66.5	56.5	47.6	73.6	32.4	6.9	14.0	3.7	6.2	0.3	91	96	97	93	100
PU-SILOL	50.4	–	–	–	–	5.7	–	–	–	–	92	–	–	–	–
PU-SIPA	33.2	43.6	45.4	59.9	42.4	10.0	3.7	6.6	6.0	3.6	69	87	91	93	100
PU-SIKOL	29.9	33.7	26.4	29.7	43.5	10.7	6.1	9.0	6.1	9.5	79	85	95	93	100

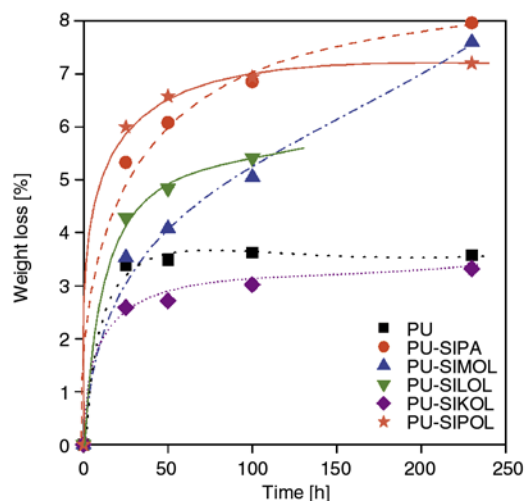


Figure 6. Weight loss (in percentage) of a selection of the samples over time at 120°C

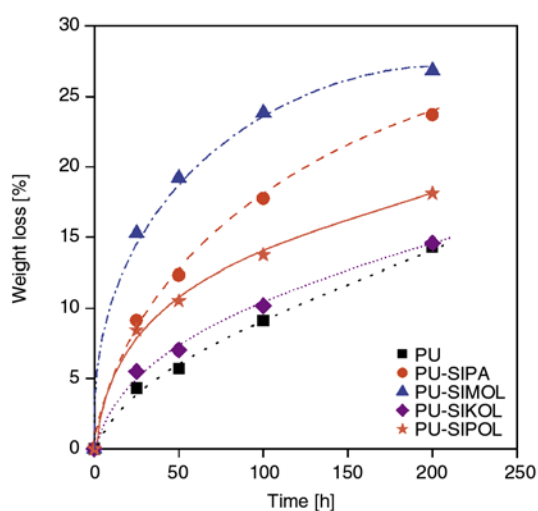


Figure 7. Weight loss (in percentage) of a selection of the samples over time at 170°C

weight loss was observed on the first day at 120°C annealing temperature. During the following eight days further decrease up to 4.1% was measured at any sample, at PU-SIKOL it was only 0.7%, at PU it was 0.2%.

At 170°C the first day was also exceptional, but the following week resulted in a significant weight loss as well. After one day PU lost 4.3%, PU-SIKOL 5.5% and PU-SIMOL 15.3% of their weight. The following week the order of the additional weight losses changed: PU-SIKOL (9.1%) > PU-SIPOL (9.7%) > PU (10.0%) > PU-SIMOL (11.5%) > PU-SIPA (14.6%). The significantly bigger weight loss of the first day can be explained by the evaporation of the volatile compounds such as residual solvent traces and cyclic siloxane oligomers [18].

The longer time the samples were in the oven, the harder, and the darker they became, for example they got even dark brown and some of them got brittle at 170°C. Although the hardness increased explicitly in accordance with the tempering time, the tensile strength values do not follow a monotonous trend line (Tables 4 and 5). The least fluctuation in UTS was observed at PU and PU-SIKOL. These phenomena can be the result of a slow post-polymerization combined with a moderate degradation process. Post-polymerization means a very complex process as we applied an excess of diisocyanate and a high cross-link density. First of all the reaction between the cross-linker and the diisocyanate can be completed during isothermal annealing. Furthermore, the residual isocyanate can react with another neighbouring urethane group forming an allophanate cross-link. It can also react with water from the air resulting in urea first, and if it reacts with another isocyanate group in biuret cross-linking [22].

The isothermal thermogravimetric and mechanical analysis revealed that except for PU-SIOL all samples especially PU and PU-SIKOL have good thermal stability which is reflected in relatively small weight loss and changes in hardness and tensile strength.

3.3. Thermogravimetric analysis (TGA)

A selection of the polymers was analysed under nitrogen and in air by using TGA. The effects of different chain extenders and different polysiloxane contents were studied. TGA data are listed in Tables 6 and 7. The effect of the increasing amount of polysiloxane is shown in Figure 8.

According to the thermogravimetric (TG) and derivative thermogravimetric (DTG) curves at least two but in most cases three degradation steps can be distinguished. Not all the degradation steps go through an inflection point; in some regions the residual weight decreases linearly with the growing temperature. All the degradation steps correlate with the reports published previously.

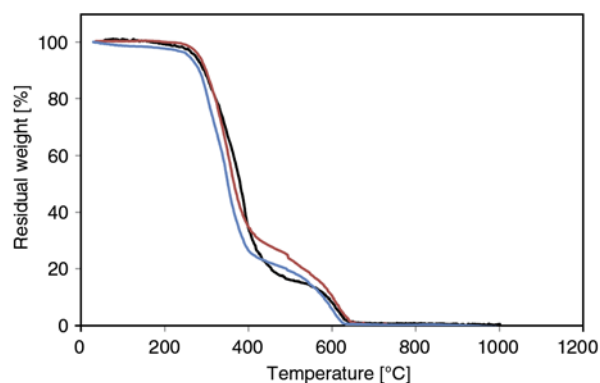
Comparing the selected data listed in Tables 6 and 7, the degradation steps on the TG curves in most cases start at higher temperatures under nitrogen than in air. The initial degradation in air started between 220–260°C, while under nitrogen between 230–275°C; and it was revealed that first urethane

Table 6. TGA data recorded in air. T1, T2, T3 designate the first, second, and third degradation steps respectively. To all steps onset (on), DTG minimum (mid), and offset (off) points are given.

Sample name	Typical temperature [°C]					
	T1 on/mid/off	T2 on/mid/ off	T3 on/ mid/off	at 10% weight loss	at 50% weight loss	at 80% weight loss
PU	260/362/420	–	420/587/647	330	364	460
PU-SIMOL	219/316/393	393/400/478	478/568/640	314	369	525
PU-SIPOL	255/310/495	–	495/595/645	297	339	509
PU-SILOL	252/274/287	287/332/478	478/563/650	294	383	454
PU-SIPA	240/296/320	320/358/540	540/622/659	297	375	465
PU-SIKOL	267/328/392	392/414/492	492/572/620	268	400	495
PU-SILOL-SLM1	222/303/323	323/348/442	442/592/634	283	346	492
PU-SILOL-SLM2	235/341/466	–	466/588/660	300	362	532
PU-SIPOL-SLM1	246/312/386	386–540	540/620/710	298	368	496
PU-SIPOL-SLM2	242/297/322	322/332/370	570/627/695	258	334	524

Table 7. TGA data recorded in nitrogen. T1, T2, T3 designate the first, second, and third degradation steps respectively. To all steps onset (on), DTG minimum (mid), and offset (off) points are given.

Sample name	Typical temperature [°C]					
	T1 on/mid/off	T2 on/mid/ off	T3 on/ mid/off	at 10% weight loss	at 50% weight loss	at 80% weight loss
PU	264/362/420	–	420-760 linear	323	369	410
PU-SIMOL	230/275/288	288/338/520	520-900 linear	300	380	467
PU-SIPOL	253/314/325	325/336/401	401-885 linear	337	357	397
PU-SILOL	246/330/350	350/399/456	456-900 linear	355	408	442
PU-SIPA	271/363/408	–	408-600 linear	337	371	437
PU-SIKOL	275/346/373	373/417/490	490-816 linear	317	395	448
PU-SILOL-SLM1	253/337/378	378/423/500	500/584/640	267	395	451
PU-SILOL-SLM2	227/389/460	–	460/540/668	290	394	534
PU-SIPOL-SLM1	239/300/510	–	510-900 linear	247	347	477
PU-SIPOL-SLM2	240/295/358	358/420/468	468/596/640	253	412	463

**Figure 8.** TG curves of PU-SILOL (black), PU-SILOL-SLM1 (blue), and PU-SILOL-SLM2 (red) recorded in air

bonds degrade causing depolymerization, and it is followed by the loss of the volatile compounds [13, 14, 16, 17]. The relatively high onset temperature in the case of PU might indicate the effect of the cross-links. Using disiloxane chain extenders the initial degradation step was generally shifted to lower temperatures except for PU-SIKOL. As urethane bonds are the least thermally stable in these systems, it is hard to improve the thermal stability of the

polyurethanes with siloxane compounds. On the other hand, the TGA characteristics strongly depend on the used chain extender and on the polysiloxane content. First of all, the simple two-step degradation of PU recorded in air usually splits into three well distinguishable regions which are less distinct under nitrogen. The second stage ranges roughly between 300–500°C and it corresponds to the degradation of the soft segments. The third step that is above 400°C belongs to the decomposition of macrocyclic siloxanes and aromatic compounds. The onset temperature of the third degradation step is occasionally lower under nitrogen than under air, but the offset temperature is significantly higher in nitrogen (up to 900°C, while in air weight losses reach their maximum at max. 710°C). Also, the weight loss in nitrogen is mostly linear in the function of temperature.

Figure 8 depicts the effect of polysiloxane content when SILOL chain extender is applied. The onset temperatures differ already in favour of higher polysiloxane content, but then between 350–380°C PU-SILOL is the least decomposing and above 400°C

PU-SILOL-SLM2 is significantly more stable than the other two samples.

The good thermal stability of the siloxane compounds revealed itself in the last two degradation steps. 50–80% weight loss occurred at significantly higher temperatures in air in the case of siloxane containing polymers than at PU. It was not true under nitrogen in all cases, and also increasing polysiloxane content not necessarily meant slower weight loss. The reason might be the complex structure of the PSiU networks owing to the secondary hydrogen bonds, segment miscibility, HS/SS ratio, etc. If the results of the same samples analysed in air are compared with the ones studied under nitrogen, the following trends can be observed: 50% weight loss is reached under nitrogen at higher temperatures usually, but almost all samples lose 80% of their weight at lower temperatures under nitrogen than in air. These differences show that also thermo-oxidative degradation takes place above 400°C in air. During the oxidation of siloxanes non-volatile silicon-dioxide is formed, thus the measurable weight loss in air is less than under nitrogen.

3.4. Dynamic mechanical thermal analysis (DMTA)

A selection of polymers was investigated by DMTA. T_g -s of the samples were determined from E'' and $\tan\delta$ peaks. On set, maximum and end set points of the peaks are listed in Table 8.

T_{g1} refers to the glass transition temperature of the soft segment which is in our study a polysiloxane diol (SLM). The peak belonging to T_{g2} is usually very moderate if present at all. It might indicate another phase formed mostly by Lupranol-1301 or

an interphase between HS and SS. T_{g3} represents the glass transition temperature of the HS and it is the highest peak on $\tan\delta$ and loss modulus (E'') curves as well. All the peaks are the most intense on the loss modulus curves, thus these diagrams are shown.

The difference between the various chain extenders is illustrated in Figure 9. It is obvious that the properties determined by DMTA depend on the applied chain extender in accordance with the mechanical properties. Comparing T_{g1} s of the soft segments no significant difference was found. This shows that T_{g1} of the polysiloxane chains is irrespective of the applied chain extender. All the other chain extenders lower T_{g2} and T_{g3} and PU-SIKOL-SLM has the lowest values. This indicates that the HS structure is changed but the polysiloxane remains mostly phase separated. The outstanding behaviour of SIKOL can be explained with its long organic chains as SIKOL is the longest one among the investigated chain extenders. Figure 9b represents the effect of the chain extenders' length on the determined T_{g3} values. These data also indicate that applying a disiloxane containing ether or ester bonds does not make significant difference; the chain length of the chain extenders is more dominant.

PU-BDO-SLM compared to the polymers containing a disiloxane chain extender has lower T_{g3} values, which refers to more flexible hard segments than it could be expected. The structure of the hard segments is mostly responsible for the tensile properties [8] and it is reflected in our data as well. If we follow the order of T_{g3} s depicted in Figure 9b and the order of tensile strengths of the same polymers (Figure 3), the two orders are almost the same. Only

Table 8. Glass transition temperatures (T_g) of a selection of polymers according to $\tan\delta$ and E'' data

Sample name	Typical temperature [°C]					
	$\tan\delta$			E''		
	T_{g1} on/mid/off	T_{g2} on/mid/ off	T_{g3} on/ mid/off	T_{g1} on/mid/off	T_{g2} on/mid/ off	T_{g3} on/ mid/off
PU-BDO-SLM	-149/-107/-54	-54/-13/30	30/121/176	-149/-115/-54	-54/-18/32	32/95/190
PU-SIMOL-SLM	-147/-105/-63	-62/-23/15	15/74/148	-147/-113/-62	-62/-23/17	17/50/172
PU-SIPA-SLM	-145/-105/-64	-64/-25/-4	-4/57/136	-145/-113/-62	-50/-26/-1	-1/24/130
PU-SIKOL-SLM	-135/-99/-74	-74/-50/-21	-21/43/133	-133/-113/-71	-71/-54/-17	-17/12/127
PU-SILOL	-140/-92/-41	-41/-10/41	41/78/138	-140/-93/-39	-39/1/44	44/69/130
PU-SILOL-SLM1	-141/-93/-55	-55/-11/15	15/75/145	-142/-97/-52	-52/-14/25	25/52/140
PU-SILOL-SLM2	-145/-105/-54	-54/-19/-10	-10/71/143	-145/-117/-53	-53/-10/16	16/53/135
PU-SILOL-SLM	-145/-107/-52	–	-52/68/150	-142/-115/-54	–	-54/39/150
PU-SIPOL	-120/-92/-54	-54/-16/36	36/74/113	-115/-92/-54	-54/-17/38	38/65/111
PU-SIPOL-SLM1	-142/-93/-50	-50/-18/25	25/69/148	-142/-93/-52	-52/-21/31	31/58/139
PU-SIPOL-SLM2	-143/-103/-65	-65/-24/10	10/67/150	-143/-113/-60	-63/-24/15	15/52/144
PU-SIPOL-SLM	-147/-104/-57	-57/-25/8	8/62/134	-142/-112/-57	-57/-25/8	8/46/132

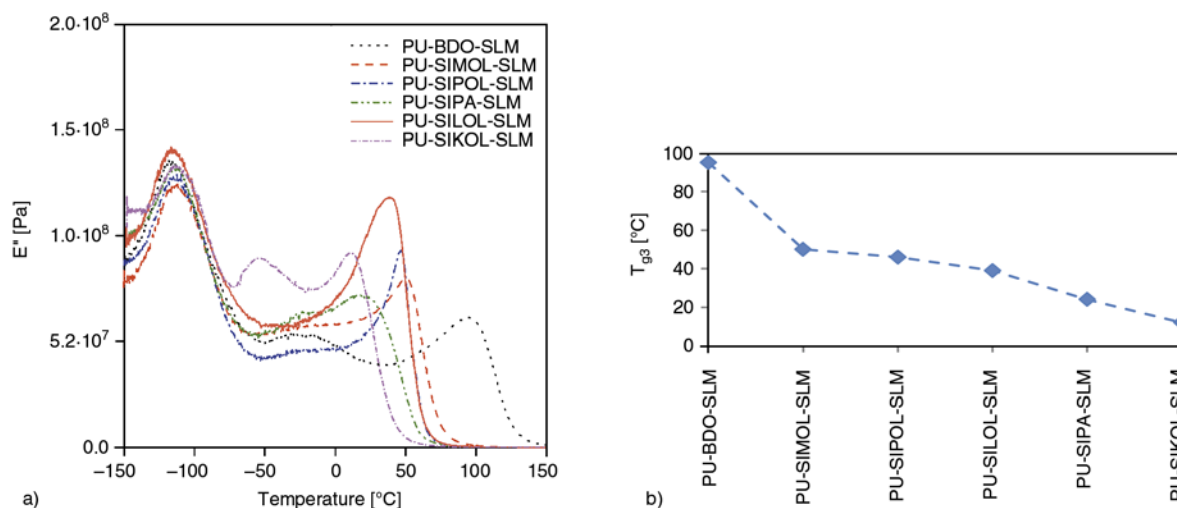


Figure 9. Loss moduli (E'') of a selection of polymers of the same composition containing different chain extenders (a) and T_{g3} values (determined from E'') of the same polymers (b)

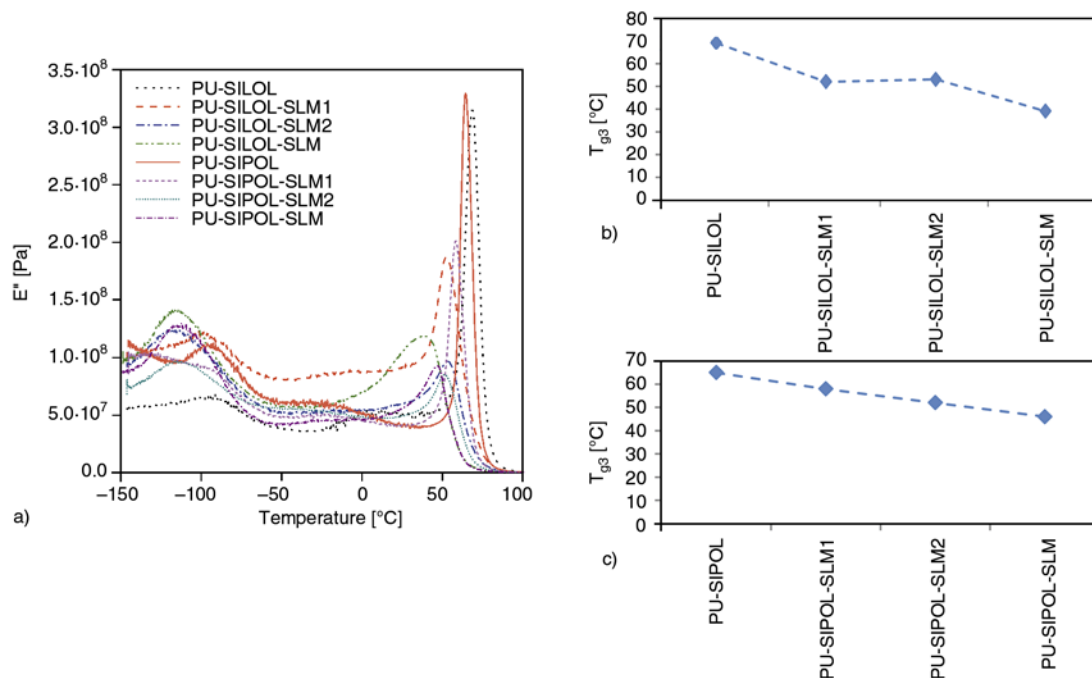


Figure 10. Loss moduli (E'') of a selection of polymers of the same composition containing SILOL or SIPOL and a different amount of polysiloxane (a) and T_{g3} values (determined from E'') of the same polymers (b–c)

PU-SIPOL-SLM stands out with higher UTS than it could be expected according to its T_{g3} . It suggests that SIPOL might form an optimal HS structure with MDI.

We made two series to illustrate the effect of the increasing polysiloxane content (Figure 10a–10c). PU-SILOL and PU-SIPOL did not contain SLM polysiloxane soft segments, while the other samples were prepared with increasing amount of SLM. The glass transition temperatures of the Si-O-Si units were well defined also in PU-SILOL and PU-SIPOL where only disiloxanes were present. As the poly-

siloxane content increased, T_{g1} , T_{g2} , and T_{g3} decreased. The decrease of T_{g2} and T_{g3} can be a result of several impacts. Besides other structural effects the decreasing theoretical cross-link density has a significant influence as the siloxane content increases [23]. Changes in E'' loss moduli at T_{g3} did not show regularity as a function of the increasing polysiloxane content. E'' values did not decrease as the cross-link density increased [15]. It corresponds to our theory: the cross-link density does not have a dominant effect and the aforementioned two effects operate at the same time.

3.5. Cross-link density

Swelling measurements were carried out in order to determine the cross-link density of the investigated samples. Different solvents (toluene, n-butyl acetate, ethanol, isopropyl alcohol) were tested to find the best solvent for our PSiUs. Q_s characterises the swelling properties according to Equation (2):

$$Q_s = 1 + \frac{\rho_p}{\rho_0} \frac{m_s - m_d}{m_d} \quad (2)$$

where ρ_p is the density of the polymer, ρ_0 the density of the solvent, m_s is the weight of the swollen sample, and m_d is the weight of the dried sample [24].

According to Q_s THF was chosen for the solvent of this study.

Swelling of networks is related to their cross-link density, which can be calculated according to the Flory-Rhener equation (Equation (3)):

$$\frac{\rho_p}{\bar{M}_c} = \nu_e = \frac{-[\ln(1 - \nu_2) + \nu_2 + \chi\nu_2^2]}{V_s \left(\nu_2^{\frac{1}{2}} + \frac{\nu_2}{2} \right)} \quad (3)$$

where ρ_p is the polymer density, \bar{M}_c is the average molecular weight between two cross-links, ν_2 is the volume fraction of the polymer in the swollen gel ($\nu_2 = 1/Q_s$), V_s is the specific volume of the solvent (for THF V_s is $81.9 \text{ cm}^3 \cdot \text{mol}^{-1}$), and χ is the polymer-solvent interaction parameter that can be calculated with Equation (4):

$$\chi = \chi_s + \chi_H \approx 0.34 + \frac{V_s}{RT} (\delta_0 - \delta_p)^2 \quad (4)$$

where χ_s and χ_H are the entropic and enthalpic contributions, δ_0 and δ_p are the solubility parameters of solvent and polymer, respectively [24].

As PSiU networks of this study have the highest equilibrium swelling values in THF, we can assume that δ_p of the networks is very close to δ_0 of THF, thus $\delta_0 \approx \delta_p$ and $\chi \approx 0.34$.

Cross-link density is related also to the rubbery plateau modulus according to Equation (5):

$$E = (\nu_e - h\mu)RT \quad (5)$$

where ν_e is the cross-link density, h is an empirical parameter, μ represents the elastically active cross-links, R is the universal gas constant, and T is the temperature in Kelvin [14]. In a highly cross-linked network h approximately equals 0, and we can

assume that E equals the storage modulus E' on the rubbery plateau (it means usually $T = T_{g3} + 80^\circ\text{C}$; where T_{g3} is determined from $\tan \delta$), thus M_c can be calculated according to Equation (6) [14]:

$$M_c = \frac{\rho_p RT}{E'} \quad (6)$$

The density of the investigated PSiU networks ranges between 1.06 and $1.24 \text{ g} \cdot \text{cm}^{-3}$, Q_s was calculated according to Equation (2), and M_c was determined in different ways. The theoretical average molecular weight between cross-links ($M_{c,\text{theo}}$) can be calculated from the compositions. $M_{c,\text{theo}}$ gives the theoretical number of cross-links formed by the covalent bonds of Lupranol-1301. M_c can be determined according to Equation (3) from swelling measurements ($M_{c,\text{swell}}$), and M_c is related to the rubbery plateau modulus as described in Equation (6) ($M_{c,E'}$). All the aforementioned data are listed in Table 9, ($M_{c,E'}$ is given provided there was a rubbery plateau, PU-SIPOL and PU-SILOL-SLM had a yield).

At the first six samples in Table 9 we determined higher $M_{c,\text{swell}}$ -s than $M_{c,\text{theo}}$ -s which were calculated from the compositions. In fact especially PU-SIKOL was less cross-linked than it was designed. These differences indicate that not all the hydroxyl groups of Lupranol-1301 reacted with isocyanates. These samples did not contain longer soft segments, and all the monomers were very reactive, so they might have reacted too fast, and at a certain degree of cross-linking the movement of the monomers could have been hindered, so the reaction stopped before it was completed.

The samples containing SLM polysiloxane were found to be more cross-linked than it was expected. The difference between $M_{c,\text{theo}}$ and $M_{c,\text{swell}}$ is especially big at the PU-CE-SLM series. Though $M_{c,E'}$ values seem to be less accurate in the case of our samples, they support the results of the swelling measurements. The deviation of M_c values determined with different methods is reasonable as described in previous works [25–27], but they can be used for comparison. $M_{c,\text{theo}}$ calculated from the composition takes only the possible chemical cross-links into account, $M_{c,\text{swell}}$ includes the real chemical and physical cross-links while $M_{c,E'}$ determined from mechanical characteristics bears usually a negative deviation from $M_{c,\text{swell}}$. These low empirical M_c values could indicate strong interactions

Table 9. Polymer density (ρ_p), swelling (Q_s), theoretical ($M_{c,theo}$) and empirical molecular weights between cross-links ($M_{c,swell}$; $M_{c,E'}$)

Sample name	ρ_p [g·cm ⁻³]	Q_s	$M_{c,theo}$ [g·mol ⁻¹]	$M_{c,swell}$ [g·mol ⁻¹]	$M_{c,E'}$ [g·mol ⁻¹]
PU	1.15	3.03	1427	1481	–
PU-SIMOL	1.15	3.45	1780	2040	–
PU-SIPOL	1.13	4.15	1893	3102	–*
PU-SILOL	1.18	3.48	2069	2143	2345
PU-SIPA	1.12	4.12	2253	3018	–
PU-SIKOL	1.14	5.92	2237	6831	–
PU-BDO-SLM	1.16	2.78	9480	1197	1090
PU-SIMOL-SLM	1.15	4.38	10520	3569	2466
PU-SIPA-SLM	1.11	3.72	11960	2357	1787
PU-SIKOL-SLM	1.13	4.72	12800	4146	2106
PU-SILOL-SLM1	1.09	3.36	2319	1814	1110
PU-SILOL-SLM2	1.14	3.57	3056	2197	1922
PU-SILOL-SLM	1.17	5.90	11960	6954	–*
PU-SIPOL-SLM1	1.14	3.48	2143	2066	1426
PU-SIPOL-SLM2	1.11	3.93	2880	2657	1587
PU-SIPOL-SLM	1.12	3.96	11080	2747	4622

*yield at $T = T_{g3} + 80^\circ\text{C}$

between the segments, but DMTA results show rather strong phase separation, thus probably the excess of the isocyanates partially reacted with urethane bonds resulting in allophanate cross-links. As the theoretical cross-link density increases, the difference between the expected and measured M_c decreases. The aforementioned observation is reasonable considering that with less cross-linker agent the segment movements are more intense and it favours i.e. the reaction of the excess isocyanate groups with urethane bonds.

The degree of cross-linking has a strong effect on the T_g s and on other physical properties but it is not dominant. The maximum of the T_g peaks varies in a wide range depending mostly on the polymer compositions.

4. Conclusions

According to the results of this study it was revealed that all the tested disiloxane chain extenders were suitable for preparing PSiU networks of good thermal stability and high tensile strength. The tensile strength and the hardness indicate that the structure of the disiloxane chain extenders has a strong effect on the physical properties. At constant polysiloxane content the longer chains the disiloxane possessed the greater flexibility and the lower tensile strength were obtained. The chain extenders of smaller molecular weight that is of shorter chain length gave tougher but still not brittle polymers of up to 66.5 MPa UTS. Increasing the polysiloxane content

the tensile strength decreased, but even of 34–36% siloxane content the tensile strength decreased only to 32–33 MPa when SIPOL or SIMOL was applied. Except for two, all the samples were found to be potentially good coating materials as they showed a good adhesion to aluminum and a good shock resistance. A set of samples of the highest tensile strength was investigated by isothermal thermogravimetry, and also the changes in the tensile strength and hardness were followed at 120 and 170°C. At these temperatures we represented possible ambient conditions that can affect PSiU polymers. Except for SILOL all samples showed a good thermal stability and none of them decomposed at these temperatures over a week.

The thermogravimetric analysis revealed that using disiloxane chain extenders the degradation of the urethane bonds cannot be influenced, still they decompose at about 220–270°C. However, the different chain extenders have effect on the further shape of the TG curves, and usually with higher siloxane content the degradation slows down at the range of 50–80% weight loss.

DMTA studies were carried out to determine glass transition temperatures. Two or three peaks were distinguished on E'' (and also on $\tan\delta$ curves), the first of them belongs to the siloxane soft segments (–107...–92°C), the second might indicate an interphase containing mostly the cross-linker (–50...–10°C), and the third one belongs to the hard segments (43–78°C). T_{g3} was found to be the most sen-

sitive to the changes in the polymer composition. T_{g3} decreases significantly with increasing chain extender chain length and with increasing polysiloxane content.

In summary, the chain length of the applied chain extender, the polysiloxane content and the cross-link density together determine the final characteristics of the polymer dominantly. Varying the structure of the disiloxane, the ratio of the cross-linker and the polysiloxane SSs polymers can be designed and synthesized with diverse physical properties for different purposes.

Acknowledgements

The authors thank Zoltán Demjén (Elastogran) and András Szabó (MagyarLakk Kft.) for the base chemicals.

References

- [1] Kozakiewicz J.: Polysiloxaneurethanes: New polymers for potential coating applications. *Progress in Organic Coatings*, **27**, 123–131 (1996). DOI: [10.1016/0300-9440\(95\)00527-7](https://doi.org/10.1016/0300-9440(95)00527-7)
- [2] Prabu A. A., Alagar M.: Mechanical and thermal studies of intercross-linked networks based on siliconized polyurethane-epoxy/unsaturated polyester coatings. *Progress in Organic Coatings*, **49**, 236–243 (2004). DOI: [10.1016/j.porgcoat.2003.09.018](https://doi.org/10.1016/j.porgcoat.2003.09.018)
- [3] Eberhart A., Zhang Z., Guidoin R., Laroche G., Guay L., De la Faye D., Batt M., King M. W.: A new generation of polyurethane vascular prostheses: Rara avis or ignis fatuus? *Journal of Biomedical Materials Research*, **48**, 546–558 (1999). DOI: [10.1002/\(SICI\)1097-4636\(1999\)48:4<546::AID-JBM22>3.0.CO;2-V](https://doi.org/10.1002/(SICI)1097-4636(1999)48:4<546::AID-JBM22>3.0.CO;2-V)
- [4] Benrashid R., Nelson G. L.: Synthesis of new siloxane urethane block copolymers and their properties. *Journal of Polymer Science Part A: Polymer Chemistry*, **32**, 1847–1865 (1994). DOI: [10.1002/pola.1994.080321006](https://doi.org/10.1002/pola.1994.080321006)
- [5] Stanciu A., Airinei A., Timpu D., Ioanid A., Ioan C., Bulacovschi V.: Polyurethane/polydimethylsiloxane segmented copolymers. *European Polymer Journal*, **35**, 1959–1965 (1999). DOI: [10.1016/S0014-3057\(98\)00294-8](https://doi.org/10.1016/S0014-3057(98)00294-8)
- [6] Wang L. F., Ji Q., Glass T. E., Ward T. C., McGrath J. E., Muggli M., Burns G., Sorathia U.: Synthesis and characterization of organosiloxane modified segmented polyether polyurethanes. *Polymer*, **41**, 5083–5093 (2000). DOI: [10.1016/S0032-3861\(99\)00570-4](https://doi.org/10.1016/S0032-3861(99)00570-4)
- [7] Hernandez R., Weksler J., Padsalgikar A., Runt J.: Microstructural organization of three-phase polydimethylsiloxane-based segmented polyurethanes. *Macromolecules*, **40**, 5441–5449 (2007). DOI: [10.1021/ma070767c](https://doi.org/10.1021/ma070767c)
- [8] Liao S. K., Jang S. C., Lin M. F.: Phase behavior and mechanical properties of siloxane-urethane copolymer. *Journal of Polymer Research*, **12**, 103–112 (2005). DOI: [10.1007/s10965-004-2501-7](https://doi.org/10.1007/s10965-004-2501-7)
- [9] Yilgor I., Yilgor E.: Structure-morphology-property behavior of segmented thermoplastic polyurethanes and polyureas prepared without chain extenders. *Polymer Reviews*, **47**, 487–510 (2007). DOI: [10.1080/15583720701638260](https://doi.org/10.1080/15583720701638260)
- [10] Pergal M. V., Antić V. V., Ostojić S., Marinović-Cincović M., Donlagić J.: Influence of the content of hard segments on the properties of novel urethane-siloxane copolymers based on a poly(ϵ -caprolactone)-b-poly(dimethylsiloxane)-b-poly(ϵ -caprolactone) triblock copolymer. *Journal of the Serbian Chemical Society*, **76**, 1703–1723 (2011). DOI: [10.2298/JSC110307146P](https://doi.org/10.2298/JSC110307146P)
- [11] Adhikari R., Gunatillake P. A., McCarthy S. J., Meijs G. F.: Low-modulus siloxane-based polyurethanes. I. Effect of the chain extender 1,3-bis(4-hydroxybutyl) 1,1,3,3-tetramethyldisiloxane (BHTD) on properties and morphology. *Journal of Applied Polymer Science*, **83**, 736–746 (2002). DOI: [10.1002/app.2268](https://doi.org/10.1002/app.2268)
- [12] Adhikari, R., Gunatillake P. A., McCarthy S. J., Bown M., Meijs G. F.: Low-modulus siloxane-polyurethanes. Part II. Effect of chain extender structure on properties and morphology. *Journal of Applied Polymer Science*, **87**, 1092–1100 (2003). DOI: [10.1002/app.11558](https://doi.org/10.1002/app.11558)
- [13] Chuang F. S., Tsen W. C., Shu Y. C.: The effect of different siloxane chain-extendors on the thermal degradation and stability of segmented polyurethanes. *Polymer Degradation and Stability*, **84**, 69–77 (2004). DOI: [10.1016/j.polymdegradstab.2003.10.002](https://doi.org/10.1016/j.polymdegradstab.2003.10.002)
- [14] Džunuzović, J. V., Pergal M. V., Poręba R., Ostojić S., Lazić N., Spirkova M., Jovanović S.: Studies of the thermal and mechanical properties of poly(urethane-siloxane)s cross-linked by hyperbranched polyesters. *Industrial and Engineering Chemistry Research*, **51**, 10824–10832 (2012). DOI: [10.1021/ie300927z](https://doi.org/10.1021/ie300927z)
- [15] Stanciu A., Bulacovschi V., Lungu M., Vlad S., Balint S., Oprea S.: Mechanical behaviour of crosslinked poly(ester-siloxane) urethanes. *European Polymer Journal*, **35**, 2039–2044 (1999). DOI: [10.1016/S0014-3057\(98\)00286-9](https://doi.org/10.1016/S0014-3057(98)00286-9)
- [16] Yeh J-T., Shu Y-C.: Characteristics of the degradation and improvement of the thermal stability of poly(siloxane urethane) copolymers. *Journal of Applied Polymer Science*, **115**, 2616–2628 (2010). DOI: [10.1002/app.29023](https://doi.org/10.1002/app.29023)

- [17] Chuang F-S., Tsi H-Y., Chow J-D., Tsen W-C., Shu Y-C., Jang S-C.: Thermal degradation of poly(siloxane-urethane) copolymers. *Polymer Degradation and Stability*, **93**, 1753–1761 (2008).
DOI: [10.1016/j.polymdegradstab.2008.07.029](https://doi.org/10.1016/j.polymdegradstab.2008.07.029)
- [18] Liptay G., Nagy J., Weis J. C., Borbely-Kuszmán A.: Thermoanalytical investigations of silicone caoutchouc polymers and silicone rubbers, I. *Journal of Thermal Analysis*, **32**, 1421–1433 (1987).
DOI: [10.1007/bf01913343](https://doi.org/10.1007/bf01913343)
- [19] Liao S. K., Jang S. C., Lin M. F.: Thermal degradation of imide-containing siloxane-urethane copolymer. *Journal of Polymer Engineering*, **27**, 197–217 (2007).
DOI: [10.1515/POLYENG.2007.27.3.197](https://doi.org/10.1515/POLYENG.2007.27.3.197)
- [20] Pusztai E., Nagy J., Wagner Ö.: Synthesis and characterization of some bis(hydroxyalkyl)- and bis(hydroxyester)-functionalized disiloxanes. *Main Group Metal Chemistry*, **35**, 91–97 (2012).
DOI: [10.1515/mgmc-2012-0010](https://doi.org/10.1515/mgmc-2012-0010)
- [21] Ionescu M.: Chemistry and technology of polyols for polyurethanes. Rapra Technology Limited, Shropshire, UK (2005).
- [22] Meier-Westhues U.: Polyurethanes: Coatings, adhesives and sealants. Vincentz, Hannover (2007).
- [23] Andrady A. L., Sefcik M. D.: Glass transition in poly(propylene glycol) networks. *Journal of Polymer Science Part B: Polymer Physics Edition*, **21**, 2453–2463 (1983).
DOI: [10.1002/pol.1983.180211203](https://doi.org/10.1002/pol.1983.180211203)
- [24] Burel F., Feldman A., Bunel C.: Hydrogenated hydroxy-terminated polyisoprene (HHTPI) based urethane network: Network properties. *Polymer*, **46**, 483–489 (2005).
DOI: [10.1016/j.polymer.2004.11.027](https://doi.org/10.1016/j.polymer.2004.11.027)
- [25] Sekkar V., Bhagawan S. S., Prabhakaran N., Rao M. R., Ninan K. N.: Polyurethanes based on hydroxyl terminated polybutadiene: Modelling of network parameters and correlation with mechanical properties. *Polymer*, **41**, 6773–6786 (2000).
DOI: [10.1016/S0032-3861\(00\)00011-2](https://doi.org/10.1016/S0032-3861(00)00011-2)
- [26] Sekkar V., Narayanaswamy K., Scariah K. J., Nair P. R., Sastri K. S., Ang H. G.: Evaluation by various experimental approaches of the crosslink density of urethane networks based on hydroxyl-terminated polybutadiene. *Journal of Applied Polymer Science*, **103**, 3129–3133 (2007).
DOI: [10.1002/app.24751](https://doi.org/10.1002/app.24751)
- [27] Sekkar V.: Comparison between crosslink densities derived from stress–strain data and theoretically data evaluated through the α -model approach for a polyurethane network system based on hydroxyl terminated polybutadiene and isophorone-diisocyanate. *Journal of Applied Polymer Science*, **117**, 920–925 (2010).
DOI: [10.1002/app.31643](https://doi.org/10.1002/app.31643)

The effect of halloysite modification combined with *in situ* matrix modifications on the structure and properties of polypropylene/halloysite nanocomposites

V. Khunova^{1*}, J. Kristóf², I. Kelnar³, J. Dybal³

¹The Slovak University of Technology, Faculty of Chemical and Food Technology, Institute of Polymer Materials, Radlinského 9, 812 37 Bratislava, Slovakia

²Institute of Environmental Engineering, University of Pannonia, H-8200 Veszprém, P.O. Box 158, Hungary

³Institute of Macromolecular Chemistry, Academy of Science of the Czech Republic, Heyrovsky Sq. 2, 16206 Prague, Czech Republic

Received 13 November 2012; accepted in revised form 4 February 2013

Abstract. The effect of various modifications/intercalations of halloysite and the combination of these modifications with *in situ* PP matrix modification was investigated with respect to the structure and properties of the polypropylene/halloysite nanocomposites. Hexadecyl-tri-methyl-ammonium-bromide (HEDA), 3-aminopropyltrimethoxysilane and urea were used as the intercalators/modifiers. The best intercalation was found for urea, although an unexpected insignificant impact on the mechanical properties also resulted as a consequence of the urea polarity and the significant decrease in PP crystallinity. However, the simultaneous application of 4,4'-diphenylmethylene dimaleinimide (DBMI) brought about an increase in the mechanical behavior by increasing the halloysite/PP affinity as a result of *in situ* matrix modification. This effect was further supported by coupling between the PP and halloysite (HNT) in the system containing urea-intercalated HNT. This can be explained by the occurrence of a urea-supported reaction between the imide ring of DBMI and the OH groups of the HNT, which resulted in the best mechanical behaviors achieved in this study.

Keywords: nanocomposites, polypropylene, halloysite, modification

1. Introduction

The significant effort devoted to the development of polymer nanocomposites based on layered silicates has resulted in tremendous progress toward our understanding of the structure and properties of these scientifically and industrially important materials. However, several thermodynamic obstacles remain to be solved before the wide application of polymer/clay nanocomposites on the industrial scale can be realized [1–3].

Recently, an exponentially increasing number of papers have been published on the successful application of natural halloysite (HNT) in nanocompos-

ites based on different polymer matrices [4]. In a recent review paper [5], a number of examples were given, documenting the significant potential of halloysite to compete with montmorillonite (MMT), which is currently the most commercially exploited clay for the preparation of polymer nanocomposites. This is generally due to the relative ease with which halloysite can be dispersed in polymer matrices in addition to its abundance, availability and biocompatibility.

Halloysite is naturally occurring aluminosilicate clay, frequently with a hollow tubular morphology [6]. The two main polymorphs of halloysite are the

*Corresponding author, e-mail: viera.khunova@stuba.sk

hydrated form, $\text{Al}_2\text{Si}_2\text{O}_5(\text{OH})_4 \cdot 2\text{H}_2\text{O}$, with a basal distance of approximately 10 Å and the dehydrated form, $\text{Al}_2\text{Si}_2\text{O}_5(\text{OH})_4$, which is identical to kaolinite. The hydrated form is irreversibly converted to the dehydrated form upon drying below 100°C. Water loss sharpens the basal reflections and reduces the basal d-spacings to approximately 7.2 Å, although this value is never so small as that of typical kaolinite (7.14 Å) [7]. In the hydrated halloysite, the TO sheets, which are double layers consisting of Si-centered tetrahedral and Al-centered octahedral layers, are separated from each other by a water monolayer. Due to mismatch between the siloxane and gibbsite layers, halloysite occurs in the form of nanotubes [8].

A further difference between the layered silicate-like montmorillonite (MMT) and halloysite is the significantly lower cation exchange capacity (CEC) of HNT for modification via ionic exchange.

However, in halloysite, nanocomposites with highly polar polymer contents [9–12], such as PVC [9, 10], PA [11, 12], or epoxy [13], require no modification/treatment of the halloysite for the preparation of melt-mixed polymer nanocomposites with well distributed HNT. With non-polar polyolefins such as PP, due to the highly hydrophobic nature of PP, it is necessary to modify not only the halloysite [14–17], but also the polymer matrix to increase the polarity of PP [18–21]. Additionally, modification of halloysite by γ -metacryloxypropyl-trimethoxysilane leads to enhanced thermal stability and decreases flammability [22]. An alternative approach for increasing the interfacial interactions is the use of electron transferring modifiers. Examples of electron-transferring modifiers [23, 24] used in PP/halloysite composites include 2-bis(2-benzoxazolyl)tiophene [23] and N-cyclohexyl-2-benzothiazole sulfonamide [24]. A further example utilizes hydrogen bond bridged halloysite with polypropylene; this can be achieved with the use of melamine, diphenyl guanine, 2,4,6-trimercapto-s-triazine, melamine cyanuric acid, tri-(2-hydroxyethyl)isocyanurate or β -cyclodextrin [25]. The authors documented a significant improvement in the resulting end use properties of the PP composites containing 30 wt% halloysite. The last referred example of PP/halloysite composite modification was carried out with bis-2-hydroxyethyl, quaternary ammonium solutions [26]. However, only negligible increases in the mechanical properties were observed.

In our earlier works, we documented [27–30] an effective alternative for increasing the PP polarity by the addition of pre-fabricated maleated polypropylene for *in situ* modification, using bifunctional compounds such as 4,4'-diphenylmethylenedimaleinimide (DBMI) and 1,3-phenylene dimaleimide (BMI).

This work highlights the effects of halloysite modification by hexa-decyl-tri-methyl-ammonium-bromide, 3-aminopropyltrimethoxysilane and urea individually as well as in combination using *in situ* modification of the PP matrix by 4,4'-diphenylmethylenedimaleinimide (DBMI).

2. Experimental

2.1. Materials

Halloysite was recovered from Biela Hora, Michalovce, Slovakia.

Before modification, the halloysite was ground into powder using a laboratory ball mill. Next, the powdered halloysite was purified and sieved to obtain a fraction smaller than 50 microns.

Polypropylene homopolymer (type 575 P) with a melt flow rate of 11.0 g/10 min (230°C/2.16 kg) was provided by Sabic, Sittard-Geleen, Netherlands.

The silane used was 3-aminopropyltrimethoxysilane, provided by Sigma Aldrich, USA.

The alkylamine used was hexa-decyl-tri-methyl-ammonium-bromide (HEDA), obtained from Sigma Aldrich, USA.

Analytical grade urea was purchased from Merck, Hungary.

The reactive modifier was 4,4'-diphenylmethylenedimaleinimide (DBMI), from VUCHT, Bratislava, Slovakia.

2.2. Halloysite modification

2.2.1. Halloysite modification by

hexa-decyl-tri-methyl-ammonium-bromide

The purified ground halloysite was treated in 5% solution of hexa-decyl-tri-methyl-ammonium-bromide (HEDA) at 80°C for 24 h. After filtration, the HNTs were dried in a vacuum oven at 60°C for 24 h. The dried powder was ground and sieved again [19].

2.2.2. Halloysite modification by

3-aminopropyltrimethoxysilane

The modification of halloysite by 3-aminopropyltrimethoxysilane was performed by adding silane

A1100 in water/ethanol solution adjusted by acetic acid to pH 5.0. The detailed procedure for this modification is given in [17].

2.2.3. Halloysite intercalation by urea

The intercalation of urea into the halloysite was performed by mechanochemical means (dry grinding). A 10 g mixture of the clay and urea (mixed in a 2:1 ratio) was generated using a Fritsch Pulverisette 5/2 type laboratory planetary mill. Milling was performed for 30 min in an 80 cm³ capacity stainless steel bowl using 29 (110.3 g total) stainless steel balls (10 mm diameter each). The rotation speed was 374 rpm.

2.3. Composite preparation

The composites were formed from polypropylene and untreated and/or intercalated halloysite (at a ratio of 5 wt%) via melt mixing in a Brabender W50-E chamber. In the case of *in situ* matrix modification to increase PP polarity, 1% DBMI was added [27]. The mixing temperature was 200°C, and the rotor speed was 200 rpm. Dog bone-shaped specimens (a gauge length of 40 mm) were prepared in a laboratory micro-injection molding machine (DSM). The barrel temperature was 200°C, and the mold temperature was 70°C.

2.4. Analysis and characterization

Wide-angle X-ray diffraction patterns (WAXS) were collected using a powder diffractometer (HZG/4A from Freiburger Präzisionsmechanik GmbH, Germany), using monochromatic Cu K α radiation. Analyses were performed on the surface of the compression-molded sheets. X-ray diffraction (XRD) analyses were carried out on a Philips PW 3710 type diffractometer equipped with a PW 3020 vertical goniometer and a curved graphite diffracted beam monochromator. The radiation applied was Cu K α , generated from a broad-focus Cu tube operated at 50 kV and 40 mA. The samples were measured in a continuous scan mode with 0.02°/s scanning speed. Data collection and evaluation were performed with PC-APD 3.6 software. Back-packed mounts of finely powdered samples were used to eliminate preferential orientation.

Transmission electron microscopy (TEM) observations were performed on a TESLA BS 300 combined scanning and transmission electron microscope, using ultrathin (60 nm) sections, which were cut under liquid N₂ with an Ultracut UCT (Leica) ultramicrotome.

Tensile tests were carried out at 22°C using an Instron 5800 apparatus at a crosshead speed of 20 mm/min. *E* modulus and stress-at-break (σ_b) were evaluated. The average data from at least eight replicates were reported.

ATR FTIR spectra were collected on a Nicolet Nexus 870 FTIR spectrometer purged with dry air and equipped with a MCT detector. The samples were measured on a horizontal micro-ATR Golden Gate unit (SPECAC) with a diamond prism. The spectra were processed with advanced ATR correction using the OMNIC software.

DRIFT spectra were recorded by means of a Bruker Equinox 55 type FTIR spectrometer equipped with a room-temperature DTGS detector and a Harrick DRIFT adapter at a resolution of 2 cm⁻¹. In all cases, 512 spectra (scans) were summed. For the halloysite samples, KBr was used as the background, while for the polymer composites the background spectra were recorded with an aluminum mirror.

The model quantum mechanical calculations were performed with density functional theory (DFT) using the Gaussian 03 program package. The B3LYP functional and the 6-31G (*d*) basis sets were used and the optimizations were unconstrained. Vibrational frequencies of the normal modes were scaled by the standard scaling factor 0.96 [31].

3. Results and discussion

3.1. Characterization of halloysite

The chemical composition of the studied halloysite, which was recovered from location Biela Hora, Michalovce, Slovakia is given in Table 1.

The chemical composition is similar to that of other halloysites/kaolinites. The amount of dehydroxylation water is 14.32%, which is very close to the theoretical value (13.96%).

From the TEM analyses (Figure 1) it is evident, that the halloysite Biela Hora has a favorable for polymer composites tubular particle shapes with diam-

Table 1. The chemical composition of the halloysite Biela Hora, Slovakia

Composition	SiO ₂	Al ₂ O ₃	Fe ₂ O ₃	CaO	MgO	K ₂ O	Na ₂ O	TiO ₂	LOI
wt%	45.48	33.74	1.27	0.39	0.10	0.02	0.02	0.05	17.41

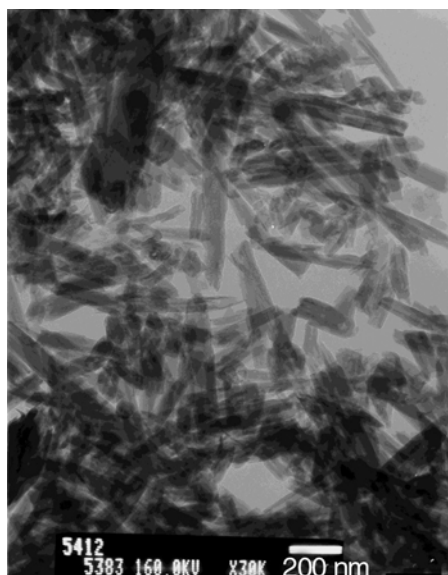


Figure 1. TEM micrographs of pristine halloysite, Biela Hora, Slovakia

eter 30–60 nm and the length from 200 up to 400 nm.

The FTIR (Figure 2) spectrum of the halloysite confirms that the band at 3695 cm^{-1} belongs to the stretching vibration of the inner surface OH groups, while the stretching band of the inner groups occurs at 3622 cm^{-1} . The inner surface OH groups are connected to the Al-centered octahedral sheets and form hydrogen bonds with the oxygen sheet in the next double layer. The other two inner surface OH groups at approximately 3650 and 3670 cm^{-1} cannot be observed, which is typical of halloysites. The stretching band of the inner OH groups, which is located in the plane common to both the tetrahedral and octahedral sheets, is not accessible by the reagent molecules, thus the peak always appears at the same position. The bands at 3603 and 3554 cm^{-1} belong to isolated and adsorbed water molecules, respec-

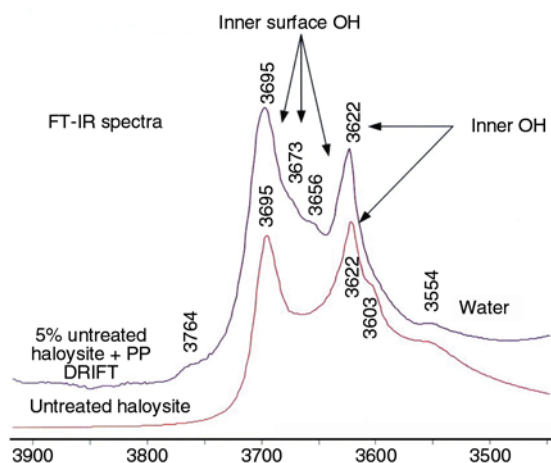


Figure 2. FTIR analysis of the halloysite

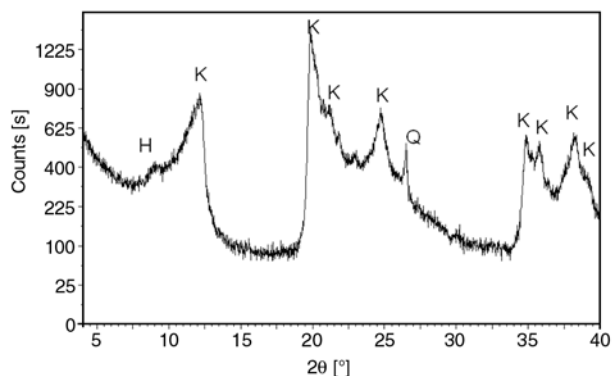


Figure 3. X-ray diffraction patterns of the pristine halloysite (H: halloysite; K: kaolinite/dehydrated halloysite; Q: quartz)

tively. Once the untreated halloysite is mixed into PP at 5% loading, the DRIFT spectrum is significantly modified. The hidden inner OH bands appeared at 3673 and 3656 cm^{-1} (similar to kaolinites), and the band at 3603 cm^{-1} (assigned to the isolated water molecules) disappeared. This observation indicates that the halloysite is present in the PP matrix in dehydrated form. The presence of the shoulder peak at 3764 cm^{-1} is difficult to explain. This feature is either an overtone or a combination band. The XRD pattern of the original unmodified halloysite clay displays 001 reflections at 10.2 and 7.2 Å (Figure 3). The 10.2 Å reflection belongs to the intact portion of halloysite, which possesses a water monolayer between the clay double layers, while the 7.2 Å band represents dehydrated halloysite. Based on the XRD pattern, the dehydrated form constitutes approximately 80% of the mineral.

3.2. Influence of modification on the HNT structure

As noted earlier, two inevitable steps are necessary to prepare polymer nanocomposite materials with advanced properties. These steps include intercalation of the clay and the establishment of sufficient interfacial adhesion between the polymer matrix and the filler surface. This study compares the influence of 3 distinct types of modifiers (alkylamine, silane and urea) on the structure from the perspective of intercalation/delamination of the halloysite and fillers; this process was used to establish successful halloysite modification/intercalation. As evident from Table 2 and Figure 4, the modification of halloysite by HEDA and silane caused no alteration to the basal d-spacing or the halloysite structure. Unlike the alkylamine and silane treat-

Table 2. The effect of modification on the basal d-spacing of the PP/HNT nanocomposites

Sample	2θ [°]	d-spacing [Å]
PP + 5 wt% untreated HNT	12.170	7.27
PP + 5 wt% HNT modified urea	8.140	10.85
PP + 5 wt% HNT modified urea + 1 wt% DBMI	8.115	10.89
PP + 5 wt% HNT modified HEDA	12.200	7.24
PP + 5 wt% HNT modified HEDA + 1 wt% DBMI	12.175	7.29
PP + 5 wt% HNT modified silane	12.130	7.29
PP + 5 wt% HNT modified silane + 1 wt% DBMI	12.185	7.29

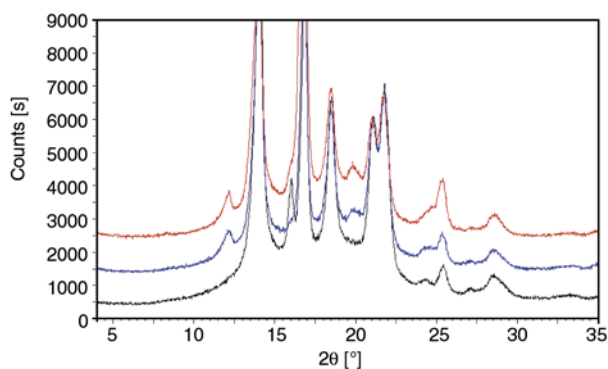


Figure 4. XRD patterns of the unfilled PP (black line), PP containing 5 wt% intercalated by HEDA (blue) and PP containing of 5 wt% intercalated by HEDA and 1 wt% DBMI (red line)

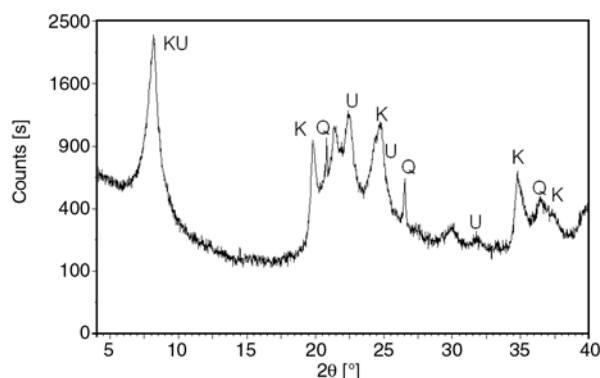


Figure 5. X-ray diffraction pattern of the urea-intercalated halloysite (H: halloysite; K: kaolinite/dehydrated halloysite; Q: quartz, U:urea)

ments, the modification of halloysite by urea resulted in a significant increase of the d-spacing. As evident from Figure 5 (approximately no intensity remains at the 7.27 Å peak), an almost complete expansion of the double layers has occurred as a result of urea intercalation.

3.3. Effect of HNT modification on the properties of the PP nanocomposites

From Table 3, which shows the mechanical behavior of the nanocomposites containing 5 wt% HNT, it can be observed that the addition of untreated hal-

Table 3. The effects of the HEDA, silane and urea modifications on the mechanical properties of the HNT/PP nanocomposites

Blend composition	σ_b [MPa]	E [MPa]
Neat PP	36.3±0.4	1340±45
PP + 5 wt% untreated HNT	36.5±0.4	1440±84
PP + 5 wt% HNT modified HEDA	36.5±0.3	1547±35
PP + 5 wt% HNT modified silane	36.2±0.6	1495±65
PP + 5 wt% HNT modified urea	36.5±0.8	1449±30

loysite to the PP caused an insignificant influence on the mechanical properties, which has been found in similar studies using other HNT sources [14, 15]. This can be explained by the low affinity between the filler particles and the polymer matrix, which was also confirmed by the presence of relatively rough HNT particles (Figures 6a–6c). Furthermore, as indicated by the DSC results, the presence of the HNT induced a detrimental effect on the matrix, evidenced as a reduction in matrix crystallinity (Table 4).

The modification of halloysite by HEDA resulted in an increased modulus without a complementary increase in tensile strength (Table 3). The low increase in the d-spacing values (Table 2) indicates the (low) extent to which modification was achieved. Moreover, by taking into account the significant nucleating activity of HEDA on PP, as documented by DSC (Table 4), the main benefit of HEDA appears to be compensation of the reduced matrix crystallinity. As mentioned above, the crystallinity was reduced by the presence of the neat HNT itself. Similar results were found for the composites containing silane-modified HNT (Table 3): both negligible enhancements in the mechanical properties and the d-spacing values (Table 2) were found, corresponding with the low extent of modification achieved in this case, as well.

In the case of urea-modified halloysite, the significant increase in the d-spacing (Table 2) indicates that this procedure yielded the best intercalation abil-

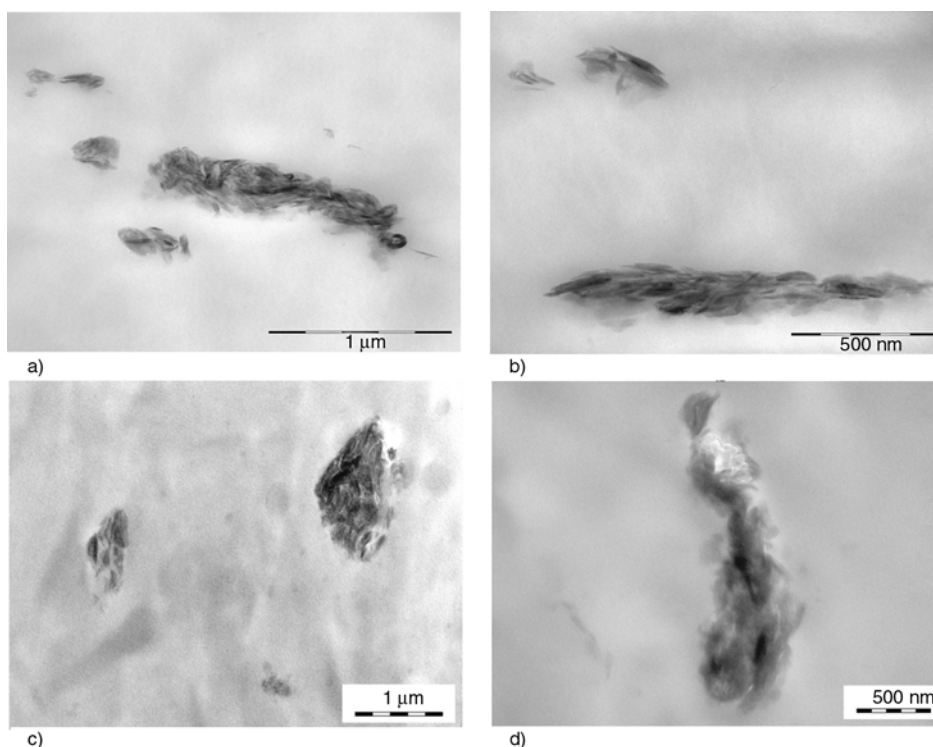


Figure 6. TEM micrographs of the untreated PP/halloysite composites (a, b) and the PP/urea- intercalated halloysite composites modified by DBMI (c, d)

Table 4. Influence of 5 wt% of halloysite on PP crystallinity

Sample	T _m [*]	ΔH [*]	Crystallinity [%]
Neat PP	166.0	105.0	46.1
PP + 5 wt% untreated HNT	163.0	88.6	41.0
PP + 5 wt% untreated HNT + 1 wt% DBMI	164.4	91.1	42.2
PP + 5 wt% untreated HNT + 2 wt% DBMI	159.9	87.7	40.3
PP + 5 wt% untreated HNT + 3 wt% DBMI	162.9	94.0	43.2
PP + 5 wt% HNT modified HEDA	162.7	94.7	43.5
PP + 5 wt% HNT modified HEDA + 1 wt% DBMI	159.7	81.3	37.3
PP + 5 wt% HNT modified silane	166.1	122.8	56.3
PP + 5 wt% HNT modified silane + 1 wt% DBMI	165.0	76.6	35.8
PP + 5 wt% HNT modified urea	170.0	48.0	22,3
PP + 5 wt% HNT modified urea + 1 wt% DBMI	170.0	55.5	25.5

*1st run

ity among the modifiers applied. Hence, the behavior of the PP composites containing urea-modified HNT was highly unexpected in that we did not observe any improvement in the investigated mechanical properties (Table 3). One reason for this might be the identical d-spacings of both compounds (urea-modified halloysite and urea-modified halloysite/PP nanocomposites), indicating the low extent to which the PP chains were able to intercalate into the halloysite structure (Table 2). This was likely due to the unfavorable polarity (hydrophilicity) of this modification, which yielded a low affinity to PP.

The effect can be clearly seen in the DSC results (Table 4), which indicate the presence of a significant negative effect of the urea (intercalated into the HNT) on crystallinity and thus the mechanical parameters of PP.

These results indicate that, to achieve more favorable mechanical behavior, simultaneous modification of the PP matrix is necessary. Based on our earlier work, for this purpose, we used a reactive modifier, 4,4'-diphenyl methylene-dimaleinimide (DBMI) [27–30].

3.4. Effect of *in situ* PP matrix functionalization on the modified HNT/PP composites

From Table 5, it is apparent that modification with DBMI caused an increase in the strength and the modulus in all nanocomposites studied. This finding is in agreement with the highly effective nature of this reactive interfacial modifier, which also has been found for other composite systems [27–30]. From Table 4, it is evident that DBMI does not affect the crystallinity of the PP matrix.

Although in each of the PP composites containing untreated HNT, alkylamine (HEDA)-treated HNT and silane-treated HNT, the increase in the matrix polarity due to DBMI modification was comparable, a more significant increase in the studied properties was observed for the urea-treated halloysite. In this case, urea provides hydrogen bonds, which link the HNT with the modified PP. At the same time, DBMI acts as a coupling agent due to parallel linking to HNT facilitated by imide ring opening due to the presence of urea followed by reaction with the OH groups of the HNT.

This assumption was confirmed by the FTIR spectra (Figure 7), which demonstrates that, in comparison to pure HNT/PP, the application of DBMI to HNT/PP yields a new band at 1514 cm⁻¹ (Figures 7a and 7b). This new band was assigned to the C=C double bond in the imide ring. When additional urea is present in the mixture, this band is shifted from 1514 to 1495 cm⁻¹ (Figure 7c). This shift indicates opening of the imide ring, as confirmed by the DFT (density functional theory) quantum mechanical calculations (Figure 8).

With respect to the model structure shown in Figure 8a, the calculated frequency of the band corresponding to the imide ring is 1501 cm⁻¹. Here, it should be noted that, although DFT calculations do

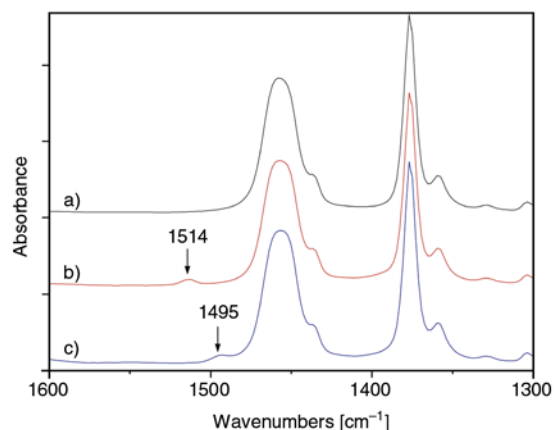


Figure 7. FTIR spectra of the PP/HNT/urea (a), the PP/HNT/DBMI (b) and the PP/HNT/DBMI/urea (c)

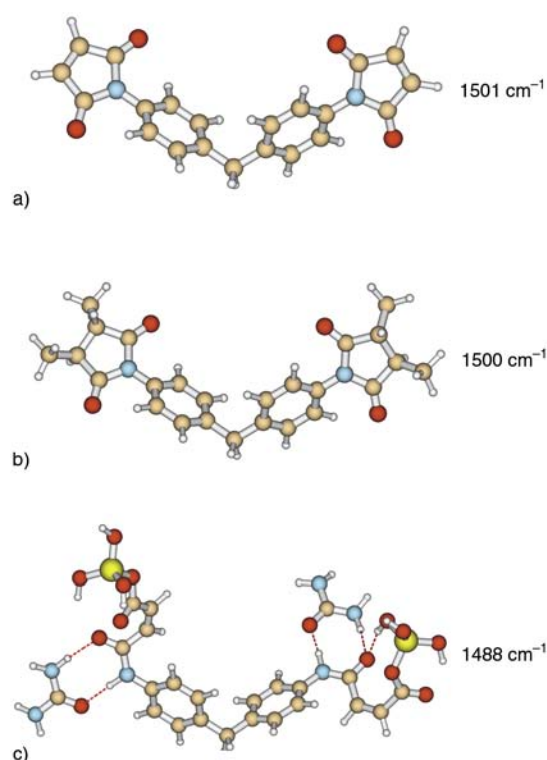


Figure 8. The DFT (B3LYP/6-31G(d)) optimized model structures and calculated frequencies a) imide ring, b) methyl groups added to the imide ring, c) opening of the imide ring

Table 5. Influence of the reactive modifier DBMI on the mechanical properties of the PP/untreated HNT and the PP/HEDA silane- and urea-modified HNT

Sample	Tensile strength [MPa]	Modulus [MPa]
Neat PP	36.3±0.4	1340±45
PP + 5 wt% untreated HNT	36.5±0.4	1440±84
PP + 5 wt% untreated HNT + 1 wt% DBMI	38.6±0.4	1510±55
PP + 5 wt% HNT modified HEDA	36.5±0.3	1548±35
PP + 5 wt% HNT modified HEDA + 1 wt% DBMI	38.3±0.4	1527±95
PP + 5 wt% HNT modified silane	35.6±0.2	1495±65
PP + 5 wt% HNT modified silane + 1 wt% DBMI	37.6±0.4	1580±45
PP + 5 wt% HNT modified urea	36.5±0.8	1449±31
PP + 5 wt% HNT modified urea + 1 wt% DBMI	40.0±0.5	1742±70

not reproduce the experimental vibrational frequencies exactly, the relative values of calculated frequencies are reliable and can be used for explanation of the observed frequency shifts. Figure 8b demonstrates that a very small frequency change occurs when methyl groups are added to the imide ring. This structure represents a direct reaction of the imide ring with PP, and thus, the band shift observed in Figure 7c cannot be explained by this direct reaction with PP. However, a significant shift in the band to lower wavenumbers (1488 cm^{-1}) was obtained for the model structure representing an opening of the imide ring for the case in which simultaneous hydrogen bonding of urea to the amide group is present (Figure 8c).

The coupling between PP and HNT was further confirmed by Soxhlet extraction in boiling xylene. While the remaining amounts of the PP/HNT and PP/BMI/HNT were approximately 2% (a portion of the HNT was missed due to ‘colloidal’ dimensions), the red-colored remainder in the PP/BMI/urea-intercalated HNT was 8%. The observed red color serves as further confirmation of the coupling reaction [29, 30].

From Table 2 (d-spacing values), it is evident that the increase in PP polarity by DBMI modification supports slightly the intercalation of PP chains into the PP structure. Furthermore, the linking between the PP and the HNT obviously do not support exfoliation. This was confirmed by TEM observation (Figure 6c, 6d), moreover, comparable degree of HNT dispersion was found for all composites studied.

4. Conclusions

The results obtained in this study indicate the low impact of single halloysite modifications using ionic exchange, silane condensation and urea intercalation on parameters of PP/nanocomposites. The most important effects of the modifiers applied include the effect on matrix crystallinity, specifically with respect to HEDA and urea. However, the simultaneous addition of DBMI to all PP/HNT systems resulted in increased mechanical properties due to *in situ* modification of the matrix, which increased the polarity of matrix and thus the affinity of the PP matrix for the HNT. Moreover, the combination of DBMI with urea-intercalated HNT led to the best

mechanical behavior due to coupling between the HNT and the PP via a facilitating reaction between the OH groups of the HNT and the imide ring of the DBMI by urea.

Acknowledgements

This work was supported by the Grant Agency of the Academy of Sciences of the Czech Republic (grant No IAA200500904). The financial support of the European Union and the European Social Fund in the frame of the TAMOP-4.2.2/B-10/1-2010-0025 project is also gratefully acknowledged.

References

- [1] Pinnavaia T. J., Beall G. W.: Polymer-clay nanocomposites. Wiley, London (2000).
- [2] Bhattacharya S. N., Gupta R. K., Kamal M. R.: Polymeric nanocomposites. Hanser, Munich (2008).
- [3] Pavlidou S., Papaspyrides C. D.: A review on polymer-layered silicate nanocomposites. Progress in Polymer Science, **33**, 1119–1198 (2008). DOI: [10.1016/j.progpolymsci.2008.07.008](https://doi.org/10.1016/j.progpolymsci.2008.07.008)
- [4] Du M., Guo B., Jia D.: Newly emerging applications of halloysite nanotubes: A review. Polymer International, **59**, 574–582 (2010). DOI: [10.1002/pi.2754](https://doi.org/10.1002/pi.2754)
- [5] Rawtani D., Agrawal Y. K.: Multifarious applications of halloysite nanotubes: A review. Reviews on Advanced Materials Science, **30**, 282–295 (2012).
- [6] Nicolini K. P., Fukamachi C. R. B., Wypych F., Mangrich A. S.: Dehydrated halloysite intercalated mechanochemically with urea: Thermal behavior and structural aspects. Journal of Colloid and Interface Science, **338**, 474–479 (2009). DOI: [10.1016/j.jcis.2009.06.058](https://doi.org/10.1016/j.jcis.2009.06.058)
- [7] Brindley G. W., Robinson K.: Randomness in the structures of kaolinitic clay minerals. Transactions of the Faraday Society, **42**, 198–205 (1946). DOI: [10.1039/TF946420B198](https://doi.org/10.1039/TF946420B198)
- [8] Joussein E., Petit S., Churchman J., Theng B., Righi D., Delvaux B.: Halloysite clay minerals – A review. Clay Minerals, **40**, 383–426 (2005). DOI: [10.1180/0009855054040180](https://doi.org/10.1180/0009855054040180)
- [9] Liu C., Luo Y., Jia Z., Li S., Guo B., Jia D.: Structure and properties of poly(vinyl chloride)/halloysite nanotubes nanocomposites. Journal of Macromolecular Science Part B: Physics, **51**, 968–981 (2012). DOI: [10.1080/00222348.2011.564106](https://doi.org/10.1080/00222348.2011.564106)
- [10] Liu C., Luo Y. F., Jia Z. X., Zhong B. C., Li S. Q., Guo B. C., Jia D. M.: Enhancement of mechanical properties of poly(vinyl chloride) with polymethyl methacrylate-grafted halloysite nanotube. Express Polymer Letters, **5**, 591–603 (2011). DOI: [10.3144/expresspolymlett.2011.58](https://doi.org/10.3144/expresspolymlett.2011.58)

- [11] Lecouvet B., Gutierrez J. G., Sclavons M., Bailly C.: Structure–property relationships in polyamide 12/halloysite nanotube nanocomposites. *Polymer Degradation and Stability*, **96**, 226–235 (2011). DOI: [10.1016/j.polymdegradstab.2010.11.006](https://doi.org/10.1016/j.polymdegradstab.2010.11.006)
- [12] Handge U. A., Hedicke-Höchstötter K., Altstädt V.: Composites of polyamide 6 and silicate nanotubes of the mineral halloysite: Influence of molecular weight on thermal, mechanical and rheological properties. *Polymer*, **51**, 2690–2699 (2010). DOI: [10.1016/j.polymer.2010.04.041](https://doi.org/10.1016/j.polymer.2010.04.041)
- [13] Liu M., Guo B., Du M., Lei Y., Jia D.: Natural inorganic nanotubes reinforced epoxy resin nanocomposites. *Journal of Polymer Research*, **15**, 205–212 (2008). DOI: [10.1007/s10965-007-9160-4](https://doi.org/10.1007/s10965-007-9160-4)
- [14] Barrientos-Ramírez S., de Oca-Ramírez G. M., Ramos-Fernández E. V., Sepúlveda-Escribano A., Pastor-Blas M. M., González-Montiel A.: Surface modification of natural halloysite clay nanotubes with aminosilanes. Application as catalyst supports in the atom transfer radical polymerization of methyl methacrylate. *Applied Catalysis A: General*, **406**, 22–33 (2011). DOI: [10.1016/j.apcata.2011.08.003](https://doi.org/10.1016/j.apcata.2011.08.003)
- [15] Du M., Guo B., Cai X. J., Jia Z., Liu M., Jia D.: Morphology and properties of halloysite nanotubes reinforced polypropylene nanocomposites. *e-Polymers*, no.130 (2008).
- [16] Lecouvet B., Sclavons M., Bourbigot S., Devaux J., Bailly C.: Water-assisted extrusion as a novel processing route to prepare polypropylene/halloysite nanotube nanocomposites: Structure and properties. *Polymer*, **52**, 4284–4295 (2011). DOI: [10.1016/j.polymer.2011.07.021](https://doi.org/10.1016/j.polymer.2011.07.021)
- [17] Du M., Guo B., Liu M., Jia D.: Thermal decomposition and oxidation ageing behaviour of polypropylene/halloysite nanotube nanocomposites. *Polymers and Polymer Composites*, **15**, 321–328 (2007).
- [18] Pasbakhsh P., Ismail H., Fauzi M. N. A., Abu Bakar A.: EPDM/modified halloysite nanocomposites. *Applied Clay Science*, **48**, 405–413 (2010). DOI: [10.1016/j.clay.2010.01.015](https://doi.org/10.1016/j.clay.2010.01.015)
- [19] Prashantha K., Lacrampe M. F., Krawczak P.: Processing and characterization of halloysite nanotubes filled polypropylene nanocomposites based on a masterbatch route: Effect of halloysites treatment on structural and mechanical properties. *Express Polymer Letters*, **5**, 295–307 (2011). DOI: [10.3144/expresspolymlett.2011.30](https://doi.org/10.3144/expresspolymlett.2011.30)
- [20] Jia Z., Luo Y., Guo B., Yang B., Du M., Jia D.: Reinforcing and flame-retardant effects of halloysite nanotubes on LLDPE. *Polymer-Plastics Technology and Engineering*, **48**, 607–613 (2009). DOI: [10.1080/03602550902824440](https://doi.org/10.1080/03602550902824440)
- [21] Liu M., Jia Z., Liu F., Jia D., Guo B.: Tailoring the wettability of polypropylene surfaces with halloysite nanotubes. *Journal of Colloid and Interface Science*, **350**, 186–193 (2010). DOI: [10.1016/j.jcis.2010.06.047](https://doi.org/10.1016/j.jcis.2010.06.047)
- [22] Du M., Guo B., Jia D.: Thermal stability and flame retardant effects of halloysite nanotubes on poly(propylene). *European Polymer Journal*, **42**, 1362–1369 (2006). DOI: [10.1016/j.eurpolymj.2005.12.006](https://doi.org/10.1016/j.eurpolymj.2005.12.006)
- [23] Liu M., Guo B., Lei Y., Du M., Jia D.: Benzothiazole sulfide compatibilized polypropylene/halloysite nanotubes composites. *Applied Surface Science*, **255**, 4961–4969 (2009). DOI: [10.1016/j.apsusc.2008.12.044](https://doi.org/10.1016/j.apsusc.2008.12.044)
- [24] Liu M., Guo B., Du M., Jia D.: The role of interactions between halloysite nanotubes and 2,2'-(1,2-ethenediylid-4,1-phenylene) bisbenzoxazole in halloysite reinforced polypropylene composites. *Polymer Journal*, **40**, 1087–1093 (2008). DOI: [10.1295/polymj.PJ2008133](https://doi.org/10.1295/polymj.PJ2008133)
- [25] Liu M., Guo B., Du M., Zou Q., Jia D.: Influence of hybrid fibrils of 2,5-bis(2-benzoxazolyl) thiophene and halloysite nanotubes on the crystallization behaviour of polypropylene. *Journal of Physics D: Applied Physics*, **42**, 075306/1–075306/9 (2009). DOI: [10.1088/0022-3727/42/7/075306](https://doi.org/10.1088/0022-3727/42/7/075306)
- [26] Ning N-Y., Yin Q-J., Luo F., Zhang Q., Du R., Fu Q.: Crystallization behavior and mechanical properties of polypropylene/halloysite composites. *Polymer*, **48**, 7374–7384 (2007). DOI: [10.1016/j.polymer.2007.10.005](https://doi.org/10.1016/j.polymer.2007.10.005)
- [27] Khunová V., Kelnar I., Liauw C. M., Lukác P.: The effect of interfacial modification on the properties of reactively processed polypropylene/clay nanocomposites. *Composite Interfaces*, **18**, 357–370 (2011). DOI: [10.1163/092764411X584496](https://doi.org/10.1163/092764411X584496)
- [28] Khunová V., Liauw C. M., Kelnar I., Snauko M.: Elimination of separation processes for post-consumer polyolefin waste: Reactive blending using 1,3-phenylene dimaleimide in presence of filler. *Macromolecular Materials and Engineering*, **294**, 502–509 (2009). DOI: [10.1002/mame.200900025](https://doi.org/10.1002/mame.200900025)
- [29] Liauw C. M., Khunová V., Lees G. C., Rother R. N.: Reactively processed high performance impact modified polypropylene/magnesium hydroxide composites: Interfacial studies. *Macromolecular Symposia*, **194**, 191–200 (2003). DOI: [10.1002/masy.200390082](https://doi.org/10.1002/masy.200390082)
- [30] Khunová V., Liauw C. M.: Tailoring of interphase structure in highly filled poly(propene) block copolymer via reactive processing. *Polymer Bulletin*, **47**, 465–473 (2002). DOI: [10.1007/s002890200010](https://doi.org/10.1007/s002890200010)
- [31] Irikura K. K., Johnson R. D. III, Kacker R. N.: Uncertainties in scaling factors for ab initio vibrational frequencies. *Journal of Physical Chemistry A*, **109**, 8430–8437 (2005). DOI: [10.1021/jp052793n](https://doi.org/10.1021/jp052793n)

Nano-lignin filled natural rubber composites: Preparation and characterization

C. Jiang, H. He*, H. Jiang, L. Ma, D. M. Jia

Department of Polymer Materials and Engineering, South China University of Technology, 510640 Guangzhou, China

Received 24 December 2012; accepted in revised form 10 February 2013

Abstract. This paper presents a novel strategy to prepare nano-lignin and its composites with natural rubber. The nano-lignin was obtained by fabricating colloidal lignin-Poly (diallyldimethylammonium chloride) (PDADMAC) complexes (LPCs) via self-assembly technology. The characteristics of LPCs were investigated by zeta potential, dynamic light scattering (DLS), transmission electron microscopy (TEM), Fourier transform infrared spectroscopy (FTIR) and ultraviolet – visible (UV-vis) absorption measurements. The results indicated that PDADMAC intensively interacted with lignin by cation- π and π - π interactions, and lignin particles were stable in aqueous solution with an average particle size less than 100 nm. LPCs accelerated the vulcanization of NR/LPCs nanocomposites. Morphological studies and Dynamic mechanical analysis (DMA) showed the homogeneous dispersion of LPCs in the NR matrix and the strong interfacial adhesion between them. The nanoscale dispersion of LPCs significantly enhanced the thermal stability and mechanical properties of NR/LPCs nanocomposites.

Keywords: nanocomposites, natural rubber, nano-lignin, cationic polyelectrolyte, self-assembly

1. Introduction

Lignin, the second most abundant renewable natural resource next to cellulose, is a highly-branched, three dimensional biopolymer. It consists of three phenylpropanoid units, such as *p*-hydroxyphenyl (H), guaiacyl (G) and syringyl (S) (Figure 1), which are attached to one another by a series of characteristic linkages (β -O-4, β -5, β - β , etc.) [1]. The major chemical functional groups in lignin include hydroxyl, methoxyl, carbonyl and carboxyl groups in various amounts and proportions, depending on genetic origin and applied extraction processes [2]. The distinct network structure as well as the presence of the various chemical substituents confers special functional properties to lignin, such as stabilizing effect [3], reinforcing effect, UV-absorption, biodegradability, anti-fungal and antibiotic activity [4–6]. However, the potential of lignin is not clearly

valued, because it predominantly obtained as by-products in pulp production is mainly used as fuel. Fortunately, incorporating into polymeric materials will be a value-added application for lignin [7–10]. Especially in rubber-based materials, lignin is less dense, non-conducting, and being lighter in color compared to carbon black. It appears more amenable for the preparation of light-colored rubber compounds. So, for the past decades great amounts of researches [11–13] and patents [14–18] of lignin as filler added to rubber compounds have investigated carbon black replacement in order to achieve similar reinforcement of rubber composites. Usually, two strategies (dry-milling and co-precipitation) are mostly used for the preparation of lignin-filled rubber composites. Lignin as dry powder straightforward milled into rubber shows almost no reinforcing effect. This is believed to be a result of the

*Corresponding author, e-mail: pshuihe@scut.edu.cn
© BME-PT

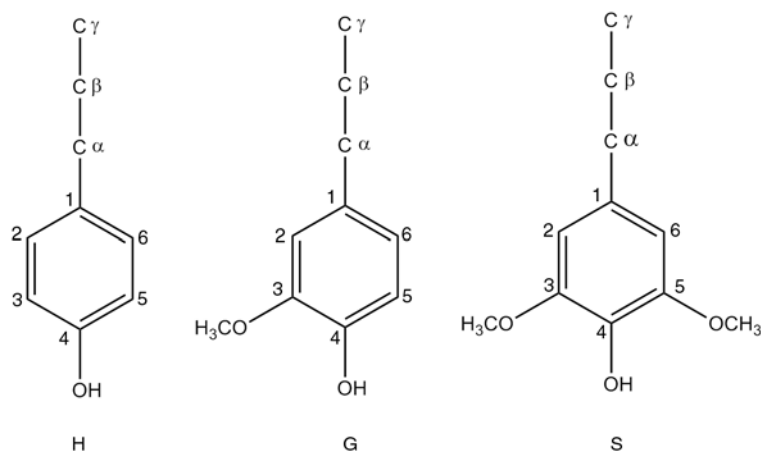


Figure 1. Three phenylpropanoid units of lignin

lignin particles adhering together by intermolecular hydrogen bonding and thus not being dispersed into the rubber by milling [19]. It is a unique property that lignin is soluble in aqueous alkali because of the ionization of the phenolic hydroxyl and carboxylic groups, such solutions being compatible with rubber latex in all proportions. Furthermore, the co-precipitation of the lignin and the rubber from the mixing solution with acids is possible in the same pH range [20]. In comparison to dry-milling method, the distribution of the lignin in the rubber compounds prepared by co-precipitation method is more homogeneous and the particle size is finer. Even so, the lignin is still unable to be dispersed at nanoscale. Nevertheless, the reinforcing effect of lignin for rubber compounds intensively depends on particle size and strong interfacial bonding with rubber matrix. In most reports, the lignin shows little reinforcing effect on nonpolar rubber matrix and even deteriorates the performance of rubber composites [21, 22]. To the best of our knowledge, there is no report on nanoscale lignin reinforced natural rubber. Therefore, we highlight the fabrication of nano-lignin and the nanoscale distribution of lignin in rubber matrix by a novel strategy in this paper.

Lignin can be viewed as an anionic polyelectrolyte when phenolic hydroxyls and carboxylic groups are ionized. Usually, three types of polyelectrolyte complexes can form: soluble, colloidal and coacervate [23]. In previous publications, the studies on the formation of polyelectrolyte complexes between cationic polyelectrolytes and anionic lignin aim to improve wastewater-treatment efficiency [24, 25], increase the efficiency of retention aids and enhance the strength of papers in papermaking [26]. As a consequence, the lignin-cationic polyelectrolyte com-

plexes are commonly coacervates for those purposes. However, the complexes must be colloidal to mix with natural rubber latex (NRL) and produce NR/lignin nanocomposites. In the present work, the formation and characteristics of colloidal LPCs were investigated and the adsorption mechanism of PDADMAC onto the lignin surface was discussed. The morphology of the NR/lignin composites was also observed by SEM. The mechanical performance and vulcanization behaviors were studied, as well as the thermal and thermo-oxidative stability.

2. Experimental section

2.1. Materials

Lignin was industrial sulfate lignin (micron scale), purchased from Shandong Tralin Pape Co., Ltd., China. The average molecular weight of sulfate lignin was 3801 with the polydispersity index of 2.15. PDADMAC (100 000–200 000; 20 wt% in water) was obtained from Sigma-Aldrich (Sigma-Aldrich, Louis, MO). NRL stabilized by ammonia with a total solid content of 64.5% was provided by the Tropical Crops Research Center of Zhanjiang, China. Sodium hydroxide, hydrochloric acid and sulfuric acid were analytical grade, purchased from Guangzhou Chemical Reagent Factory, China. The reagents used in rubber formula such as sulphur, stearic acid, zinc oxide, N-tert-butyl-2-benzothiazole sulfonamide (CBS), were industrial grade, kindly provided by South China Rubber Tyre co., Ltd.

2.2. Purification of the industrial sulfate lignin

The industrial sulfate lignin was dissolved in a beaker with deionized water followed by adding NaOH to adjust the pH to approximately 13. The

resulting solution was centrifuged to exclude fibril or insoluble impurities before slowly titrating with 1.0 N sulfuric acid to a final pH of approximately 2 with mechanical stirring. Subsequently, the slurry was placed in water bath at 70°C for 2 h to accelerate lignin agglomeration then filtered. The lignin was washed with deionized water three times and dried in a vacuum oven at 50°C for 24 h followed by extraction with pentane to remove the organic impurities. Finally, the purified lignin was dried at 50°C and stored under reduced pressure.

2.3. Preparation of sample solution

Purified sulfate lignin was dissolved in deionized water at a mass concentration of 0.5% and the pH was adjusted to 12. PDADMAC aqueous solution was diluted to 2 wt % with deionized water followed by adjusting the pH to 12. The various mass of sulfate lignin solution was dropped slowly into the PDADMAC solution with vigorous stirring, leading to formation of colloidal LPCs with different mass ratios of lignin to PDADMAC.

2.4. Preparation of NR/lignin compounds

The NRL was diluted to a solid content of 10% and its pH was adjusted to 12 with 1 N NaOH. After that, a desired amount of the lignin solution or the colloidal LPCs solution was then dropped into NRL under vigorous mechanical stirring. The resulting solution was co-precipitated by adjusting the pH to 2 with 1 N sulfuric acid. Finally, the obtained mixtures were filtered, water washed and dried in a vacuum oven at 50°C.

All the rubber compositions were summarized in Table 1. The dried composites and other additives were mixed on an open two-roll mill. Then the compounds were vulcanized in a standard mold at 143±1°C for optimum vulcanization time, which was determined by the U-CAN UR-2030 vulcameter (Taipei, Taiwan).

2.5. Characterizations

The particle size of lignin and colloidal LPCs as a function of solution pH was determined by DLS using a N5 Submicron Particle Size Analyzer (Beckman Coulter) with a detection angle of 90° at 25°C. The effect of mass ratio of lignin to PDADMAC on the particle size of LPCs was also studied by DLS. All samples were repeatedly measured three times. The zeta potential measurements were carried out on Malvern Zetasizer Nano ZS90.

The UV-vis absorption measurements were performed with a UV-vis spectrophotometer (UV756CRT, Shanghai Youke Instrument CO. Ltd., China). Deionized water was scanned at the same wavelength as a baseline.

The sample solutions of lignin or LPCs were diluted with 0.01 N NaOH to a certain mass concentration of 0.05% (based on lignin) for DLS and zeta potential measurements or 0.01% for UV-vis absorption measurements. A few drops of either 0.1 N, 0.01 N or 0.001 N HCl was added to the diluted sample solutions to adjust the pH before the measurements. The samples for TEM measurement were prepared by dropping sample solution on Cu grids of 200 mesh and then observed on a Hitachi H-7650 instrument (Hitachi, Japan) with an accelerating voltage of 80 kV.

FTIR was recorded in transmission mode with a Bruker Vertex 70 FTIR spectrometer at a spectral resolution of 4 cm⁻¹ and 32 scans. Then KBr pellets of lignin, PDADMAC and LPCs were prepared (200 mg KBr : 1–2 mg sample) with pressure.

Scanning electron micrographs (SEM) of the composites were taken with a Nova NanoSEM 430 instrument (FEI, Netherlands) at an acceleration voltage of 10 kV. The fracture surface was obtained by splitting bulk sample being quenched in liquid nitrogen. Before the observation, a thin gold was evaporated on the fractured surface.

Table 1. Recipe of NR/lignin compounds^a

Ingredients [phr] ^b	Sample code								
	L-0	L-1	L-3	L-5	L-7	LPCs-1	LPCs-3	LPCs-5	LPCs-7
NR	100	100	100	100	100	100	100	100	100
Lignin	0	1	3	5	7	0	0	0	0
LPCs ^c	0	0	0	0	0	1	3	5	7

^arubber ingredients: ZnO 5, Stearic acid 2, CBS 2, S 2.

^bphr, parts per hundred of rubber by weight.

^cthe ratio of lignin to PDADMAC is 0.45, and the amount of LPCs in the formula refers to the weight of lignin in the LPCs.

The curing characteristics of the compounds were determined at 143°C by U-CAN UR-2030 vulcameter. After the compounds were vulcanized for vulcanization time (T_{c90}) at 143±1°C, tensile and tear tests of the vulcanizates were performed according to ISO 37-2005 and ISO 34-2004, respectively. The crosslink density of the vulcanizates was measured according to the method described by Gregorová *et al.* [27].

DMA spectra of the samples were obtained by using a DMA 242D dynamic mechanical analyzer (NETZSCH Company, Germany). The specimens with the size of 30 mm × 6 mm × 4 mm were analyzed in tensile mode at a constant frequency of 1 Hz, a strain of 0.5%, and a temperature range from –130 to 50°C at a heating rate of 3°C/min.

A Perkin–Elmer Pyris 1 TGA thermogravimetric analyser (TGA) (Perkin-Elmer, Fremont, USA) was used for thermal and thermo-oxidative stability measurement. In nitrogen, the measurement was carried out from room temperature to 700°C at a heating rate of 10°C/min. In air, the TGA analysis was carried out at the same temperature range and heating rate. The flow rate of the carrying was 20 mL/min.

3. Results and discussion

3.1. Effect of pH on the particle size of lignin

The aggregation and hydrodynamic radius of colloidal lignin in aqueous solution can be influenced by many factors, such as pH [28, 29], temperature [30], electrolyte [31, 32], concentration of lignin [33] and surfactant [34]. Due to the ionizable phenolic hydroxyls and carboxylic groups in lignin macromolecules, the association and particle size of lignin are very sensitive to the solution pH. Figure 2 shows the effect of the solution pH on the particle

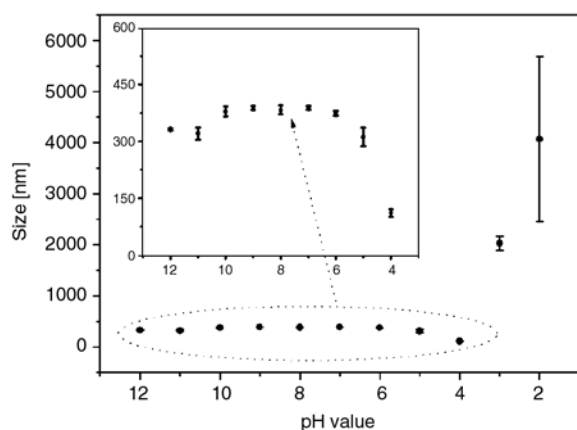


Figure 2. The effect of the solution pH on the particle size of lignin

size of lignin. As the pK_a of the phenolic hydroxyls on lignin is higher than 10.2 [35], they are not ionized when the pH is below 10. But lignin still has negative charges at alkaline and neutral pH that can be attributed to the ionized carboxylic groups. Therefore, the lignin is still stable at that pH range from 10 to 7. At acidic pH, the degree of dissociation of carboxylic groups decreases with decreasing pH. Consequently, lignin macromolecules shrink at the pH range from 6 to 4 (i.e., from about 380 to about 110 nm). When the pH is low enough and carboxylic groups are completely protonated, the serious aggregation of lignin particles is unavoidable. It can be attributed that the attractive forces including hydrophobic interactions, hydrogen bonding interactions [28] and π - π interactions [36–39] surpass the electrostatic repulsive forces. Conceivably, the lignin particles will aggregate and form agglomerates in rubber matrix, when the NRL and lignin is co-precipitated by adding acid.

3.2. Characteristics of colloidal LPCs

It is generally known that oppositely charged polyelectrolytes form complexes over a broad range of stoichiometric ratios and that the complexes tend to be water-soluble unless they are nearly stoichiometric [23]. In this work, the colloidal LPCs were fabricated by dropwise adding the alkali solution of lignin into the PDADMAC solution. Hence, the formed LPCs were positively charged and water-soluble until the mass ratio of lignin to PDADMAC exceeded stoichiometric point. However, the NRL particles were natively charged at the pH of 12, as the protein molecules absorbed on the surface of NRL particles contained carboxylic and amino groups and the carboxylic groups would be ionized at that pH. When the LPCs solution were added into NRL, the natively charged NRL were subsequently adsorbed onto the positively charged LPCs via electrostatic self-assembly, which would suppress the aggregation of lignin and finally resulted in homogeneous distribution of lignin in NR matrix (see Figure 3). However, excess PDADMAC adsorbed onto lignin is unnecessary. If present in excess, it will prematurely flocculate NRL and reduce the loading of lignin incorporated into rubber matrix. To optimize the fabrication of LPCs, the effect of mass ratio of lignin to PDADMAC on particle size of LPCs was investigated (Figure 4). The particle size of LPCs is consistently reduced (from about 400 to about 180 nm) with the increas-

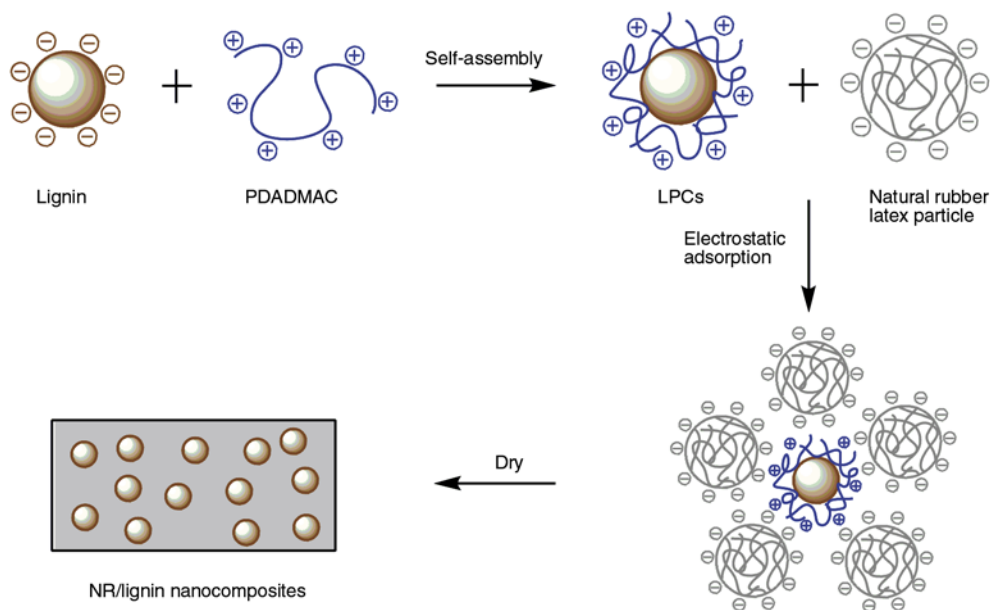


Figure 3. Schematic illustration of process for NR/Lignin nanocomposites

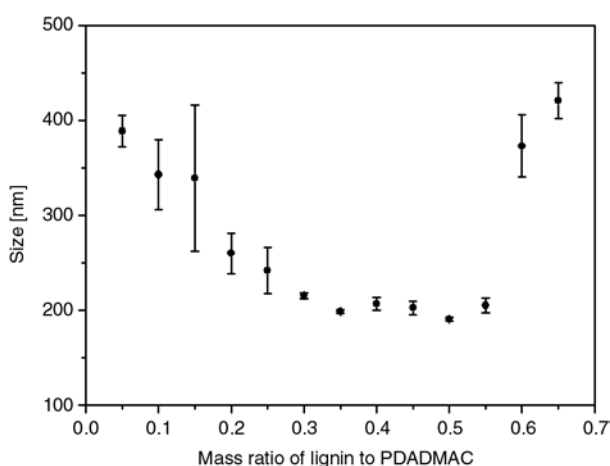


Figure 4. The effect of mass ratio of lignin to PDADMAC on particle size of LPCs at pH of 12

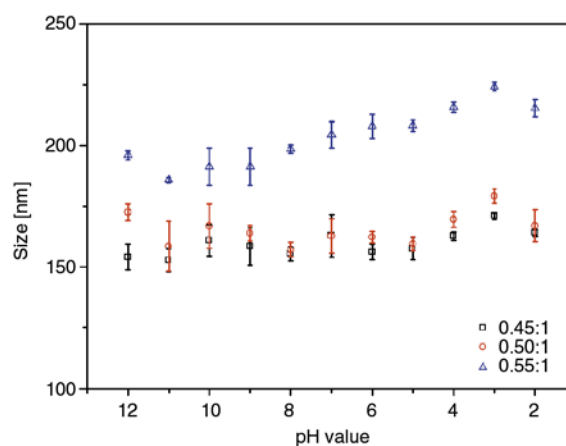


Figure 5. The particle size of colloidal LPCs with different mass ratios of lignin to PDADMAC as a function of solution pH

ing lignin/PDADMAC ratio (from 0.05 to 0.5). It should be noted that the minimum particle size of LPCs is still larger than that of the collapsed lignin at the pH 4 (about 110 nm). The particle size should be the size of collapsed lignin plus the thickness of absorption layer of PDADMAC onto lignin surface. A significantly increasing particle size follows when lignin and positively charged LPCs are present. Similarly, the particle size of colloidal LPCs as a function of solution pH was investigated (Figure 5). It can be seen that the particle size of colloidal LPCs with lignin/PDADMAC ratios of 0.45 and 0.5 is very close and stable at the pH range from 12 to 2. It is quite different from the results in Figure 2. Hence, the lignin can be dispersed at nanoscale in NR matrix when acid is used to co-precipitate rub-

ber latex and LPCs. In the case of colloidal LPCs with a lignin/PDADMAC ratio of 0.55, a slightly increasing particle size with decreasing pH indicates the association of LPCs. Furthermore, the original particle size of colloidal LPCs with a lignin/PDADMAC ratio of 0.55 is larger than that of two others, indicating the partial association of LPCs at the beginning of formation of colloidal LPCs. In fact, the results from DLS measurements are apparent hydrodynamic diameters, obtained from the measured diffusion coefficients using the Stokes-Einstein relationship. The particle size from DLS is always larger than actual size [40], especially in colloidal LPCs system. Adsorbed PDADMAC will significantly increase the hydrodynamic diameter of

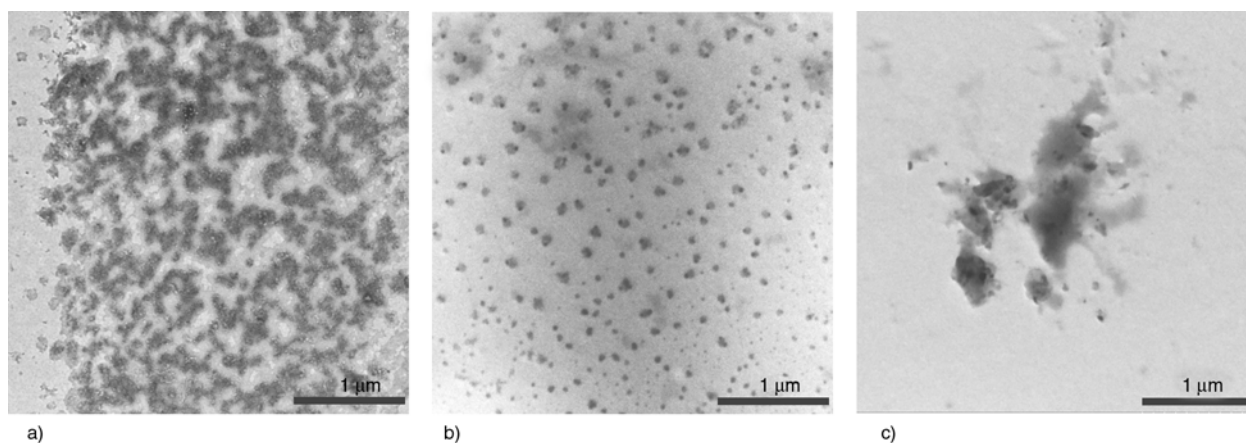


Figure 6. TEM photos of lignin (a), LPCs with a lignin/PDADMAC ratio of 0.5 (b) and LPCs with a lignin/PDADMAC ratio of 0.6 (c)

lignin because of the length of PDADMAC molecular chain. In a polydisperse system, results from DLS measurements give more or less the diameters of the largest aggregates, and not a weight average or size average [34]. To assess the actual size of lignin and LPCs, their TEM photos are shown in Figure 6. It can be seen that serious aggregation and amorphous profile are present in the sample of lignin (Figure 6a). Relatively, LPCs with a mass ratio of 0.5 are stable and individually dispersed with an average size 60.8 nm, which was calculated by Nano Measurer (Figure 6b). However, LPCs become larger as the lignin/PDADMAC ratio rises to 0.6 (Figure 6c), which is similar to the results from DLS. It should be attributed to the bridging flocculation of lignin and PDADMAC. Hence, the lignin/PDADMAC ratio should be less than 0.55 to fabricate nanoscale and stable lignin.

The zeta potential of colloidal LPCs was measured in this work in order to study the charge state of colloidal LPCs surface (Figure 7). The zeta potential of lignin in aqueous alkali had been measured (−22.3 mV; pH = 12). Due to the adsorption of positively charged PDADMAC onto lignin surface, there were excess positive charges on the surface of colloidal LPCs. With increasing the lignin/PDADMAC ratio, the zeta potential of colloidal LPCs monotonically decreases, which indicates that charge density on the LPCs surface gradually decreases with increasing lignin/PDADMAC ratio. However, the charge on LPCs surface is still positive, when the lignin/PDADMAC ratio is less than 0.55. Therefore, positively charged LPCs can adsorb negatively charged natural rubber latex in latex compounding proce-

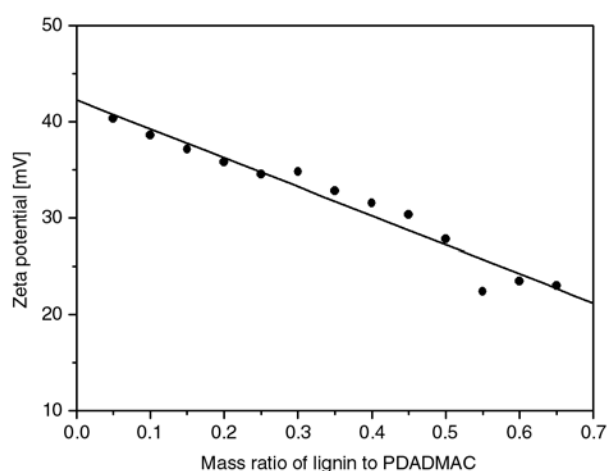


Figure 7. The zeta potential of LPCs as a function of mass ratio of lignin to PDADMAC at pH of 12

cedure, which will further suppress the association of lignin.

The UV-vis absorption spectra of colloidal LPCs as a function of solution pH offer a powerful proof to further clarify the adsorption mechanism of PDADMAC to lignin. As shown in Figure 8a, the absorption bands located at 240 and 288 nm are assigned to K and B bands of $\pi-\pi^*$ transitions of the aromatic rings in lignin linked by ionized phenolic hydroxyls and carboxylic groups. Obviously, the K band disappears and the B band shifts to 276 nm with decreased absorption intensity as the solution pH changes from 12 to 7, which is the result of protonation of phenolic hydroxyls. Herein, the UV-vis spectrum of lignin at acidic pH is not shown due to the solubility of lignin. For LPCs, the similar tendency is found in Figure 8b. Considering the dissociation constant of phenolic hydroxyls, the decreased intensity from

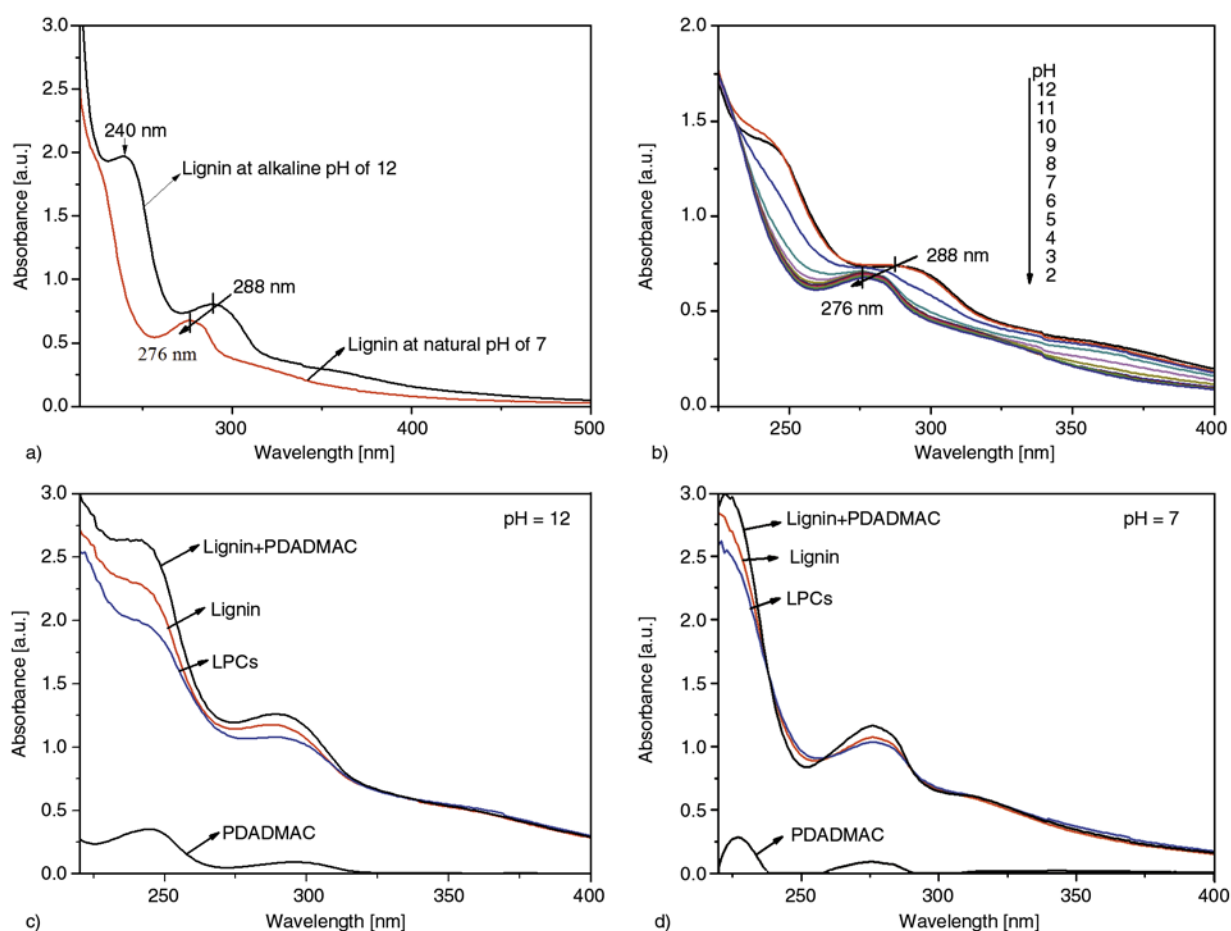


Figure 8. (a) The UV-vis absorption spectra of lignin as functions of solution pH; (b) the UV-vis absorption spectra of LPCs as functions of solution pH; (c) the UV-vis absorption spectra of LPCs (0.05 g/L lignin, 0.11 g/L PDADMAC), lignin (0.05 g/L) and PDADMAC (0.11 g/L) at pH of 12; (d) the UV-vis absorption spectra of LPCs (0.05 g/L lignin, 0.11 g/L PDADMAC), lignin (0.05 g/L) and PDADMAC (0.11 g/L) at pH of 7. Note that the curves of lignin + PDADMAC are the superposed spectra of lignin and PDADMAC.

pH 10 to 7 may be ascribed to a hysteresis of protonation of phenolic hydroxyls. Unlike phenolic hydroxyls, carboxylic groups have less influence on the ultraviolet light absorption of lignin. So, no decreased intensity was observed at acidic pH. However, the protonation of carboxylic groups is possible at acidic pH since phenolic hydroxyls can be protonated. The hypochromic effect of colloidal LPCs with decreasing pH indicates that H ions can penetrate through the adsorption layer of PDADMAC and combine with ionized functional groups. In other words, the ionized functional groups do not form short-distance ion pairs with PDADMAC. This result is coincided with others' work [24]. However, the colloidal LPCs could be stabilized by PDADMAC at acidic pH, indicating other interactions between lignin and PDADMAC except ion-ion interactions. Figure 8c and 8d show the UV-vis spectra of LPCs, as well as the spectra of its corresponding components, such as lignin and PDADMAC, respectively at

pH of 12 and 7. The superposed spectra of lignin and PDADMAC are also shown for comparison with LPCs. The obvious differences in the maximum absorption and the shape between the spectra of LPCs and the superposed spectra indicate the strong interactions between lignin and PDADMAC. It should be attributed to cation- π interactions, widely reported between benzene rings and polycations [41, 42], which can result in charge-transfer from the aromatic rings in lignin to PDADMAC.

For the driving forces of adsorption of PDADMAC onto lignin, Pillai and Rennekar [43] considered that cation- π interactions as driving forces contribute to the adsorption besides ion-ion interactions. In this work, another noncovalent interaction, π - π interaction between an unsaturated contaminant in the PDADMAC chain (Figure 9a) and lignin, was revealed by FTIR (Figure 9b). The peaks at 1636 and 1474 cm^{-1} in PDADMAC, corresponding to the stretching of the double bonds in the contaminant,

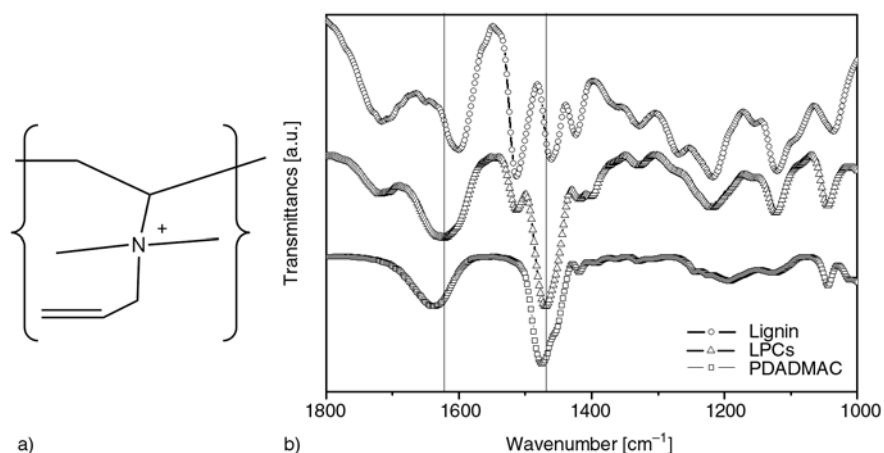


Figure 9. Chemical structure of the contaminate in PDADMAC (a) and FTIR spectra of lignin, LPCs and PDADMAC (b)

respectively shift to 1623 and 1470 cm^{-1} in LPCs, which are also different from the peaks at 1600 and 1460 cm^{-1} in lignin. The shifts indicate that the double bonds both in the contaminant and lignin are in a different environment. Because of a great amount of aromatic units in lignin interacting with each other via π - π interactions, similarly, the double bond in the contaminant can also stack with the aromatic rings in lignin. The similar result was also observed by Yang *et al.* [44] in the system of PDADMAC/Multiwalled Carbon Nanotubes.

The additional driving forces, π - π interactions, enhance the adhesion of PDADMAC on lignin surface. Furthermore, the molecule chain skeleton of PDADMAC is similar to that of NR, which suggests a good compatibility between PDADMAC and NR. Therefore, the interfacial bonding between lignin and NR matrix in NR/LPCs composites is better than that in NR/lignin composites.

3.3. Morphology of NR/lignin and NR/LPCs composites

Lignin dispersion in the NR matrix was studied by SEM observation. As shown in Figure 10a, the agglomerate with a large size about 2000 nm is present in NR matrix. This indicates that the aggregation of lignin is unavoidable by co-precipitation method, although a part of lignin is dispersed in nanoscale due to the polydispersity of lignin. In contrast, it is clear to see that the lignin is uniformly dispersed in nanoscale in Figure 10a–10e. And the average particle size of LPCs calculated by Nano Measurer is about 90–100 nm. The obvious differences in the two samples clarify that cationic PDADMAC polyelectrolytes can stabilize colloidal

lignin particles and suppress aggregation when lignin is co-precipitated with NRL.

3.4. Curing characteristics and crosslink density

The curing characteristics of the pristine NR and its composites with lignin or LPCs, expressed in terms of the vulcanization times, t_{S2} (scorch time) and t_{90} (optimum cure time), as well as the maximum and minimum values of the torque, S_{\max} and S_{\min} , respectively, and delta torque ΔS ($\Delta S = S_{\max} - S_{\min}$), were deduced from curing curves. These parameters, along with the cure rate index, CRI expressed as $\text{CRI} = 100/(t_{90} - t_{S2})$, were compiled as shown in Table 2, as well as the crosslink density of composites.

It is obvious that incorporation of lignin or LPCs into NR matrix has distinctly different effects on the curing characteristics of composites. For NR/lignin composites, the scorch time gradually decreases with addition of lignin while the optimum cure time increases slightly. According to the gradually decreased CRI of NR/lignin compounds, we can infer that lignin hinders vulcanization. It can be attributed to the fact that phenolic hydroxyl of lignin not only acts as an activating agent to reduce scorch time, but also reacts with curing system to increase optimum cure time because of its acidity [13, 45], which results in a gradually decreased crosslink density of NR/lignin composites with the addition of lignin. For NR/LPCs compounds, both vulcanization times, t_{S2} and t_{90} , are sharply reduced with addition of LPCs, showing accelerated vulcanization with respect to that of pure NR and NR/lignin compounds. These results are confirmed by CRI and the crosslink density data, which show a significant

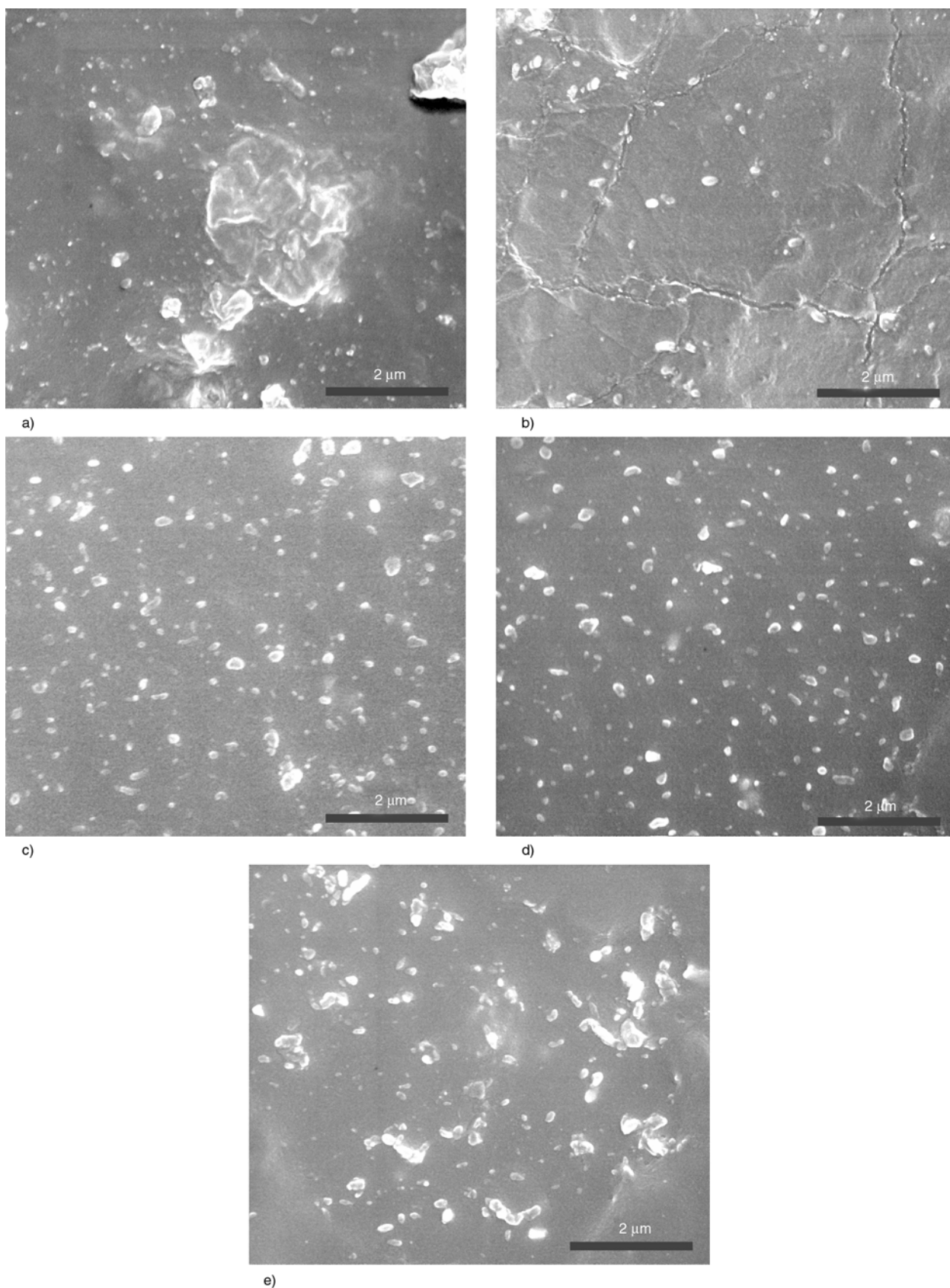


Figure 10. SEM photos of NR/lignin composites and NR/LPCs nanocomposites. (a) L-7; (b) LPCs-1; (c) LPCs-3; (d) LPCs-5; (e) LPCs-7.

increase with increasing LPCs loading, mainly attributed to the accelerating effect provided by the

PDADMAC in LPCs [46, 47]. On the other hand, the minimum torque, maximum torque and delta torque

Table 2. Curing characteristics and crosslink density of pure NR and its composites with lignin and LPCs

Sample code	S_{min} [dNm]	S_{max} [dNm]	ΔS [dNm]	t_{s2} [min]	t_{90} [min]	CRI [min ⁻¹]	Crosslink density [10 ⁻⁵ mol/cm ³]
L-0	0.09	10.58	10.49	19.55	31.45	8.40	6.65
L-1	0.17	11.90	11.73	18.56	32.40	7.23	6.57
L-3	0.15	11.70	11.55	18.16	32.54	6.95	5.47
L-5	0.16	11.31	11.15	17.34	32.15	6.75	5.25
L-7	0.19	12.42	12.23	17.20	33.15	6.27	5.13
LPCs-1	0.19	12.24	12.05	15.49	27.24	8.51	6.57
LPCs-3	0.25	12.68	12.43	10.17	18.52	11.98	6.63
LPCs-5	0.20	12.89	12.69	9.56	17.44	12.69	7.05
LPCs-7	0.35	14.50	14.15	8.20	15.33	14.03	7.21

Table 3. Mechanical properties of pure NR and its composites with lignin and LPCs

Sample code	Modulus at 300% [MPa]	Tensile strength [MPa]	Elongation at break [%]	Tear strength [kN/m]	Hardness [Shore A]
L-0	2.00±0.03	25.24±0.38	654±13	27.70±1.02	38
L-1	2.14±0.16	25.07±1.22	679±16	24.79±1.14	36
L-3	1.96±0.00	23.91±0.58	701±13	23.50±1.28	37
L-5	2.13±0.03	23.38±1.18	675±13	22.11±0.89	38
L-7	2.17±0.07	23.81±0.38	693±4	22.08±0.17	39
LPCs-1	1.96±0.01	25.69±1.30	701±5	27.35±0.43	38
LPCs-3	2.25±0.09	27.51±0.45	715±14	30.00±0.13	40
LPCs-5	2.38±0.00	27.91±0.46	725±10	28.12±1.05	41
LPCs-7	2.95±0.10	29.24±0.59	658±20	34.74±1.28	44

increase by addition of lignin or LPCs. It is of interest to point out that this increase is more evident for NR/LPCs composites, due to the higher crosslinking density of NR/LPCs composites.

3.5. Mechanical property and dynamic mechanical property

The mechanical properties of the pure NR and its composites with lignin or LPCs are listed in Table 3. Compared to pure NR, gradually decreased tensile strength and tear strength with addition of lignin can be observed in NR/lignin composites due to the bad interfacial compatibility between polar lignin and nonpolar NR, whereas a noticeable improvement in tensile strength, tear strength and the modulus at 300% is achieved with increasing LPCs loading in NR/LPCs composites. This distinction can be attributed to the two factors: lignin dispersion and affinity between rubber matrix and lignin. Lignin is well-dispersed in NR/LPCs composites and aggregates in NR/lignin composites, which has been disclosed by SEM. Moreover, LPCs has higher affinity toward NR matrix than lignin, due to the similarity between the chain backbones of PDADMAC on LPCs surface and natural rubber. Interestingly, the

hardness of NR/lignin composites shows practically no variation, whereas that of NR/LPCs composites mildly increases with addition of LPCs. The increased hardness may be ascribed to the presence of PDADMAC.

The dynamic mechanical properties of NR/LPCs composites and NR/lignin composites were also performed. The variation of tangent delta ($\tan \delta$) and storage modulus (E') as a function of temperature as a comparison are reported in Figure 11. The $\tan \delta$ peak height is 1.58 and 1.64 respectively for NR/LPCs composites and NR/lignin composites. Furthermore, the glass transition temperature of NR/LPCs composites is -88°C , which is 5°C higher than that of NR/lignin composites. These results suggest that there is a stronger interaction between LPCs and NR matrix. This interaction restricts the mobility of the elastomer segments, which significantly elevates the glass transition temperature. The E' of NR/LPCs composites shows a higher value than that of NR/lignin composites below the glass transition temperature, which demonstrates that the addition of LPCs into NR matrix results in an increase of stiffness. That further reflects the stronger confinement of LPCs on the rubber chains.

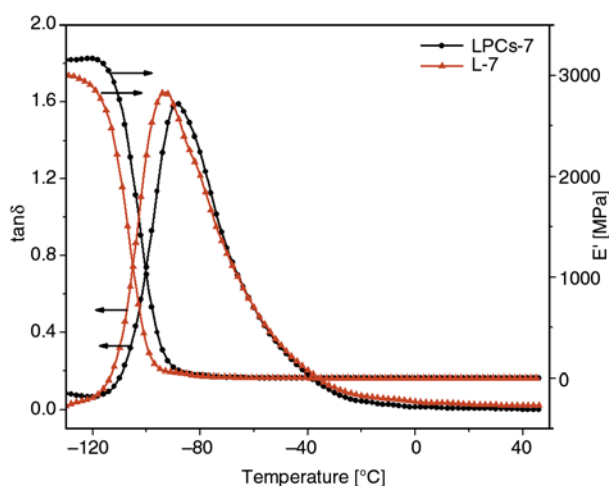


Figure 11. The curves of tangent delta and storage modulus versus the temperature for NR/lignin (L-7) and NR/LPCs (LPCs-7) composites

3.6. Thermal and thermo-oxidative stability

The thermal and thermo-oxidative stability of pure NR, NR/lignin and NR/LPCs composites can be assessed, respectively, from the investigation of thermal and thermo-oxidative decomposition. Figure 12a shows the DTG curves of pure NR, NR/lignin and NR/LPCs composites in nitrogen. There is only one obvious thermal decomposition step of NR molecular chains, primarily initiated by thermal scissions of C–C chain bonds accompanying a transfer of hydrogen at the site of scission.

The thermo-oxidative decomposition is obviously different from the thermal decomposition as shown in Figure 12b, which are DTG curves of pure NR, NR/lignin and NR/LPCs composites in air, respectively. There are three peaks in the DTG curve of pure NR, in contrast to NR/lignin and NR/LPCs composites. The first large decomposition peak (358.8°C) is caused by the main oxidation of rubber. An addi-

tional two small peaks probably originate from degradation of compounding ingredient (440.4°C) and from the oxidation reaction of residual carbon. From the DTG curves of NR/lignin and NR/LPCs composites, it can be seen that there are no peaks at 440.4°C, probably because of the formation of lignin-sulfur intermediates originated during vulcanization of lignin-containing NR composites [22, 48]. Table 4 shows the thermal and thermo-oxidative degradation characteristics of pure NR, NR/lignin and NR/LPCs composites. For thermal decomposition, the 5, 50% weight loss and peak decomposition temperature (T_{max}) of NR/LPCs composites shift to higher values, compared with pure NR and NR/lignin composites. The enhanced thermal stability can be contributed to the nanoscale dispersion of LPCs in NR matrix, which results in the LPCs and NR molecular chains strongly interacted through various effects such as the branching effect, nucleation effect, size effect and surface effect [49]. However, the change of those characteristic temperatures in thermo-oxidative decomposition is more complicated. Except the T_{max} , other characteristic temperatures of NR/LPCs composites are inferior to that of NR/lignin composites. It is known that lignin’s hindered phenolic hydroxyls can act as a

Table 4. Characteristic temperatures of thermal and thermo-oxidative decomposition for pure NR, NR/lignin and NR/LPCs composites

Sample code	Thermal decomposition			Thermo-oxidative decomposition		
	$T_{5\%}$ [°C]	$T_{50\%}$ [°C]	T_{max} [°C]	$T_{5\%}$ [°C]	$T_{50\%}$ [°C]	T_{max} [°C]
L-0	283.5	375.1	370.0	289.2	372.8	358.8
L-3	310.7	385.4	381.0	294.3	379.6	368.6
LPCs-3	312.0	390.7	386.5	288.6	373.9	372.5

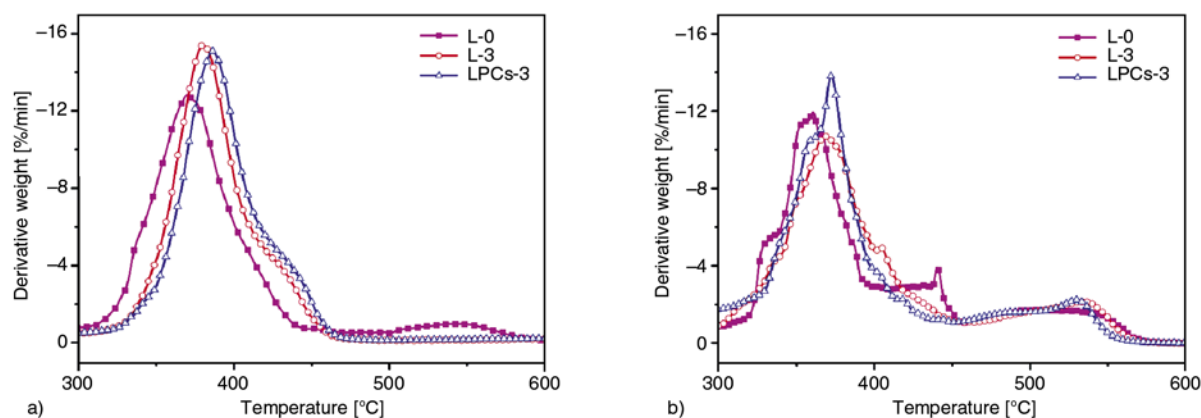


Figure 12. DTG curves of pure NR, NR/lignin (L-3) and NR/LPCs (LPCs-3) composites in nitrogen (a) and air (b)

stabilizer of reactions induced by oxygen and its radical species [5]. The complicated results in thermo-oxidative decomposition may be contributed that the interactions between the phenolic hydroxyls of lignin and PDADMAC, such as cation- π and π - π interactions, weaken the ability of scavenging free radicals of phenolic hydroxyls in lignin.

4. Conclusions

Natural rubber/lignin nanocomposites were successfully prepared via co-precipitation of colloidal lignin-cationic polyelectrolyte complexes and rubber latex. PDADMAC was adsorbed onto lignin particles through ion-ion interactions, cation- π and π - π interactions which were confirmed by UV-vis and FTIR. As employing proper amount of PDADMAC, nanoscale LPCs were formed, laying a foundation for fabrication NR/LPCs nanocomposites. LPCs accelerated the vulcanization of NR/LPCs nanocomposites. Furthermore, LPCs were homogeneously distributed in NR matrix, which resulted in improved mechanical properties, thermal and thermo-oxidative stability of NR/LPCs composites. In a word, this paper presents a promising strategy to utilize lignin for partial carbon black replacement.

Acknowledgements

The authors gratefully acknowledge National Natural Science Foundation of China (U1134005/L04) for financial supports.

References

- [1] Vainio U., Maximova N., Hortling B., Laine J., Stenius P., Simola L. K., Gravitis J., Serimaa R.: Morphology of dry lignins and size and shape of dissolved kraft lignin particles by X-ray scattering. *Langmuir*, **20**, 9736–9744 (2004).
DOI: [10.1021/la048407v](https://doi.org/10.1021/la048407v)
- [2] Gosselink R. J. A., Abächerli A., Semke H., Malherbe R., Käuper P., Nadif A., van Dam J. E. G.: Analytical protocols for characterisation of sulphur-free lignin. *Industrial Crops and Products*, **19**, 271–281 (2004).
DOI: [10.1016/j.indcrop.2003.10.008](https://doi.org/10.1016/j.indcrop.2003.10.008)
- [3] De Paoli M-A., Furlan L. T.: Sugar cane bagasse-lignin as photo-stabilizer for butadiene rubber. *Polymer Degradation and Stability*, **11**, 327–337 (1985).
DOI: [10.1016/0141-3910\(85\)90036-9](https://doi.org/10.1016/0141-3910(85)90036-9)
- [4] Boeriu C. G., Bravo D., Gosselink R. J. A., van Dam J. E. G.: Characterisation of structure-dependent functional properties of lignin with infrared spectroscopy. *Industrial Crops and Products*, **20**, 205–218 (2004).
DOI: [10.1016/j.indcrop.2004.04.022](https://doi.org/10.1016/j.indcrop.2004.04.022)
- [5] Pouteau C., Dole P., Cathala B., Averous L., Boquillon N.: Antioxidant properties of lignin in polypropylene. *Polymer Degradation and Stability*, **81**, 9–18 (2003).
DOI: [10.1016/S0141-3910\(03\)00057-0](https://doi.org/10.1016/S0141-3910(03)00057-0)
- [6] Barclay L. R. C., Xi F., Norris J. Q.: Antioxidant properties of phenolic lignin model compounds. *Journal of Wood Chemistry and Technology*, **17**, 73–90 (1997).
DOI: [10.1080/02773819708003119](https://doi.org/10.1080/02773819708003119)
- [7] Thielemans W., Wool R. P.: Lignin esters for use in unsaturated thermosets: Lignin modification and solubility modeling. *Biomacromolecules*, **6**, 1895–1905 (2005).
DOI: [10.1021/bm0500345](https://doi.org/10.1021/bm0500345)
- [8] Li Y., Sarkanen S.: Alkylated kraft lignin-based thermoplastic blends with aliphatic polyesters. *Macromolecules*, **35**, 9707–9715 (2002).
DOI: [10.1021/ma021124u](https://doi.org/10.1021/ma021124u)
- [9] Feldman D., Banu D., Campanelli J., Zhu H.: Blends of vinylic copolymer with plasticized lignin: Thermal and mechanical properties. *Journal of Applied Polymer Science*, **81**, 861–874 (2001).
DOI: [10.1002/app.1505](https://doi.org/10.1002/app.1505)
- [10] Hirose S., Kobashigawa K., Izuta Y., Hatakeyama H.: Thermal degradation of polyurethanes containing lignin studied by TG-FTIR. *Polymer International*, **47**, 247–256 (1998).
DOI: [10.1002/\(SICI\)1097-0126\(199811\)47:3<247::AID-PI966>3.0.CO;2-F](https://doi.org/10.1002/(SICI)1097-0126(199811)47:3<247::AID-PI966>3.0.CO;2-F)
- [11] Setua D. K., Shukla M. K., Nigam V., Singh H., Mathur G. N.: Lignin reinforced rubber composites. *Polymer Composites*, **21**, 988–995 (2000).
DOI: [10.1002/pc.10252](https://doi.org/10.1002/pc.10252)
- [12] Griffith T. R., MacGregor D. W.: Aids in vulcanization of lignin–natural rubber coprecipitates. *Industrial and Engineering Chemistry*, **45**, 380–386 (1953).
DOI: [10.1021/ie50518a039](https://doi.org/10.1021/ie50518a039)
- [13] Kumaran M. G., De S. K.: Utilization of lignins in rubber compounding. *Journal of Applied Polymer Science*, **22**, 1885–1893 (1978).
DOI: [10.1002/app.1978.070220711](https://doi.org/10.1002/app.1978.070220711)
- [14] Benko D. A., Hahn B. R., Cohen M. P., Dirk, S. M., Cicotte K. N.: Functionalized lignin, rubber containing functionalized lignin and products containing such rubber composition. U.S. Patent 2010/0204368 A1, USA (2010).
- [15] Boutsicaris S. P.: Lignin reinforced synthetic rubber. U.S. Patent 4477612, USA (1984).
- [16] Davidson M. J. G., Wunder R. H.: Latex coagulation process using lignin compound. U.S. Patent 4025711, USA (1977).
- [17] Doughty J. B.: Method of dry-milling carboxylic elastomers and alkali lignins. U.S. Patent 3325427, USA (1967).
- [18] Doughty J. B., Charlestion S. C.: Lignin reinforced rubber and method of preparation thereof. U.S. Patent 3247135, USA (1966).

- [19] Sirianni A. F.; Puddington I. E.: Reinforcing polymers with laundered amorphous lignin. U.S. Patent 3817974, USA (1976).
- [20] Keilen J. J., Pollak A.: Lignin for reinforcing rubber. *Industrial and Engineering Chemistry*, **39**, 480–483 (1947).
DOI: [10.1021/ie50448a013](https://doi.org/10.1021/ie50448a013)
- [21] Botros S. H., Eid M. A. M., Nageeb Z. A.: Thermal stability and dielectric relaxation of natural rubber/soda lignin and natural rubber/thiolignin composites. *Journal of Applied Polymer Science*, **99**, 2504–2511 (2006).
DOI: [10.1002/app.22865](https://doi.org/10.1002/app.22865)
- [22] Košíková B., Gregorová A.: Sulfur-free lignin as reinforcing component of styrene-butadiene rubber. *Journal of Applied Polymer Science*, **97**, 924–929 (2005).
DOI: [10.1002/app.21448](https://doi.org/10.1002/app.21448)
- [23] Maximova N.: Adsorption of lignin and lignin/cationic polymer complexes on cellulose fibres and their effect on sheet properties. PhD thesis, Helsinki University of Technology (2004).
- [24] Lappan R. E., Pelton R., McLennan I., Patry J., Hrymak A. N.: Kraft lignin-poly(DADMAC) precipitate formation. *Industrial and Engineering Chemistry Research*, **36**, 1171–1175 (1997).
DOI: [10.1021/ie960460u](https://doi.org/10.1021/ie960460u)
- [25] Li P., Pelton R.: Wood pulp washing 1. Complex formation between kraft lignin and cationic polymers. *Colloids and Surfaces*, **64**, 217–222 (1992).
DOI: [10.1016/0166-6622\(92\)80102-8](https://doi.org/10.1016/0166-6622(92)80102-8)
- [26] Vanerek A., van de Ven T. G. M.: Coacervate complex formation between cationic polyacrylamide and anionic sulfonated kraft lignin. *Colloids and Surfaces A: Physicochemical and Engineering Aspects*, **273**, 55–62 (2006).
DOI: [10.1016/j.colsurfa.2005.08.005](https://doi.org/10.1016/j.colsurfa.2005.08.005)
- [27] Gregorová A., Košíková B., Moravčík R.: Stabilization effect of lignin in natural rubber. *Polymer Degradation and Stability*, **91**, 229–233 (2006).
DOI: [10.1016/j.polymdegradstab.2005.05.009](https://doi.org/10.1016/j.polymdegradstab.2005.05.009)
- [28] Lindström T.: The colloidal behaviour of kraft lignin. *Colloid and Polymer Science*, **257**, 277–285 (1979).
DOI: [10.1007/BF01382370](https://doi.org/10.1007/BF01382370)
- [29] Norgren M., Edlund H., Wågberg L., Lindström B., Annergren G.: Aggregation of kraft lignin derivatives under conditions relevant to the process, Part I: Phase behaviour. *Colloids and Surfaces A: Physicochemical and Engineering Aspects*, **194**, 85–96 (2001).
DOI: [10.1016/S0927-7757\(01\)00753-1](https://doi.org/10.1016/S0927-7757(01)00753-1)
- [30] Lindström T., Westman L.: The colloidal behaviour of kraft lignin. *Colloid and Polymer Science*, **260**, 594–598 (1982).
DOI: [10.1007/BF01422591](https://doi.org/10.1007/BF01422591)
- [31] Dong D., Fricke A. L., Moudgil B. M., Johnson H.: Electrokinetic study of kraft lignin. *Tappi Journal*, **79**, 191–197 (1996).
- [32] Lindström T.: The colloidal behaviour of kraft lignin. *Colloid and Polymer Science*, **258**, 168–173 (1980).
DOI: [10.1007/BF01498276](https://doi.org/10.1007/BF01498276)
- [33] Chernoberezhskii Y. M., Atanesyan A. A., Dyagileva A. B., Lorentsson A. V., Leshchenko T. V.: Effect of the concentration of sulfate lignin on the aggregation stability of its aqueous dispersions. *Colloid Journal*, **64**, 637–639 (2002).
DOI: [10.1023/A:1020678430092](https://doi.org/10.1023/A:1020678430092)
- [34] Norgren M., Edlund H.: Stabilisation of kraft lignin solutions by surfactant additions. *Colloids and Surfaces A: Physicochemical and Engineering Aspects*, **194**, 239–248 (2001).
DOI: [10.1016/S0927-7757\(01\)00806-8](https://doi.org/10.1016/S0927-7757(01)00806-8)
- [35] Norgren M., Lindström B.: Dissociation of phenolic groups in kraft lignin at elevated temperatures. *Holzforchung*, **54**, 519–527 (2000).
DOI: [10.1515/HF.2000.088](https://doi.org/10.1515/HF.2000.088)
- [36] Micić M., Benítez I., Ruano M., Mavers M., Jeremić M., Radotić K., Moy V., Leblanc R. M.: Probing the lignin nanomechanical properties and lignin-lignin interactions using the atomic force microscopy. *Chemical Physics Letters*, **347**, 41–45 (2001).
DOI: [10.1016/S0009-2614\(01\)01022-3](https://doi.org/10.1016/S0009-2614(01)01022-3)
- [37] Mičić M., Jeremić M., Radotić K., Mavers M., Leblanc R. M.: Visualization of artificial lignin supramolecular structures. *Scanning*, **22**, 288–294 (2000).
DOI: [10.1002/sca.4950220503](https://doi.org/10.1002/sca.4950220503)
- [38] Sarkanen S., Teller D. C., Stevens C. R., McCarthy J. L.: Lignin. 20. Associative interactions between kraft lignin components. *Macromolecules*, **17**, 2588–2597 (1984).
DOI: [10.1021/ma00142a022](https://doi.org/10.1021/ma00142a022)
- [39] Sarkanen S., Teller D. C., Abramowski E., McCarthy J. L.: Lignin. 19. Kraft lignin component conformation and associated complex configuration in aqueous alkaline solution. *Macromolecules*, **15**, 1098–1104 (1982).
DOI: [10.1021/ma00232a027](https://doi.org/10.1021/ma00232a027)
- [40] Pogodina N. V., Tsvetkov N. V.: Structure and dynamics of the polyelectrolyte complex formation. *Macromolecules*, **30**, 4897–4904 (1997).
DOI: [10.1021/ma9617983](https://doi.org/10.1021/ma9617983)
- [41] Ouyang X., Deng Y., Qian Y., Zhang P., Qiu X.: Adsorption characteristics of lignosulfonates in salt-free and salt-added aqueous solutions. *Biomacromolecules*, **12**, 3313–3320 (2011).
DOI: [10.1021/bm200808p](https://doi.org/10.1021/bm200808p)
- [42] Deng Y., Zhang W., Wu Y., Yu H., Qiu X.: Effect of molecular weight on the adsorption characteristics of lignosulfonates. *The Journal of Physical Chemistry B*, **115**, 14866–14873 (2011).
DOI: [10.1021/jp208312a](https://doi.org/10.1021/jp208312a)
- [43] Pillai K. V., Rennecker S.: Cation- π interactions as a mechanism in technical lignin adsorption to cationic surfaces. *Biomacromolecules*, **10**, 798–804 (2009).
DOI: [10.1021/bm801284y](https://doi.org/10.1021/bm801284y)

- [44] Yang D-Q., Rochette J-F., Sacher E.: Spectroscopic evidence for π - π interaction between poly(diallyl dimethylammonium) chloride and multiwalled carbon nanotubes. *The Journal of Physical Chemistry B*, **109**, 4481–4484 (2005).
DOI: [10.1021/jp044511+](https://doi.org/10.1021/jp044511+)
- [45] Nando G. B., De S. K.: Effect of lignin on the network structure and properties of natural rubber mixes vulcanized by conventional, semiefficient and efficient vulcanization systems. *Journal of Applied Polymer Science*, **25**, 1249–1252 (1980).
DOI: [10.1002/app.1980.070250625](https://doi.org/10.1002/app.1980.070250625)
- [46] Verezhnikov V. N., Nikulin S. S., Poyarkova T. N., Misin V. M.: Separation of styrene-butadiene rubbers from latexes using dimethyldiallylammonium chloride-SO₂ copolymer. *Russian Journal of Applied Chemistry*, **74**, 1225–1229 (2001).
DOI: [10.1023/A:1013004025985](https://doi.org/10.1023/A:1013004025985)
- [47] Verezhnikov V. N., Nikulin S. S., Krutikov M. Y., Poyarkova T. N.: Kinetics of latex flocculation by cationic polyelectrolyte from data of nephelometry (in Russian). *Colloid Journal of the Russian Academy of Sciences*, **61**, 37–40 (1999).
- [48] Košíková B., Gregorová A., Osvald A., Krajčovičová J.: Role of lignin filler in stabilization of natural rubber-based composites. *Journal of Applied Polymer Science*, **103**, 1226–1231 (2007).
DOI: [10.1002/app.24530](https://doi.org/10.1002/app.24530)
- [49] Peng Z., Kong L. X., Li S-D., Chen Y., Huang M. F.: Self-assembled natural rubber/silica nanocomposites: Its preparation and characterization. *Composites Science and Technology*, **67**, 3130–3139 (2007).
DOI: [10.1016/j.compscitech.2007.04.016](https://doi.org/10.1016/j.compscitech.2007.04.016)